Washington University in St. Louis

Washington University Open Scholarship

All Theses and Dissertations (ETDs)

January 2009

Zeolites for Cleaner Processes: Alkylation of isobutane and n-butene

Subramanya Nayak
Washington University in St. Louis

Follow this and additional works at: https://openscholarship.wustl.edu/etd

WASHINGTON UNIVERSITY

Department of Energy, Environmental and Chemical Engineering

Dissertation Examination Committee:

Milorad Dudukovic, Chair

Palghat Ramachandran

John Gleaves

Bala Subramanaiam

Young-Shin Jun

Cynthia Lo

Renato Feres

Zeolites for Cleaner Processes: Alkylation of isobutane and n-butene

by

Subramanya Venkatesh Nayak

Acknowledgments

I would like to thank my advisor, Professor Milorad Dudukovic, for opening new world for me both geographically and scientifically, and enthusiastically and patiently encouraging me to grow both personally and professionally. Professor Dudukovic your insight and sharp criticism, which definitely added very much to my work is greatly appreciated.

I would like to thank my advisor, Professor Palghat Ramachandran, for discussions, his valuable calmness in hectic periods and for putting me up with milestones which certainly helped me finish my thesis.

I thank Professor John Gleaves who helped me with my experiments and for his cheerful attitude during the time of uncertainty. I thank Professor Bala Subramaniam for opening a wonderful center CEBC, where graduate student like me can learn and practice the science of green chemistry. I would like to thank my other committee members, Young-Shin Jun, Cynthia Lo and Renato Feres for agreeing to serve on my committee at such a short notice.

Dear colleagues, EECE staff and friends, I thank you very much for this unforgettable period. Especially, Achariya Suriyawong for making my stay in St. Louis delightful and adventurous, and Zeljko Kuzeljevic for all the fruitful discussions.

I would like to thank my family, Annu (Venkatesh Nayak), Mummy (Usha Nayak), Anna (Kiran Nayak), and Wheni (Vijetha Nayak) who supported me and gave me every opportunity to walk my own way. I deeply feel as I share my degree with them.

I also owe thanks to CEBC and CREL for financial support.

Dedicated to Anna

(Kiran Nayak)

Table of Contents

List of Table

List of Figures

ABSTRACT OF THE DISSERTATION

Zeolites for Cleaner Processes: Alkylation of isobutane and n-butene

by

Subramanya Nayak

Doctor of Philosophy in Energy, Environmental and Chemical Engineering

Washington University in St. Louis, 2009

Professor Milorad P. Dudukovic, Chairperson

Large pore beta zeolite with straight and zig-zag channels and USY zeolite with super cages have shown potential to replace toxic and hazardous mineral acids as catalysts in alkylation processes. However, due to rapid deactivation of these zeolites, their acceptance in industrial alkylation has been delayed. In this study we seek a deeper understanding of the kinetics, transport, and sorption of organic molecules used in alkylation processes in nano-porous zeolites. A six lump kinetic model that considers the key reactions for the zeolite catalyzed alkylation process is presented. The influence of different reactions and rate limiting steps on catalyst, and reactor performance is examined by coupling an appropriate reactor scale model, that accounts for different back-mixing on the reactor scale, with a zeolite particle model, which accounts for the diffusion inside the zeolite pores, the alkylation reactions, and zeolite deactivation. Single pulse TAP experiments are employed for obtaining estimates of intra-particle diffusion coefficients and better insight into adsorption-desorption dynamics and equilibria for species in beta and USY zeolite. This technique provides a unique way of directly

estimating transport and sorption processes at extremely low surface coverage, in the absence of an inert carrier stream, with no external mass transfer resistance, and with a negligible thermal effect.

The results of this study suggest that higher alkylate yield and longer zeolite activity are achieved by increasing the intrinsic hydride transfer rate and the ratio of isobutane to n-butene (P/ O) concentration in the vicinity of the catalyst. For a given P/O feed ratio, achieving close to plug flow for isobutane and high back-mixing for n-butene further enhances local P/O ratio and yield. Furthermore, optimal zeolite catalyst design should consider the egg shell type of Brønsted acid site distribution and a low silicon to alumina (Si/ Al) ratio. It is suggested that the ideal zeolite morphology should feature characteristics of both beta and USY zeolites. Specifically, it should have straight and zig-zag channels with an average pore diameter of 0.74 nm, for decreasing the deactivation rate. Further, to enhance the formation of 2,2,4-trimethylpentane it should have small cages in between these channels, with average pore diameter less than 1.2 nm but more than 0.74 nm.

CHAPTER 1

Zeolites for Cleaner Processes:

Alkylation of isobutane and n-butene

1.1 Introduction

Significant development of many technologies and their commercialization took place during World War II. One of these technologies was production of highest-quality gasoline (C_8 alkylates) by alkylation of isobutane with C3-C5 olefins for the warplanes of that time (airplanes during World War II were powered by reciprocating piston engines fuelled by high-octane gasoline rather than by jet engines fuelled by kerosene). The alkylation production first started in the late 1930s and early 1940s with collaborative efforts by several American companies. These high quality gasoline helped Allied planes to perform better than enemy planes and had significant impact on the outcome of the war.

After the war, the demand for C_8 alkylates as airplane fuel dropped but soon picked up as premium quality motor fuel. With todays environmental concerns, these clean burning C_8 alkylates are considered to be the gold standard for blending feed stocks in refineries. C_8 alkylates have a high research octane number (RON ~ 100) and motor octane number (MON ~ 98), virtually no olefins, sulfur, or aromatics, and have low Reid vapor pressure (RVP). Currently, 13 − 15 % of the refined gasoline pool is made up of these C_8 alkylates (Albright, 2003).

From World War II until today, homogeneous catalysts such as hydrofluoric acid (HF) (licensed by ConocoPhillips and UOP) and sulfuric acid (H_2SO_4) (licensed by DuPont/STRATCO and ExxonMobil) have been successfully used in alkylation. However, given the inherent toxicity and environmental hazards associated with these acid catalysts, these World War II processes should be replaced with greener processes. One promising alternative involves zeolites.

The synthesis of zeolites in the late 1960s and early 1970s rapidly found application in adsorption, catalysis and ion-exchange. Zeolites are made of aluminosilicates with the general formula $M_{2/n}O.Al_2O_3.ySiO_2$, where n is the valence of cation M, and y may vary from 2 to infinite. Structurally, zeolites are crystalline polymers in three-dimensional arrangement of TO_4 tetrahedra, where SiO_4 or AlO_4^- is connected via oxygen atoms to form subunits. These subunits are repeated to form large lattices. The remarkable ability of zeolites to behave as solid acid catalysts enables them to replace mineral acids (Corma and Martinez, 1993; Clark and Subramaniam, 1998; de Jong, et al., 1997; Feller and Lercher, 2004). Furthermore, owing to the molecular dimensions of their nano-pores, zeolites possess the peculiar property of molecular shape selectivity, which can increase C_8 alkylate yield and selectivity (Clark and Subramaniam, 1998). On the downside, zeolites deactivate with time on stream (TOS) and require periodic regeneration for continuous operation (Corma and Martinez, 1993; de Jong, 1997).

In this study, we demonstrate that *by understanding the fundamentals of catalysis, reaction engineering and material science we can develop hazard-free, waste-free, energy-efficient and economically feasible zeolite catalyzed processes for alkylation.*

In particular, we seek a deeper understanding of the kinetics, transport, and sorption of organic molecules used in alkylation processes in nano-porous zeolites, specifically beta and USY zeolites. We adopted a multi-scale research approach from molecular to reactor-scale schematized in Figure 1.1. At the reactor-scale, the combined effects of flow pattern configuration, reaction kinetics, concentration of acid sites and their distribution are theoretically investigated. At the molecular-scale, the importance of the zeolite pore morphology, shape, and internal pore structure is studied by a combination of experimental and theoretical methods.
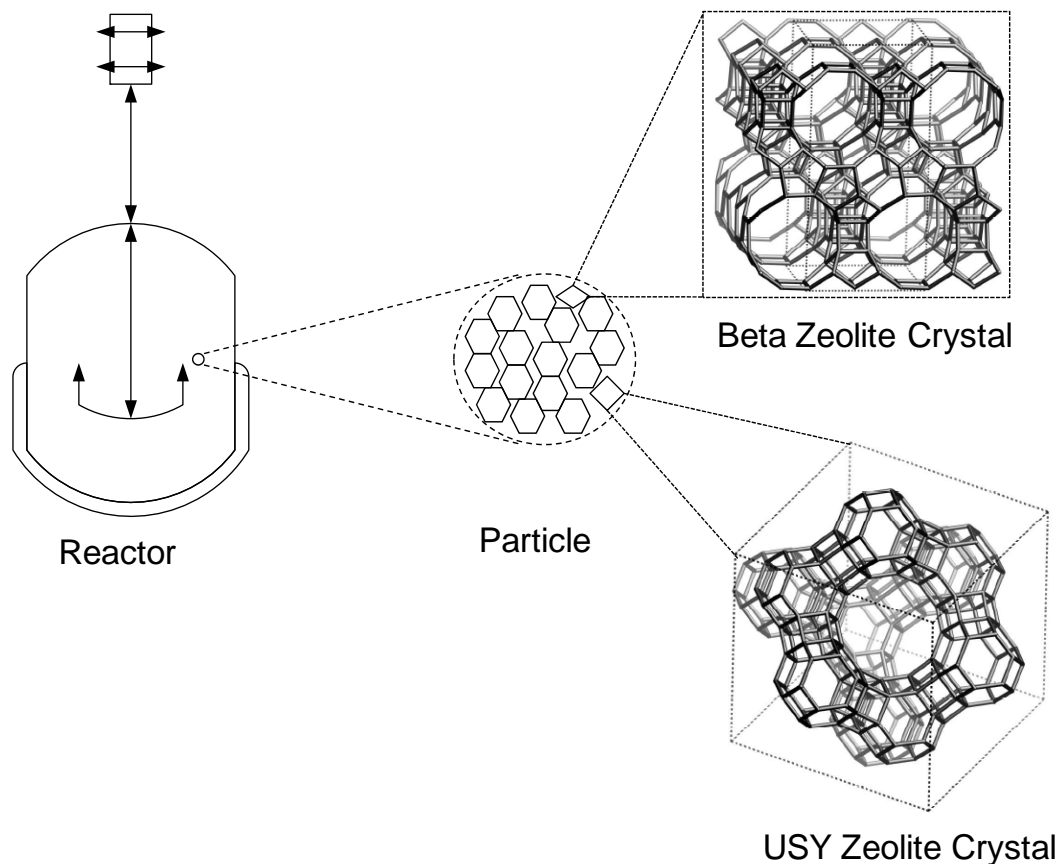
Figure 1.1: Multi-scale research approach adopted in this study.

This thesis is organized as follows:

Chapter 2 describes the key reaction steps that affect the C_8 alkylates yield and catalyst activity. The influence of different design and operating parameters on the performance of zeolite catalyzed alkylation processes is also studied.

Chapter 3 describes the experimental technique and methodology used to study transport and sorption in commercially available beta and USY zeolites.

Chapter 4 discusses the dimensionless equilibrium constant, apparent heats of adsorption, intra-particle diffusivities, and activation energies estimated at low surface coverage for the reactants, products, and byproducts of alkylation reactions in beta and USY zeolite. Chapter 5 presents the recommendation based on this study to improve and optimize the performance of zeolite catalyzed alkylation processes.

References

Albright, L. F. Alkylations Industrial. In Encyclopedia of Catalysis; Howath, I. T., Ed.; John Wiley and Sons: New York, 2003; Vol. 1, pp 226-281.

Corma, A., Martinez, A., (1993). Chemistry, catalysts and processes for isoparaffin alkylation: actual situation and future trends. Catal. Rev. Sci. Eng., 35, 483-570.

Clark M. and Subramaniam B., (1998). Extended Alkylate Production Activity during Fixed-Bed Supercritical 1-Butene /Isobutane Alkylation on Solid Acid Catalysts Using Carbon Dioxide as a Diluent. Ind. Eng. Chem. Res., 37, 1243.

de Jong, K.P., Mesters, C.M.A.M., Peferoen, D.G.R., van Brugge, P.T.M. and de Groote, C., (1996). Paraffin alkylation using zeolitie catalysts in a slurry reactor: Chemical engineering principles to extend catalyst lifetime. Chem. Eng. Sci. 51, 2053.

Feller A and J. A. Lercher, 2004, "Chemistry and technology of isobuatne/ alkene alkylation catalyzed by liquid and solid acids" Adv. Catal. 48 229-295.

CHAPTER 2

Modeling of Key Reaction Pathways: Zeolite Catalyzed

Alkylation Processes

Excerpts of this chapter have been submitted to Chemical Engineering Science

Abstract

A six lump kinetic model that considers the key reactions for the zeolite catalyzed alkylation process is presented. The influence of different reactions and rate limiting steps on reactor performance are examined by coupling an appropriate reactor model that accounts for different back-mixing on reactor scale, with a zeolite particle model which accounts for the diffusion inside the zeolite pore, the alkylation reaction, and zeolite deactivation. Model predictions are compared with experimental results and lead to conclusions that hydride transfer and oligomerization reactions are the key kinetic steps affecting the overall performance of zeolite catalyzed alkylation processes. It is suggested that higher alkylate yield and longer zeolite activity are achieved by increasing the intrinsic hydride transfer rate and the ratio of feed isobutane to n-butene (P/ O) concentration. For a given P/O feed ratio, achieving close to plug flow for isobutane and high back-mixing for n-butene further enhances local P/O ratio and yield. Furthermore, optimal zeolite catalyst design should consider the egg shell type of Brønsted acid sites distribution and lower silicon to alumina (Si/ Al) ratio.

2.1 Introduction

Alkylation of isobutane and n-butene to produce gasoline with high octane number and low Reid vapor pressure has been carried out since World War II. Homogeneous catalysts such as hydrofluoric acid (HF) and sulfuric acid (H_2SO_4) have been successfully used to catalyze these processes. These homogeneous catalyzed processes have matured over the years to give high product selectivity ($\sim 85 - 90$ %) at relatively safe operating conditions (Rao and Vatcha, 1996). Thus, these processes are licensed today everywhere in the world. However, due to the inherent toxicity and the environmental hazard associated with the employed mineral acid catalysts much research has been done over the years in searching for better more environmentally friendly alternatives (Feller and Lercher, 2004).

Different heterogeneous catalysts have been tried and tested, such as zeolites (Clark and Subramaniam 1998; de Jong et al., 1996; Feller and Lercher, 2004; Simpson et al., 1996), supported Nafion (Lyon et al., 2004), hetropoly acids (Sarsani et al., 2005) and ion exchange resins. Disadvantages associated with these catalysts are that the deactivation rate is high and/or product selectivity is too low, compared to the conventional processes. Zeolites in particular have been studied in great detail over the last three decades since they show high product selectivity ($\sim 85 - 95$ %), but also exhibit a rapid decrease in activity with time on stream (TOS) (de Jong et al., 1996; Martinis and Forment, 2006[a,b]; Simpson et al., 1996).

Irreversible adsorption of heavier hydrocarbons on active sites has been singled out as the major cause of zeolite's deactivation in alkylation reactions conducted in the vapor (Simpson et al., 1996) and in the liquid phase (de Jong et al., 1996; Martinis and Forment, 2006[a,b]). It has also been shown that, under liquid phase conditions, zeolite catalyzed alkylation reactions have an intra-particle diffusion limitation, which further enhances the deactivation rate (Sahebdelfar et al., 2002; Simpson et al., 1996).

The major constituents of the alkylate product stream are highly branched trimethylpentanes (TMP) that have high-octane blend values of approximately 100. Dimethylhexanes (DMH) have lower-octane blend values and are present in the alkylate stream at varying levels. Various factors, such as the olefin space velocity (OSV), the isobutane to n-butene (P/ O) feed ratio and the operating temperature, are believed to affect the catalyst life and the product patterns for zeolite catalyzed alkylation reactions (de Jong et al., 1997).

Ramaswamy et al. (2005), by relying on kinetic and deactivation schemes reported by de Jong et al. (1996), have shown that optimal reactor configuration and catalyst size and shape can significantly decrease the deactivation rate and increase the product yield. To simulate the system, Ramaswamy et al. (2005) used a four lump reaction kinetic model for alkylation of isobutane and n-butene, proposed by de Jong et al., (1996). However, this simplified kinetic model does not consider the key kinetic steps of hydride transfer between C_8 carbocations with isobutane to form C_8 alkylates. The hydride transfer

reaction is denoted as the main alkylation reaction in the recent literature (Martinis and Forment, 2006[a,b]), and as a result the effect of this reaction on the overall reactor performance needs further investigation.

An alkylation reaction catalyzed by zeolites consists of complex elementary reaction steps (Martinis and Forment, 2006[a,b]; Simpson et al., 1996). They include olefin-(de)protonation, oligomerization, hydride transfer, hydride shift and protonated cyclopropane (PCP) branching. Thousands of these elementary steps, governed by the rules of carbenium ion chemistry, account for the reaction network of the alkylation processes (Martens and Jacobs 1990; Gates et al. 1979). As a result, it is a difficult and time consuming task to develop a kinetic model and estimate all the rate parameters for such a complex system. While this level of science ultimately will be needed, at the moment our goal is to develop improved insight into this system by attempting to capture in a model the key pathways that affect alkylate yield and zeolite deactivation.

The objective of this study is to model the key reactions affecting the performance of zeolite catalyzed alkylation of isobutane and n-butene. A six lump kinetic model is proposed (Section 2.3). This kinetic model takes into account the key steps, such as hydride transfer and oligomerization, and is coupled with the zeolite particle transport model and reactor flow pattern model (Section 2.4). The results of the overall model are compared with the experimental data available in the literature to evaluate the suitability of the developed kinetic and reactor models (Section 2.6.2). Parametric studies are

performed with an emphasis on improving the understanding of and achieving better zeolite catalyst and reactor performance (Section 2.6.3).

2.2 Alkylation Mechanism

The widely accepted description of the governing chemistry for hydrocarbon transformations in solution is based on the carbenium ion mechanism (Boronat et al., 2002; Martinis and Forment[a,b], 2006). On the basis of 'ab initio' calculations (Boronat et al., 2002; Kazansky et al., 1996), supported by ample experimental evidence, it has been proposed that protonation of an olefin by zeolite Brønsted acid sites results in formation of stable covalent alkoxide intermediates. The transition states for these processes are similar in geometry and electronic structure to classical carbenium ions. As a result, it can be stated that the carbenium ion mechanism also governs the hydrocarbon transformation in zeolites.

To form the Brønsted acid sites in zeolites, silicon atoms in the framework are substituted by other cations, such as aluminum, sodium or potassium (Figure 2.1). Due to the different valency of these cations, charges are created in the framework, which have to be compensated for by the addition of protons. These proton acid (Brønsted) sites behave in the same way as the protons in an acidic solution. It is instructive to point out that only those with a tetrahedral alumina behaves as Brønsted sites (proton donors), due to strong interaction of oxygen atom with alumina over hydrogen. In contrast, acid sites with the

octahedral alumina behaves as Lewis sites (electron acceptors), due to weak interaction of oxygen atom with alumina.
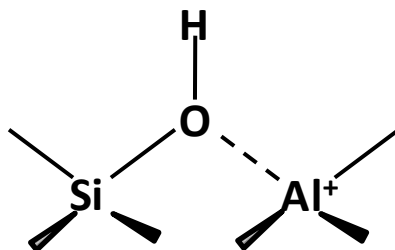
Figure 2.1: Brønsted acid sites in a zeolite particle

It has been shown (Martinis and Forment, 2006[a,b]; Roseler et al., 2004; Simpson et al., 1996; Sievers et al., 2008) that the alkylation reaction catalyzed by zeolite is initiated with protonation of n-butene on a Brønsted acid site to form C_4 carbocation. This is followed by addition of an olefin on the C_4 carbocation to form C_8 carbocation (Figure 2.2). When a hydrogen atom attached to a highly substituted carbon atom in an isobutane molecule is attacked by surface bonded C_8 carbocations, a hydride-ion transfer between them occurs, resulting in isooctanes and C_4 carbocation. Further C_8 carbocations can oligomerize with olefins to form heavier hydrocarbons.

$C_4H_8 + S \longrightarrow C_4H_8S \longleftarrow$ *Low* $\longleftarrow$ *Temperature* $\longrightarrow$ *High*

$+ C_4H_8$

High

$+ i\text{-}C_4H_{10}$

$C_8H_{16}S \longrightarrow C_8H_{18} \longrightarrow$ Isomerized C_8H_{18}

Isobutane/ Olefin Ratio

TMP   DMH
100 RON   Minor   60 RON

Minor

Minor
Cracked Products

$+ nC_4H_8$

$+ i\text{-}C_4H_{10}$

Low $C_{12}H_{24}S - C_{20}H_{40}S \longrightarrow C_{12}H_{26} - C_{20}H_{42} \longrightarrow C_5H_{12} - C_7H_{14}$

90 RON   60 − 93 RON

Low $\longleftarrow$ *Contact Time* $\longrightarrow$ *High*
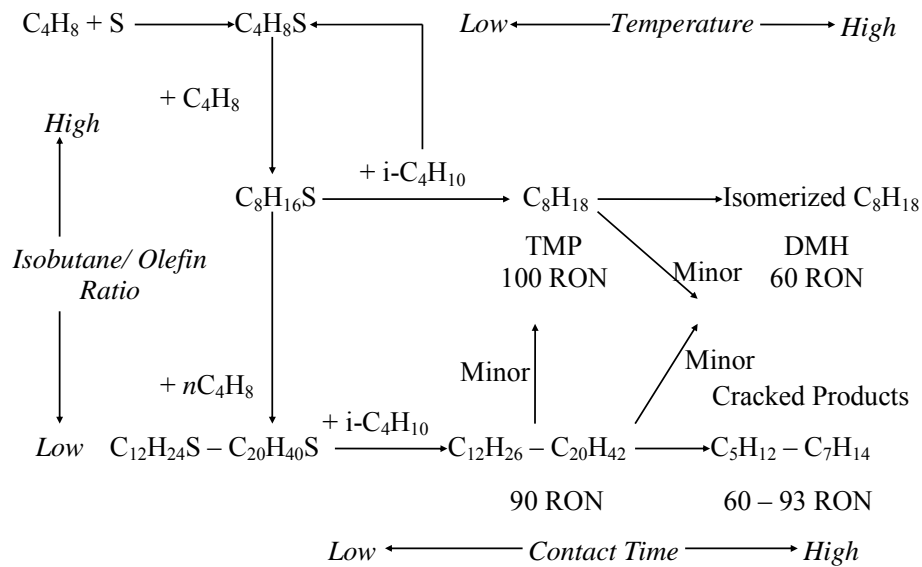
Figure 2.2: Simplified alkylation mechanism (Roeseler, 2004)

It may be argued that in alkylation reactions catalyzed by zeolites, the hydride transfer step controls the net hydrocarbon chain growth by promoting desorption of isooctanes from the active sites. The oligomerization step causes the formation of heavier hydrocarbons, which are irreversibly adsorbed on the active sites. As a result, the rate of hydride transfer and the rate of oligomerization affect not only the rate of desired product formation but also the overall rate of zeolite deactivation and product yield and selectivity.

2.3 Six Lump Kinetic Model

As already mentioned alkylation chemistry is highly complex (Corma and Martinez, 1993) which renders the development of a detailed kinetic model that could be used on

14

reactor scale very difficult. However, by considering the key kinetic steps, a simplified lumped kinetic model can be postulated (de Jong et al., 1996 and Simpson et al., 1996). Much can be learned regarding the goals for catalyst and reactor designs form such models.

If one assumes that the protonation and addition of lighter olefins on the zeolite Brønsted acid site (S) to form isooctenes can be treated as effectively the same reaction step with rate constant k_1, then this reaction can be represented by the following form:

$$C_4H_8 + C_4H_8 + S \xrightarrow{k_1} C_8H_{16} + S \ . \tag{R1}$$

Furthermore, the hydride transfers between different isomers of isooctenes and isobutane can be treated as effectively the same reaction step with rate constant k_2 and the direct alkylation between different lighter olefins and isobutane can likewise be treated as the same reaction step with rate constant k_3. Then the reactions for hydride transfer (see R2) and direct alkylation (see R3) steps can be reduced to the following form:

$$C_8H_{16} + C_4H_{10} + S \xrightarrow{k_2} C_8H_{18} + C_4H_8 + S \ , \tag{R2}$$

$$C_4H_{10} + C_4H_8 + S \xrightarrow{k_3} C_8H_{18} + S \ . \tag{R3}$$
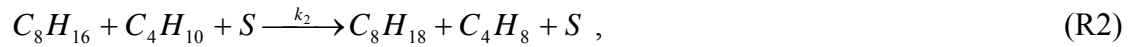
In this study, reactions R1 through R3 are considered to be the main reaction steps for forming alkylates in zeolite catalyzed alkylation of isobutane and n-butene. In this lumped kinetic model, C_5 to C_7 hydrocarbons formed by alkylation reactions are ignored for now. Further, alkylates formed via reactions R2 and R3 are considered to collectively

represent all the isomers of isooctanes. More detailed modeling can be done in the future based on actual elementary steps involved when these become better quantified.

The major limitation of the zeolite catalyzed alkylation reaction is rapid deactivation. Irreversible adsorption of heavier hydrocarbons on the Brønsted acid site has been deduced as the major cause of zeolite deactivation (Sievers et al., 2008). Improved understanding of the deactivation mechanism is needed to minimize the deactivation rate. Based on an understanding gained from the literature (de Jong et al., 1996; Ramaswamy et al., 2005; Simpson et al., 1996; Sievers et al., 2008), three routes for zeolite deactivation are considered in this work.

In the first scenario one considers different isomers of isooctenes oligomerizing with olefins to form heavier carbocations (Roeseler, 2004). It is reasonable to accept that the heavier carbocations formed on the Brønsted acid site are stable and have a high heat of desorption. The lumped deactivation mechanism for oligomerization reactions with rate constant k_4 is

$$C_8H_{16} + C_4H_8 + S \xrightarrow{\ k_4\ } C_{12}H_{24}S \ . \tag{R4}$$

In reaction R4, the formation of heavier hydrocarbons is truncated at C_{12} carbocation. It is assumed that once C_{12} carbocation is formed, the Brønsted acid site is irreversibly blocked, causing zeolite deactivation. Cracking of this heavier hydrocarbon is ignored as it is not prevalent under alkylation conditions (Simpson et al., 1996).

16

In the second scenario the formed isooctanes react with olefins on the Brønsted acid site to form highly branched paraffinic hydrocarbons. These bulky molecules may block the zeolite nano pores due to steric hindrance, hence decreasing the zeolite activity. The lumped deactivation reaction due to formation of paraffinic hydrocarbon with rate constant k_5 is

$$C_8H_{18} + C_4H_8 + S \xrightarrow{k_5} C_{12}H_{26}S \;. \tag{R5}$$

In the third scenario isooctenes isomerize on the Brønsted acid site to form complex olefinic dimers (de Jong et al., 1996). These dimers irreversibly adsorb to the Brønsted acid site to further decrease the zeolite activity. Reaction R6 shows the lumped deactivation due to formation of olefinic dimers with rate constant k_6:

$$C_8H_{16} + S \xrightarrow{k_6} C_8H_{16}S \tag{R6}$$

 Later, we will show that under the experimental conditions considered in an effort coordinated with this study (Sarsani, 2007) reaction R4 is more detrimental to catalyst activity than reactions R5 and R6. Nevertheless, here all reactions R1 through R6 are considered to develop a six lump kinetic model.

Assuming that the reactions R1 through R6 can be treated as elementary steps (de Jong et al., 1996), we can write the net rate of formation for isobutane, n-butene, isooctanes and isooctenes as follows:

$$R_{C_4H_{10}} = -\left(k_2[C_4H_{10}][C_8H_{16}] + k_3[C_4H_8][C_4H_{10}]\right)[S_0]\xi, \tag{2.1a}$$

$$R_{C_4H_8} = -\left(\begin{array}{c} k_1[C_4H_8]^2 + k_3[C_4H_8][C_4H_{10}] + k_4[C_4H_8][C_8H_{16}] \\ + k_5[C_4H_8][C_8H_{18}] - k_2[C_4H_{10}][C_8H_{16}] \end{array} \right)[S_0]\xi, \tag{2.1b}$$

$$R_{C_8H_{18}} = -\left(\begin{array}{c} k_5[C_4H_8][C_8H_{18}] - k_2[C_4H_{10}][C_8H_{16}] \\ - k_3[C_4H_8][C_4H_{10}] \end{array} \right)[S_0]\xi, \text{ and} \tag{2.1c}$$

$$R_{C_8H_{16}} = -\left(\begin{array}{c} k_2[C_4H_{10}][C_8H_{16}] + k_4[C_4H_8][C_8H_{16}] \\ + k_6[C_8H_{16}] - \dfrac{k_1[C_4H_8]^2}{2} \end{array} \right)[S_0]\xi. \tag{2.1d}$$

Here, $[S_0]$ is the initial concentration of the Brønsted acid sites in a zeolite particle which can be calculated from the ratio of silicon to alumina (Si/Al) present in the zeolite particle (equation 2.2) (de Jong et al., 1996). ξ is the zeolite particle activity and is a function of time and concentration (equation 2.3).

$$[S_0] = \frac{\rho_{cat}}{Mw_{cat}(1 + Si/Al)}, kmole/m_{cat}^3, \tag{2.2}$$

$$-\frac{\partial \xi}{\partial t} = \left(k_4[C_4H_8][C_8H_{16}] + k_5[C_4H_8][C_8H_{18}] + k_6[C_8H_{16}]\right)\xi. \tag{2.3}$$

These reaction rates should be combined with a description of diffusion and reaction inside the zeolite particle to obtain the effective rate of reactions. This effective rate of reactions should then be incorporated in the reactor models to get the overall performance of the zeolite catalyzed alkylation processes.

2.4 Transient Reactor and Zeolite Particle Models

In this work a transient CSTR (continuous flow stirred tank reactor) reactor model coupled with a transient zeolite particle model using film transport is developed for the previously described kinetic scheme. The reactor model takes into account the residence time distribution of the reactor bulk flow. The zeolite particle model accounts for diffusion inside the zeolite pore, the alkylation reaction and zeolite deactivation.

Dimensionless transient mass balance for the reactor model is

$$(1-\varepsilon_s)\tau_{res}\frac{dC_i^{e*}}{dt}=(C_i^{in*}-C_i^{e*})-\varepsilon_s\alpha_i(C_i^{e*}-C_i^{s*}).$$

(2.4)

Here, C_i^{e*} is dimensionless concentration of species i at the reactor exit, due to CSTR assumption. C_i^{in*} and C_i^{s*} are dimensionless concentrations of species i at the reactor inlet and at the zeolite particle surface, respectively. ε_s is the zeolite particle hold up and the notations τ_{res} and α_i are defined as

$$\tau_{res}=\frac{V_r}{Q}, \quad \alpha_i=\frac{V_r S_{cat} k_{sl}^i}{Q V_{cat}}.$$

As mentioned earlier, under liquid phase conditions, intra-particle diffusion limitations are observed (Ramaswamy et al., 2005; Sahebdelfar et al., 2002; Simpson et al., 1996). As a result, the mass balance for the zeolite particle should describe both intra-particle

diffusion and the net rate of formation for each species. Dimensionless transient reaction diffusion equations for isobutane, n-butene, isooctane and isooctenes are

$$
\tau_D^I \frac{\partial [C_4 H_{10}^*]}{\partial t} = \frac{1}{\eta^s} \frac{\partial}{\partial \eta} \left(\eta^s \frac{\partial [C_4 H_{10}^*]}{\partial \eta} \right)
$$
$$
- \left(\phi_2^2 [C_4 H_{10}^*][C_8 H_{16}^*] + \phi_3^2 [C_4 H_{10}^*][C_4 H_8^*] \right) \xi \frac{[S_0]\rho_{cat}}{C_{ref} \rho_{liq}} ,
$$

(2.5)

$$
\tau_D^O \frac{\partial [C_4 H_8^*]}{\partial t} = \frac{1}{\eta^s} \frac{\partial}{\partial \eta} \left(\eta^s \frac{\partial [C_4 H_8^*]}{\partial \eta} \right)
$$
$$
- \left(\begin{array}{c} \phi_1^2 [C_4 H_8^*]^2 + \dfrac{D_e^I}{D_e^O} \phi_3^2 [C_4 H_{10}^*][C_4 H_8^*] \\ + \phi_4^2 [C_4 H_8^*][C_8 H_{16}^*] + \phi_5^2 [C_4 H_8^*][C_4 H_{18}^*] \\ - \dfrac{D_e^I}{D_e^O} \phi_2^2 [C_4 H_{10}^*][C_8 H_{16}^*] \end{array} \right) \xi \frac{[S_0]\rho_{cat}}{C_{ref} \rho_{liq}} ,
$$

(2.6)

$$
\tau_D^A \frac{\partial [C_8 H_{18}^*]}{\partial t} = \frac{1}{\eta^s} \frac{\partial}{\partial \eta} \left(\eta^s \frac{\partial [C_8 H_{18}^*]}{\partial \eta} \right)
$$
$$
- \left(\begin{array}{c} \dfrac{D_e^O}{D_e^A} \phi_5^2 [C_4 H_8^*][C_4 H_{18}^*] - \dfrac{D_e^I}{D_e^A} \phi_2^2 [C_4 H_{10}^*][C_8 H_{16}^*] \\ - \dfrac{D_e^I}{D_e^A} \phi_3^2 [C_4 H_8^*][C_4 H_{10}^*] \end{array} \right) \xi \frac{[S_0]\rho_{cat}}{C_{ref} \rho_{liq}} ,
$$

(2.7)

$$
\tau_D^D \frac{\partial [C_8 H_{16}^*]}{\partial t} = \frac{1}{\eta^s} \frac{\partial}{\partial \eta} \left(\eta^s \frac{\partial [C_8 H_{16}^*]}{\partial \eta} \right)
$$
$$
- \left(\begin{array}{c} \dfrac{D_e^I}{D_e^D} \phi_2^2 [C_4 H_{10}^*][C_8 H_{16}^*] + \dfrac{D_e^O}{D_e^D} \phi_4^2 [C_4 H_8^*][C_8 H_{16}^*] \\ + \phi_6^2 [C_8 H_{16}^*] - \dfrac{D_e^O}{D_e^D} \dfrac{\phi_1^2 [C_4 H_8^*]^2}{2} \end{array} \right) \xi \frac{[S_0]\rho_{cat}}{C_{ref} \rho_{liq}} .
$$

(2.8)

20

Here, ϕ_1^2 through ϕ_6^2 are the ratios of the characteristic diffusion times to characteristic

reaction time (Thiele Moduli squared) for the reaction mechanisms R1 through R6 and

they are defined as:

$$\phi_1^2 = \frac{R_{cat}^2 k_1 C_{ref}^2}{D_e^O}, \quad \phi_2^2 = \frac{R_{cat}^2 k_2 C_{ref}^2}{D_e^I}, \quad \phi_3^2 = \frac{R_{cat}^2 k_3 C_{ref}^2}{D_e^I}, \quad \phi_4^2 = \frac{R_{cat}^2 k_4 C_{ref}^2}{D_e^O}, \quad \phi_5^2 = \frac{R_{cat}^2 k_5 C_{ref}^2}{D_e^O} \quad \text{and}$$

$$\phi_6^2 = \frac{R_{cat}^2 k_6 C_{ref}^2}{D_e^D}.$$

The other variables used in equation 2.5 through 2.8 are either defined earlier or in the

notation section.

Simulations have been performed assuming that at $t = 0$ the reactor is filled with pure

isobutane and the activity ξ is unity throughout the zeolite particle. The boundary

conditions for equations 2.5 through 2.8 are given as

$$\left. \frac{\partial C_i^*}{\partial \eta} \right|_{\eta=1_l} = B_i (C_i^{e*} - C_i^{s*}) \qquad , \tag{2.9}$$

$$\left. \frac{\partial C_i^*}{\partial \eta} \right|_{\eta=0} = 0 . \tag{2.10}$$

Boundary condition 2.9 couples the reactor model with zeolite particle model, and B_i is

defined as:

$$B_i = \frac{k_{sl}^i R_{cat}}{D_e^i}.$$

Thoenes and Kramer's (1958) correlation is used to predict the liquid-solid mass transfer coefficients ($k_{sl} \sim$ 3 x 10^{-5}, m/s). The effective pore diffusion coefficients are estimated from the following relation:

$$D_e^i = D_{liq}^i \frac{\varepsilon_{cat}}{\varsigma_{cat}} \,.$$

$$(2.11)$$

It is assumed that the effective pore diffusion coefficients do not vary with time and are not affected by zeolite particle deactivation. The diffusion coefficients D_{liq}^i are predicted from the correlations given by Wilke-Chang (Reid et al., 1977).

2.5 Solution Procedure

Initially the activity of the zeolite particle is set to unity. The governing equations (2.5 through 2.8) for the zeolite particle along with the boundary conditions (equations 2.9 and 2.10) are solved using the method of lines. The principle used in this method is the approximation of spatial derivatives which reduces the partial differential equations (PDEs) to sets of ordinary differential equations (ODEs). Orthogonal collocation with 10 collocation points is used to discretize the second order spatial derivatives. The resulting ODEs are solved using stiff ODE solvers from NETLIB libraries.

Once the concentration at the zeolite particle surface is obtained by numerically integrating equation 2.4, the concentration of each species in the reactor is calculated. The activity along the dimensionless spatial distance of the zeolite particle is then

updated using equation 2.3. With these updated values of zeolite particle activity, the concentrations of the species along the dimensionless spatial distance of the zeolite particle and in the reactor are calculated for the next time step. This procedure is repeated until the catalyst is completely deactivated.

2.6 Results and Discussions

In this section, the developed kinetic and reactor models are simulated for base case conditions to predict the performance of zeolite catalyzed alkylation processes in a single CSTR. Then, the developed models are validated by comparing model results with published experiments (Sarsani, 2007). Simulations are also carried out to understand the effects of key design and operating parameters on the performance of zeolite catalyzed alkylation processes.

2.6.1 Base Case

Figure 2.3 shows the predicted dimensionless concentrations at the CSTR exit of n-butene, isooctanes and isooctenes as a function of time on stream (TOS) for the operating conditions and the Thiele Moduli squared (ϕ_1^2 through ϕ_6^2) reported in Table 2.1. The rate constants assumed to calculate Thiele Moduli squared (ϕ_1^2 through ϕ_6^2) are of the same order of magnitude as reported in the literature (de Jong et al., 1996; Simpson et al., 1996). It is observed that ultimately complete n-butene breakthrough is reached with

23

TOS, due to complete deactivation of the zeolite catalyst. Initially the dimensionless concentration of isooctanes at the reactor exit increases with TOS. It reaches a maximum before decreasing due to a decrease in zeolite catalyst activity. A small concentration of isooctenes is also observed at the reactor exit and also exhibits a maximum with TOS.

Table 2.1: Input parameters for model simulations

OSV	1, kg/ kg$_{cat}$-hr
Feed P/ O ratio	5
Si/ Al ratio[a]	15
R_{cat}	3 x 10^{-4}, m
ρ_{cat}[a]	937, m^3/ kg$_{cat}$
ρ_{liq}[a]	450, m^3/ kg
ε_s[b]	1
ε_{cat}	0.48
ζ_{cat}	2
ϕ_1^2	900
ϕ_2^2	12
ϕ_3^2	1
ϕ_4^2	46
ϕ_5^2	2
ϕ_6^2	2

[a] de Jong et al. (1996); [b] Sarsani (2007)
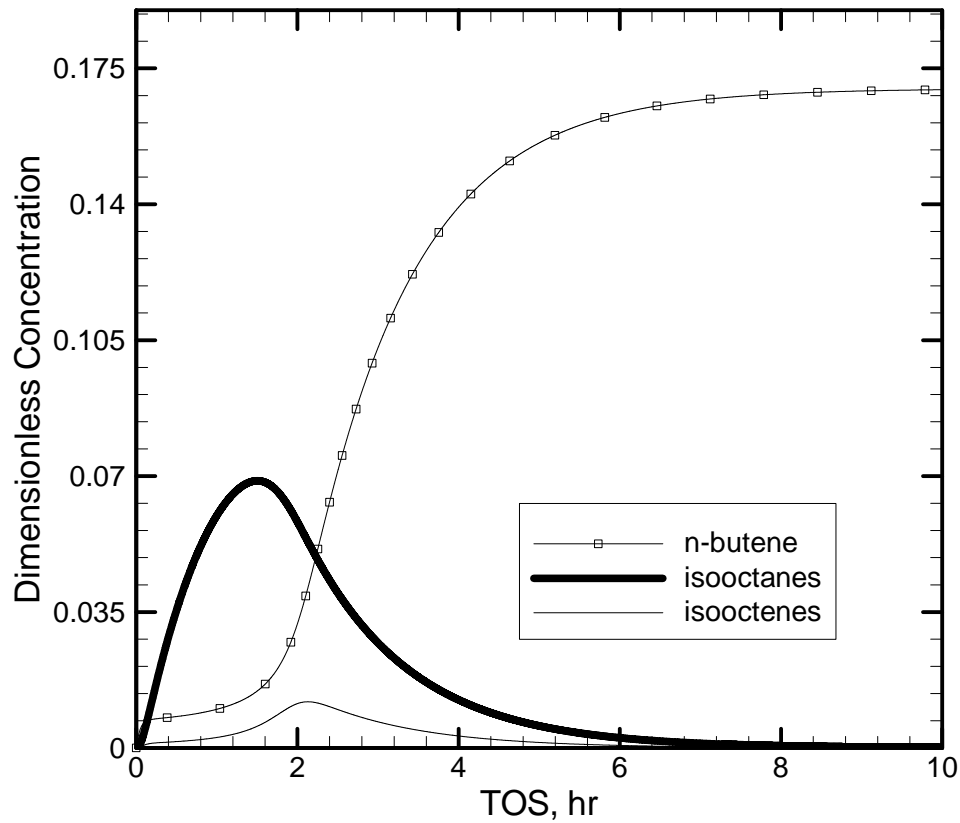
Figure 2.3: Predicted dimensionless concentration of n-butene, isooctane and isooctenes

as a function of TOS for the base case simulation for a single CSTR

(refer to Table 2.1 for input parameters).

2.6.2 Validation of kinetic and reactor models

The developed models are used to simulate the olefin conversion and alkylate yield reported by Sarsani, (2007). The scope of this study is not to carry out data regression to estimate kinetic constants for reactions R1 through R6, but to evaluate the predictive

25

abilities of the developed models. Sarsani (2007) performed alkylation of isobutane and n-butene on beta zeolite in a CSTR at 40 bar, temperature 75 ^{o}C and with OSV of 0.11 kg/ kg$_{cat}$-hr. In his work, a CSTR is initially filled with pure isobutane. At t = 0, a mixture of isobutane and n-butene with P/ O ratio of 5 is introduced into the reactor. The other operating parameters and Thiele Moduli squared used in his study are reported in Table 2.1.

The olefin conversion and alkylate yield are calculated as follows:

$$Olefin\,Conversion = \frac{[C_4H_8^*]^{in} - [C_4H_8^*]^e}{[C_4H_8^*]^{in}} \times 100\,,$$

$$Alkylate\,yield = \frac{[C_8H_{18}^*]^e - [C_8H_{18}^*]^{in}}{[C_4H_8^*]^{in}} \times 100\,.$$

Here, the olefin conversion is the ratio of moles of n-butene reacted to the moles of n-butene fed into the reactor system, and the alkylate yield is the ratio of moles of isooctanes produced to moles of n-butene fed to the reactor system.

The predicted olefin conversion and experimental data for the given time on stream (TOS) are shown in Figure 2.4. It is observed that initially the predicted conversion closely matches the experimental data. However, as the TOS increases, the model predicts a steep decrease in olefin conversion as compared to the experimental data. Similar behavior is also observed when the predicted olefin conversion is compared with experimental data for the USY zeolite catalyzed alkylation reaction. The steep decrease

in the predicted olefin conversion can be explained by understanding the deactivation mechanism proposed in this work.

From the values of the Thiele Moduli squared reported in Table 2.1, it is clear that reaction R4 is at least 20 times faster than reactions R5 and R6. As a result the oligomerization reaction between isooctenes and n-butene is more detrimental for catalyst deactivation. It is assumed that once C_{12} carbocation is formed the Brønsted acid site is irreversibly blocked, causing zeolite catalyst deactivation. However, under experimental conditions used it seems that the C_{12} carbocation further oligomerizes with n-butene (reaction R7), causing the slower decline of olefin conversion with TOS observed in the experimental data.

$$C_{12}H_{24}S + C_4H_8 \xrightarrow{k_7} C_{16}H_{34}S + C_4H_8 \xrightarrow{k_8} \ldots\ldots\ldots\ldots \tag{R7}$$
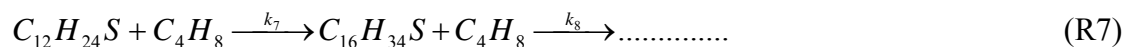
Furthermore, in the simulation, the initial concentration of the Brønsted acid sites is calculated based on the silicon to alumina ratio of beta zeolite (Si/Al = 13). However, the beta zeolite used in the experiment contains both Brønsted and Lewis acid sites (Sarsani, 2007). Lewis acid sites do not catalyze the alkylation reaction, but the presence of strong Lewis acid sites promotes the formation of unsaturated compounds by n-butene reactions (Diaz-Mendoza et al., 1998). This further explains the observed disparity between predicted olefin conversion and the experimental data. The model did not account for the additional reactions promoted by the catalyst that did not lead to the desired product as these reactions should be suppressed on the well designed catalyst.
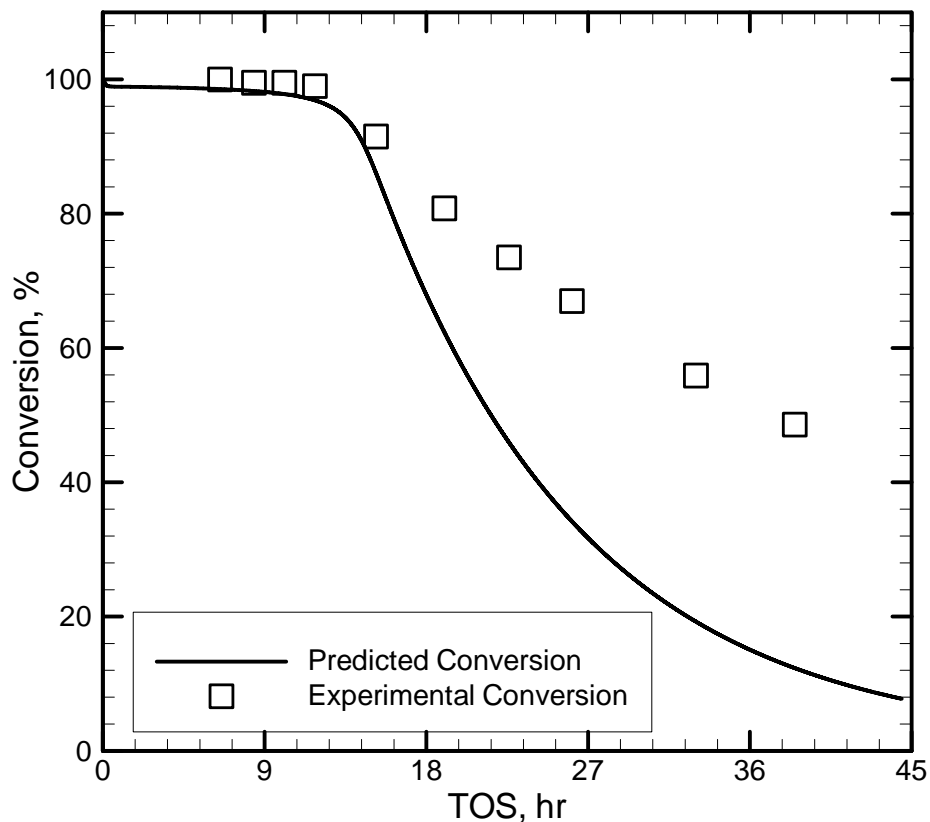
Figure 2.4: Comparison of TOS dependent olefin conversion predicted by the model and

that observed under experimental conditions (OSV = 0.11 kg/ kg$_{cat}$-hr, P/ O = 5; see

Table 2.1 for other input parameters).

The comparison between the predicted alkylate yield and experimental data for the given

time on stream (TOS) is shown in Figure 2.5. Good agreement of model predictions with

the experimental data is obtained, with less than 5 % absolute error between predicted

yield and experimental data. This can be taken as proof that the model indeed captured

the key reactions responsible for the production of alkylate and for the catalyst

deactivation. Initially the alkylate yield increases with TOS and reaches the maximum. With the subsequent drop in the olefin conversion the alkylate yield decreases. The slow drop in the alkylate yield is caused by intra-particle diffusion limitation in the zeolite pores. A similar trend for the alkylate yield was also observed by Feller et al., (2004) when they carried out alkylation of isobutane and n-butene on La-X zeolite.

The results obtained provide support to the notion that the reactions (R1 through R6) considered in this study are the key reaction steps affecting the performance of zeolite catalyzed alkylation processes. They also confirm that the alkylation reaction is catalyzed only by Brønsted acid sites and that alkylate yield rather than olefin conversion is the true measuring stick for the performance of any solid acid catalyzed alkylation process.

For predicting olefin conversion and alkylate yield, it is considered that the protonation and addition of lighter olefins on the zeolite Brønsted acid site (R1) is almost an order of magnitude faster than hydride transfer (R2) and direct alkylation (R3) (see Table 2.1). Furthermore, the reaction mechanism for hydride transfer (R2) is at least 12 times faster than reaction mechanism for direct alkylation (R3) (see Table 2.1). As a result, it can be concluded that the hydride transfer step between isooctenes and isobutane is more beneficial for producing isooctanes.

From the results shown in Figures 2.3 through 2.5, it is evident that the zeolite catalyst deactivates with TOS and that periodic regeneration is required to make zeolite catalyzed

alkylation processes feasible. In the succeeding sections, key design and operating parameters affecting the performance of zeolite catalyzed alkylation processes are discussed.
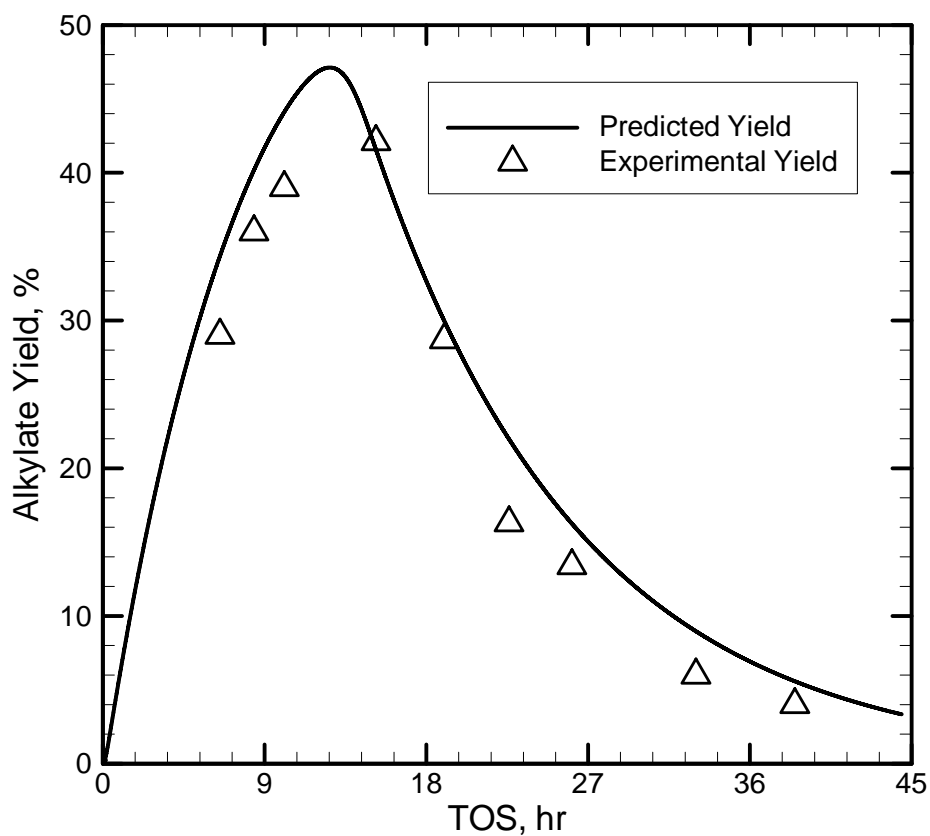
Figure 2.5: Comparison of TOS dependent alkylate yield predicted by the model and that observed under experimental conditions. (OSV = 0.11 kg/ kg$_{cat}$-hr, P/ O = 5; see Table 2.1 for other input parameters)

2.6.3 Influence of Design and Operating Parameters

2.6.3.1 Hydride Transfer and Oligomerization

As indicated earlier, the hydride transfer and oligomerization reaction are the key kinetic steps affecting the overall performance of zeolite catalyzed alkylation processes. It is desirable to have a high rate of hydride transfer, as it augments the production of alkylates and prolongs zeolite catalyst life by desorbing saturated hydrocarbon from the Brønsted acid sites (see R2). On the other hand, oligomerization reduces the production of alkylates and shortens zeolite catalyst life by producing unsaturated hydrocarbons which are irreversibly adsorbed on the Brønsted acid sites (see R4).

The rate of hydride transfer compared to rate of oligomerization can be increased by either increasing the kinetic constant of hydride transfer, hence decreasing the value of ϕ_4^2 / ϕ_2^2, or by increasing the P/O ratio; the latter is discussed in detail in a subsequent section. Here the effect of different values of ϕ_4^2 / ϕ_2^2 on the zeolite catalyst performance is studied. It is assumed that only the rate of hydride transfer between isooctenes and isobutane is changed. By doing so, for the fixed value of ϕ_4^2, simulations are done for various values of ϕ_2^2 (see Figure 2.6). Other parameters used in these simulations are reported in Table 2.1. It is observed that as the values of ϕ_4^2 / ϕ_2^2 decreases from 4 to 0.25, the alkylate yield and zeolite catalyst life are indeed considerably increased.

Figure 2.6: Simulated alkylate yield as a function of TOS for various values of ϕ_4^2 / ϕ_2^2

(refer to Table 2.1 for other input parameters).

Simpson et al., (1996) postulated that the hydride transfer step between isooctenes and isobutane is sterically more hindered than olefin oligomerization in the zeolite catalyzed alkylation process. They recommended that this steric effect can be mitigated to a certain extent by attaching the acid group to a tether and extending it away from the support surface. Furthermore, by adding an efficient hydride donor to the zeolite, the intrinsic rate of hydride transfer can be increased. This has been observed by Nivarthy and coworkers

(Nivarthy et al., 1998) when adamantane, an efficient hydride donor, was admixed to beta zeolite as catalyst.

2.6.3.2 Isobutane/ n-butene ratio (P/ O)

High isobutane concentration near the Brønsted acid site increases the production of alkylate yield by increasing the probability of hydride transfer between isooctenes and isobutane. In addition, the undesired oligomerization between isooctenes and olefins are suppressed, hence the zeolite catalyst life is longer. In a CSTR that we studied the feed P/ O ratio determines the isobutane concentration, which in turn determines the hydride transfer rate. Figure 2.7 shows the influence of feed P/ O ratio on the alkylate yield. The other parameters besides the P/O ratio used in these simulations are shown in Table 2.1. It is observed that with increased feed P/O ratio, higher alkylate yield is obtained, and the zeolite catalyst is active for a longer TOS.

A high feed P/ O ratio is beneficial for performance of zeolite catalyzed alkylation processes. However with an increase in P/ O ratio, the cost associated with separation and recycling the unreacted isobutane also increases, and this needs to be addressed separately. To maintain a high P/ O ratio in the reactor bulk, a back mixed reactor (slurry reactor) is more beneficial than a plug flow reactor (packed bed reactor). Ramaswamy et al. (2005) theoretically studied the role of reactant feeding pattern on the performance of zeolite catalyzed alkylation processes. They concluded that the CSTRs in series with

33

isobutane flowing in once-through mode while n-butene is distributed to each tank is the optimal configuration for obtaining a higher bulk P/ O ratio everywhere along the reactor, and hence, a higher alkylate yield with longer catalyst life. This feeding configuration is similar to Kellogg's cascade process for sulfuric acid alkylation (Albright, 1990).
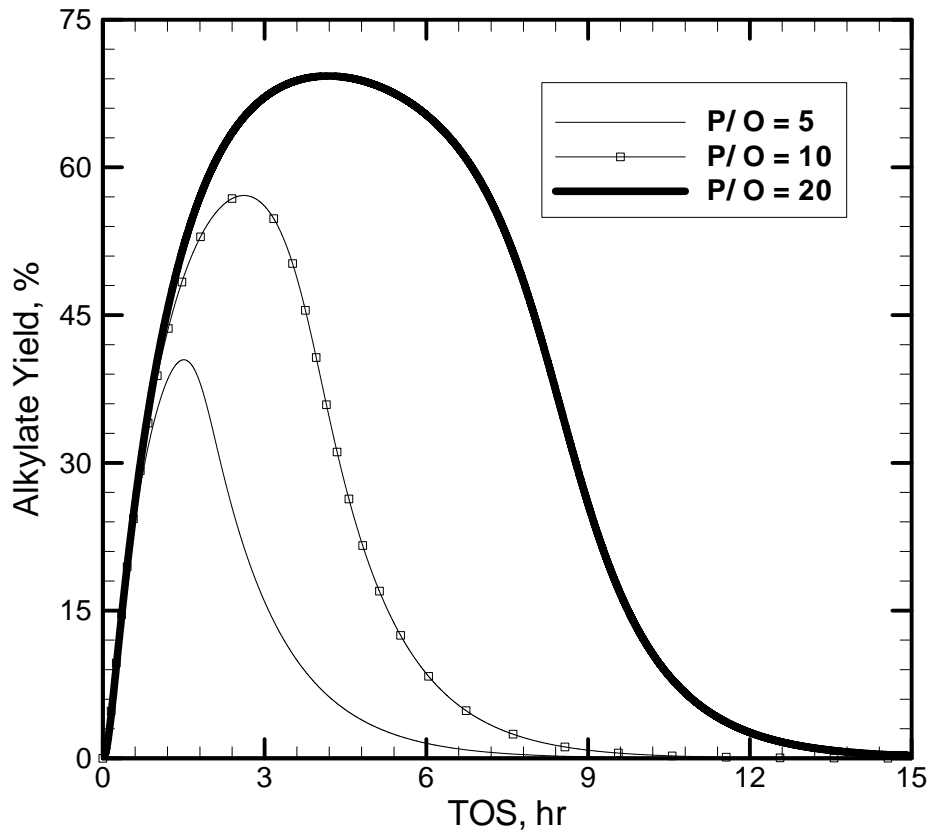
Figure 2.7: Simulated alkylate yield as a function of TOS for various P/ O ratios (refer to Table 2.1 for other input parameters).

2.6.3.3 Optimal Brønsted Acid Site Disrtibution

As mentioned, the zeolite catalyzed alkylation processs has an intra-particle diffusion limitation. This can be overcome by using a smaller zeolite particle (Ramaswamy et al., 2005). Futhermore, it would be more effective to locate the Brønsted acid site concentration near the external surface of the zeolite particle, rather than having a uniform distribution (Simpson et al., 1996). To find the optimal Brønsted acid site distribution, simulations were performed considering three different distributions shown in Figure 2.8. They are: egg shell (a thin shell of Brønsted acid sites placed near the external surface), egg white (Brønsted acid sites are uniformly distributed) and egg yolk (the Brønsted acid sites are placed in the particle core). Operating and design parameters considered in these simulations are the same as the ones reported in Table 2.1. Furthermore, the initial Brønsted acid site concentration is kept constant for all three types of distribution.

<div align="center">Egg Shell   Egg White   Egg Yolk</div>
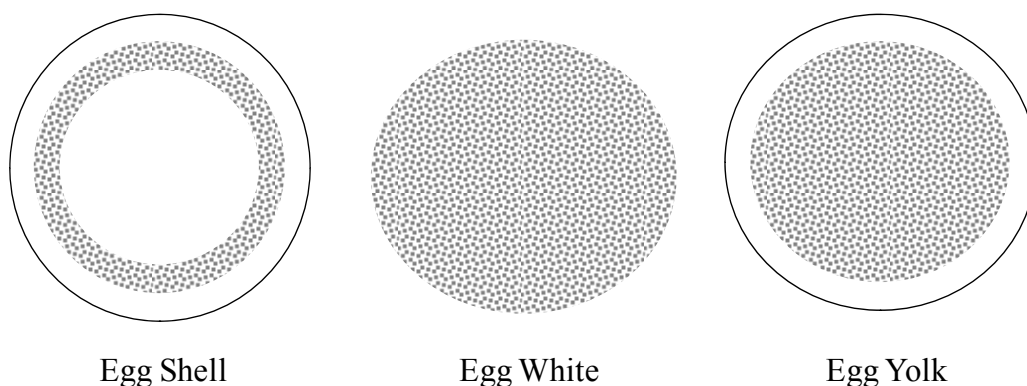
Figure 2.8: Different types of Brønsted acid site distributions simulated in this study.
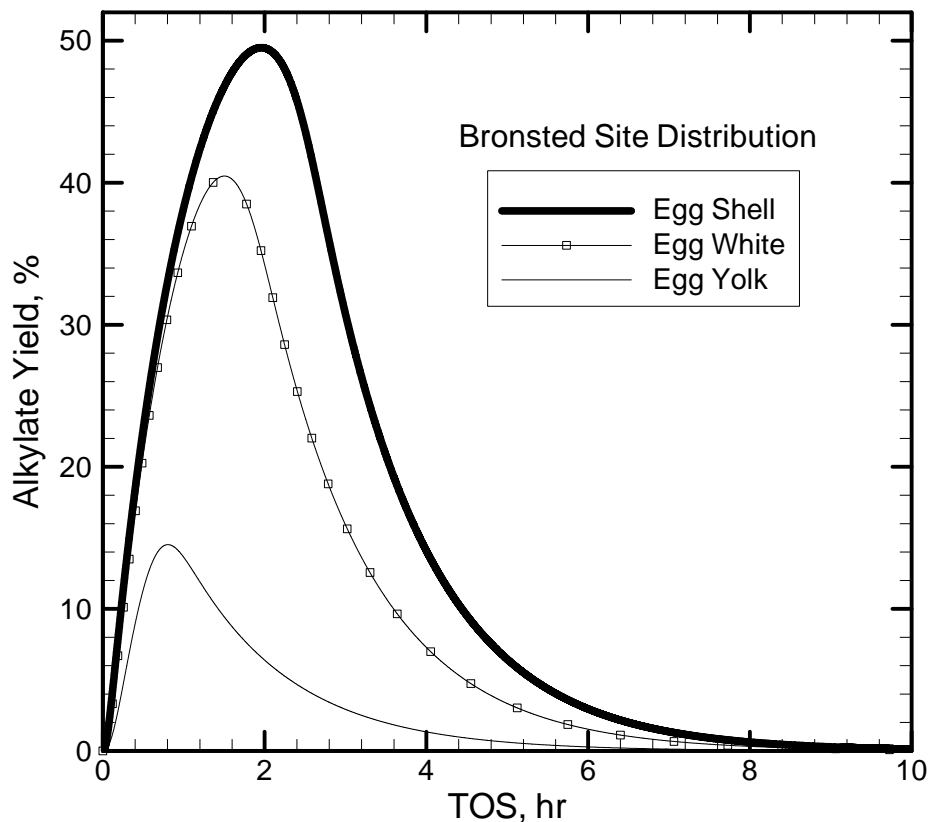
Figure 2.9: Simulated alkylate yield as a function of TOS for different types of Brønsted

acid site distributions (see Figure 2.8 for the types of Brønsted acid site distributions

considered and Table 2.1 for other input parameters).

The egg shell type of Brønsted acid site distribution performed much better than the egg

white and egg yolk distributions. In the egg shell type of distribution the thin shell of

Brønsted acid sites is placed just a small distance away from the external surface of the

zeolite. Thus, n-butene diffuses through a finite intra-particle space to reach the Brønsted

acid sites. As a result, the P/ O ratio in the intra-particle space is much higher than in the

bulk. Furthermore, alkylates formed in this thin shell can easily diffuse out to the bulk. The above stated phenomena cause an increase in the alkylate yield and longer zeolite catalyst life in the egg shell Brønsted acid site distribution (see Figure 2.9).

2.6.3.4 Silicon/ Aluminum Ratio

In a patent assigned to Mobil Oil (1998), the alkylation performance of beta zeolite with Si/ Al ratios of 7.3, 16.0 and 18.5 is compared. The only detail given in the patent is an increase in the TMP/ (C8-TMP) ratio with a decrease in the Si/ Al ratio. In this work the simulations are carried out with above stated Si/ Al ratios to study their effect on alkylate yield and zeolite catalyst activity. Aside from the Si/ Al ratio, all the other parameters used in these simulations are identical. In this study, the Si/ Al ratio affects the initial Brønsted acid site concentration as shown in equation 2.2.

The decrease in Si/ Al ratio increases the initial Brønsted acid site concentration. As a result, the alkylate yield and zeolite catalyst life increase with a decrease in the Si/ Al ratio, as shown in Figure 2.10. This result is qualitatively in agreement with the patent claims. Similar trend was also observed by de Jong et al. (1996), when they tested a series of Y zeolites with different Si/ Al ratios in a semi-batch reactor. The authors also tested a beta zeolite with a Si/ Al ratio of 15 that performed better than the Y zeolites. They postulated that beta zeolite with a lower Si/ Al ratio should lead to increased alkylate yield and longer catalyst life due to a higher Brønsted acid site concentration.
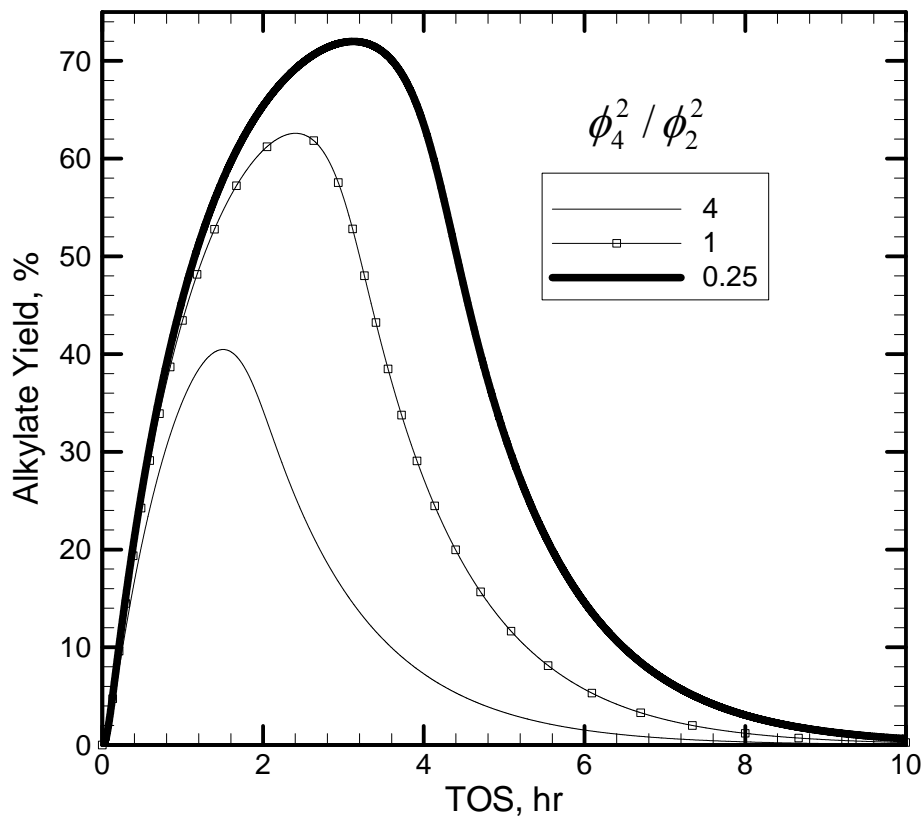
37
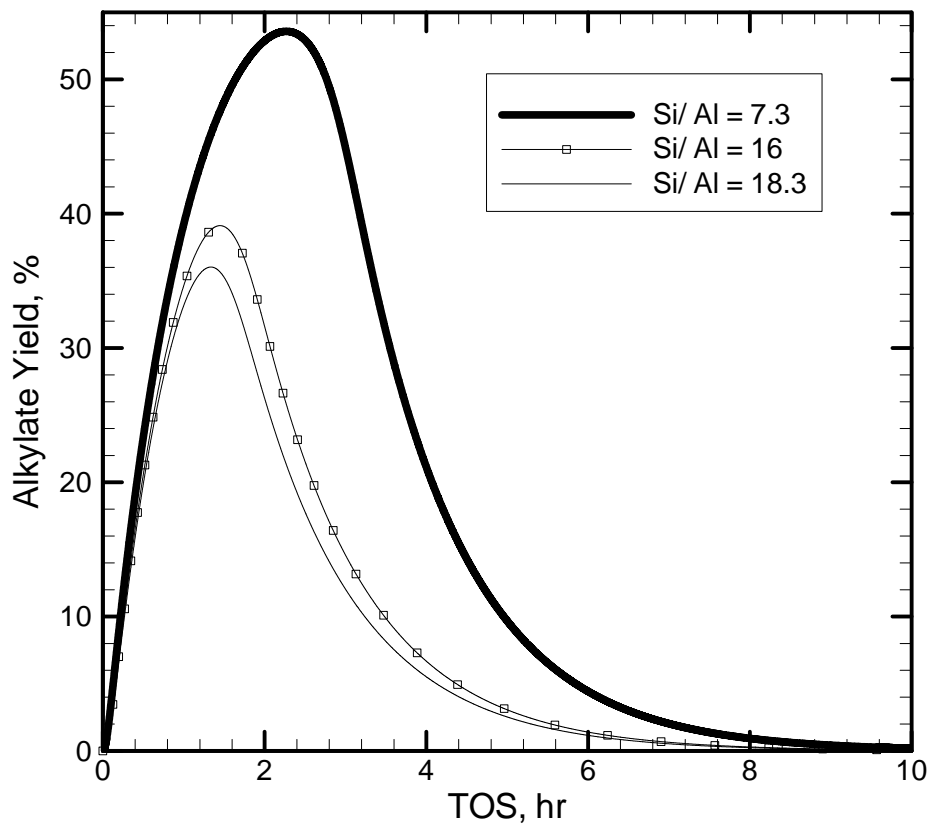
Figure 2.10: Simulated alkylate yield as a function of TOS for various Si/ Al ratios (refer

to Table 2.1 for other input parameters).

2.7 Summary

Hydride transfer between isooctenes and isobutane and oligomerization of isooctenes

with olefins are the key reactions affecting the overall performance of zeolite catalyzed

alkylation processes. A slow rate of hydride transfer compared to oligomerization is the

major cause of the low alkylates yield and shorter zeolite activity with time on stream (TOS).

A high value of kinetic constant for hydride transfer compared to oligomerization and a high P/ O ratio increases the rate of hydride transfer compared to oligomerization. The intrinsic rate of hydride transfer can be improved by adding efficient hydride donors to the zeolite catalyst. A flow pattern consisting of CSTRs in series with flow through of paraffin and with olefin distributed to each tank, is the most desirable reactor configuration for maintaining a high P/ O ratio everywhere in the system for a given feed P/O ratio.

A high local P/ O ratio can also be achieved by placing a thin shell of Brønsted acid sites a small distance away from the external surface of the zeolite particle. Such an egg shell Brønsted acid site distribution improves the performance of zeolite catalyst. The initial concentration of Brønsted acid sites can also be increased by having a low Si/ Al ratio in the zeolite particle.

Ultimately the zeolite catalyst deactivates with TOS, and periodic regeneration is required to make zeolite catalyzed alkylation processes feasible. Optimal catalyst and reactor design based on incresed scientific understanding will lead to yields that can be maintained on stream for suffcent time to justify commercialization of this

environmentally friendlier process compared to the current mineral acid catalyzed processes.

To further enhance the science of zeolite catalyzed alkylation processes, we need to examine the consequences of zeolite morphology on the diffusion and adsorption-desorption dynamics of the organic molecules. The understanding gained will help in better catalyst design, improved regeneration protocol and selection of optimal operating conditions. In the subsequent chapters the sorption and transport in commercially availbale beta and USY zeolites are studied and discussed.

Acknowledgement

Notations

B_i Biot number $= \dfrac{k_{sl}^i R_l}{D_e^i}$

CSTR Continuous Stirred Tank Reactor

C_i^* Dimensionless concentration of species i

C_{ref} Reference Concentration, kmole/ m^3

DMH   Dimethylhexane

D_e^i Effective Diffusivity of species i , m^2/ sec

D_{liq}^i Molecular Diffusivity of species i in liquid mixture, m^2/sec

k_j Rate Constant of reaction j, $m^6/kmole\text{-}sec$

k_{sl}^i Solid-liquid mass transfer coefficient, m/sec

Mw_{cat} Molecular weight of zeolite catalyst, $kmole/m^3$

OSV   Olefin space velocity, $kg/kg_{cat}\text{-}hr$

Q Volumetric flow rate, m^3/sec

RON   Research Octane Number

R_i Rate of formation of species i, $kmole/m^3\text{-}sec$

R_{cat} Zeolite particle radius, m

S_{cat} Surface area of zeolite particle, m^2

t Time, sec

TOS   Time on stream, hr

TMP   Trimethylpentane

V_{cat} Volume of zeolite particle, m^3

V_r Volume of reactor, m^3

Greek letters

ϕ_k^2 Thiele Modulus squared $= \dfrac{R_{cat}^2 k_j C_{ref}^2}{D_e^i}$

α_i $\dfrac{V_r S_{cat} k_{sl}^i}{Q V_{cat}}$

τ_{res} $\dfrac{V_r}{Q}$

τ_D^i $\dfrac{R_{cat}^2}{D_e^i}$

η Dimensionless spatial distance within the zeolite particle

ξ Zeolite catalyst activity

ε_s Solid holdup

ε_{cat} Zeolite particle porosity

ρ_{cat} Zeolite catalyst density, kg/ m^3

ρ_{liq} Liquid mixture density, kg/ m^3

ζ_{cat} Zeolite catalyst tortuosity

Subscripts/ Superscripts

i Index for species

j Index for reactions

k Index for Thiele Moduli squared

I Isobutane

O n-butene

A Isooctanes

D Isooctenes

cat Zeolite catalyst

liq Liquid mixture

in   Reactor inlet

e   Reactor exit

s   Zeolite external surface

References

Albright, L.F., (1990). Alkylation – 1: Alkylation will be key process in reformulated gasoline era. Oil and Gas Journal, 12, 79.

Agaskar, P. A. and Huang, T. J., Mobil Oil, (1998). U.S. Patent 5,824,835

Boronat M., Viruela P., Corma A., (2002). Ab initio and density-functional theory study of zeolite-catalyzed hydrocarbon reactions: hydrdide transfer, alkylation and disproportionate. Phys. Chem. Chem. Phys, 2, 3327

Corma, A., Martinez, A., (1993). Chemistry, catalysts and processes for isoparaffin alkylation: actual situation and future trends. Catal. Rev. Sci. Eng., 35, 483-570.

Clark M. and Subramaniam B., (1998). Extended Alkylate Production Activity during Fixed-Bed Supercritical 1-Butene /Isobutane Alkylation on Solid Acid Catalysts Using Carbon Dioxide as a Diluent. Ind. Eng. Chem. Res., 37, 1243.

de Jong, K.P., Mesters, C.M.A.M., Peferoen, D.G.R., van Brugge, P.T.M. and de Groote, C., (1996). Paraffin alkylation using zeolitie catalysts in a slurry reactor: Chemical engineering principles to extend catalyst lifetime. Chem. Eng. Sci. 51, 2053.

Diaz-Mendoza, F. A., Pernett-Bolano, L., and Cardona-Martinez, N., (1998). Thermochim.Acta 312, 47.

Feller A. and Lercher J. A., (2004). Chemistry and technology of isobuatne/ alkene alkylation catalyzed by liquid and solid acids. Adv. Catal. 48 229-295.

Feller A., Guzman A., Zuazo I., and Lercher J. A., (2004). On the mechanism of catalyzed isobutane/butene alkylation by zeolites. Journal of Catalysis 224, 80–93.

Gates, B. C.; Katzer, J. R.; Schuit, G. C., (1979). A. Chemistry of Catalytic Processes. McGraw-Hill: New York.

Kazansky, V. B.; Frash, M. V.; van Santen, R. A., (1996). Quantumchemical Study of the Isobutane Cracking on Zeolites. *Appl. Catal., A, 146*, 225.

Lyon C., Sarsani S., and Subramaniam B., (2004). 1-Butene + isobutane reaction on solid acid catalysts in dense CO_2 based reaction media: experiments and modeling. Ind. Eng. Chem. Res. Vol 43, 16, 4809-4814.

Martens, J. A.; Jacobs, P. A., (1990). Theoretical Aspects of Heterogeneous Catalysis; Moffat, J. B., Ed.; Van Nostrand Reinhold Catalysis Series; Van Nostrand Reinhold: New York.

Martinis J. M. and Forment G. F., (2006)[a]. Alkylation on Solid Acids. Part 1. Experimental Investigation of Catalyst Deactivation. Ind. Eng. Chem. Res 45, 940-953.

Martinis J. M. and Forment G. F., (2006)[b]. Alkylation on Solid Acids. Part 2. Single-Event Kinetic Modeling. Ind. Eng. Chem. Res 45, 954-967.

Nivarthy, G. S., Seshan, K., and Lercher, J. A., (1998)**.** The influence of acidity on zeolite H-BEA catalyzed isobutane/n-butene alkylation. *Microp. & Mesop. Mater.* **22**, 379

Rao P. and Vatcha S R., (1996). Solid acid alkylation process development is at crucial stage. Oil & Gas Journal, 9, 56-61.

Ramaswamy. R C, Ramachandran P.A., and Dudukovic M.P., (2005). Modeling of Solid Acid Catalyzed Alkylation Reactors. International Journal of Chemical Reactor Engineering, 3, A42.

Reid, C.R., Prausnitz, J.M. and Sherwood, T.K., (1997). The properties of gases and liquids. 3rd ed., McGraw-Hill, New York.

Roeseler, C., (2004). UOP Alkylene™ Process for motor fuel alkylation. 3rd ed., Handbook of Petroleum Refining Processes,

Sahebdelfar, S., Kazemeini, M., Khorasheh, F. and Badakhshan, A., (2002). Deactivation behavior of the catalyst in solid acid catalyzed alkylation: effect of pore mouth plugging. Chem. Eng. Sci., 57, 3611-3620.

Sarsani, V.S.R., Wang, Y., Subramaniam, B., (2005) "Toward Stable Solid Acid Catalysts for 1-Butene + Isobutane Alkylation: Investigations of Heteropolyacids in Dense CO2 Media." Ind. Eng. Chem. Res., 44:16 6491-6495.

Sarsani, V.S.R., (2007). Solid acid catalysis in liquid, gas-expanded liquid and near critical reaction media: Investigation of isobutane/ butene alkylation and aromatic acylation reactions. Ph D. Dissertation, University of Kansas.

Sievers C., Liebert J. S., Stratmann M. M., Olindo R., Lercher J. A., (2008). Comparison of zeolites LaX and LaY as catalysts for isobutane/2-butene alkylation. Applied Catalysis A: General, 336, 1-2,

Simpson M. F., Wei J., and Sundaresan S., (1996). Kinetic Analysis of Isobutane/Butene Alkylation over Ultrastable H-Y zeolite. Ind. Eng. Chem. Res. 35, 3861-3873.

Thoenes, D., Kramers, H., (1958). Mass transfer from spheres in various regular packing to a flowing fluid. Chem. Eng. Sci., 8, 271.

CHAPTER 3

Transport and Sorption Studies in Beta and USY Zeolites

via Temporal Analysis of Products (TAP)

Abstract

Single pulse TAP experiments are chosen for obtaining estimates of intra-particle diffusion coefficients and better insight into adsorption-desorption dynamics and equilibria for species in commercially available beta and USY zeolite. This technique provides a unique way of directly estimating transport and sorption processes at extremely low surface coverage $(\theta_i \rightarrow 0)$, in the absence of an inert carrier stream, with no external mass transfer resistance, and with a negligible thermal effect. The use of a thin zone TAP reactor configuration enables the use of small zeolite particles without causing high bed resistance. A theoretical model that considers transport and adsorption–desorption phenomena in the inter-particle and intra-particle space is developed and numerically solved. Numerical experiments demonstrate the ability of the model to represent the actual experimental response curves. It is shown that reliable values of intra-particle diffusivity and adsorption-desorption constants can be obtained from the TAP single pulse experiments when the three dimensionless constants of the model τ_{p_i} (the ratio of characteristic diffusion time in the micro-reactor to characteristic diffusion time in zeolite pore), K_{eq_i} (the ratio of characteristic desorption time to characteristic adsorption time), and $k_{d_i}^*$ (the ratio of characteristic diffusion time in the micro-reactor to characteristic desorption time) fall within a prescribed range.

3.1 Introduction

Large pore beta zeolite (de Jong et al., 1996; Sarsani 2007) and ultrastable Y zeolite (USY) (Simpson et al., 1996) (pore range from 0.56 to 0.72 nm) have exhibited high product selectivity and relatively long activity on stream for alkylation reactions. An improved understanding of the intra-particle (in the nano pores of zeolite particle) diffusion and adsorption-desorption of various species in these zeolites is required for further optimizing these catalysts, operating conditions, and regeneration protocols for alkylation processes. However, there are only a few studies in the literature on beta and USY zeolites that report these intra-particle properties for hydrocarbons of interest (Anderson et al., 1998; Denayer et al., 1998a; Denayer et al., 1998b; Mittelmeijer-Hazeleger et al., 2002; Lee et al., 2004; Bárcia et al., 2005; Schuurman et al., 2005; Bárcia et al., 2007; Wender et al., 2007; Gong, 2008; Lima et al., 2008; Truitt and White, 2009; Zhang et al., 2009). Commercially, these zeolites are available in the form of self aggregates with an average particle size of 5 μm and an average crystal size of 0.5 μm. These small particles make it difficult to obtain reliable estimates of the intra-particle diffusivity and adsorption-desorption constants by conventional tracer techniques (Karger and Ruthven, 1992).

Theoretical predictions of transport coefficients and adsorption isotherms in these zeolites, while significantly advanced in the last decade (Skoulidas and Sholl, 2003; Iyengar and Coppens, 2004; Plant et al., 2006) have not yet been able to yield results that

48

can be accepted without experimental confirmation. For that reason many different experimental techniques have been tested for determination of the above parameters but none have been universally adopted (Raghavan and Ruthven, 1983; Raghavan and Ruthven, 1985; Eic and Ruthven, 1988; Karge and Nießen, 1991; Karger and Ruthven, 1992; Hagelstein et al., 1994; Lee et al., 2004; Bárcia et al., 2005; Schuurman et al., 2005; Bárcia et al., 2007; Lima et al., 2008). These previously conducted studies can roughly be divided into: macroscopic and microscopic.

Most macroscopic experimental systems (Raghavan and Ruthven, 1983; Raghavan and Ruthven, 1985; Eic and Ruthven, 1988; Karger and Ruthven, 1992; Lee et al., 2004; Bárcia et al., 2005; Bárcia et al., 2007; Lima et al., 2008) introduce a concentration or partial pressure change of the probe molecules into a carrier stream continuously flowing over zeolites particles. The real time response of the probe molecules to such a perturbation is recorded at the exit. An appropriate theoretical model is used to represent the exit response and to estimate the desired parameters. Due to the presence of the carrier stream and external mass transfer resistance in most macroscopic experimental systems only a crude estimate of intra-particle diffusivity in small zeolite particles is possible (Karger and Ruthven, 1992; Lima et al., 2008). Moreover, the high concentration of probe molecules in these experiments can induce a thermal effect due to sorption. This effect is more pronounced in the case of small zeolite particles (Keipert and Baerns, 1998; Lima et al., 2008) further decreasing the reliability of the estimated intra-particle diffusivity and adsorption-desorption constants. In microscopic

49

experimental systems (Karge and Nießen, 1991; Hagelstein et al., 1994) the intra-particle diffusivity is directly calculated from the observed mean square displacement of the probe molecule. However, these techniques require the diffusing molecules to spend quite a long time in the intra-particle space, and do not have the resolution required for investigation of small zeolite particles.

The Temporal Analysis of Products (TAP) pulse response experiment is a fast and reproducible technique which in principle can be applied to study intra-particle diffusivity and adsorption/ desorption dynamics in zeolite particles (Keipert and Baerns, 1998; Nijhuis et al., 1999). In TAP pulse response experiments a small number of probe molecules are introduced as a pulse of very short duration into a micro-reactor maintained under high vacuum (10^{-8} torr). There is no continuous flow of a carrier stream, and under high vacuum conditions the external mass transfer resistance is absent. Furthermore, the low concentration of the probe molecules in the micro-reactor causes negligible thermal effects due to sorption, and the zeolite particles are easily maintained at isothermal conditions.

We used the single pulse TAP response experiment to estimate intra-particle diffusivity and adsorption-desorption constants in commercially available beta and USY zeolites. Single pulse TAP experiments are performed using n-butane, isobutane, 2,2,4-trimethylpentane, 2,5-dimethylhexane and argon as probe molecules (each 99.9 % purity). Argon, a noble gas, is inert on the surface of these zeolites and provides

information on transport in the inter- and intra-particle voids. TAP reactor models that account for the adsorption, desorption and intra-particle diffusion resistances offered by the zeolite particles are presented and solved numerically. Sensitivity analysis of model predictions is conducted to determine the range of conditions under which reliable estimate of the above mentioned parameters can be obtained.

The organization structure of this chapter is as follows: Section 3.2 describes the methodology and experimental procedure for the single pulse TAP response experiment. Section 3.3 explains the theory of the TAP experimental system and the model developed to represent the response curve. The numerical solution technique, of the developed models is briefly described in section 3.4. Section 3.5 shows the key results and provides pertinent discussion. The conclusions of this work are provided in section 3.6. The minimization procedure to estimate the model parameters and the values these parameters with their physical significance are discussed in the Chapter 4.

3.2 TAP Pulse Response Experiments

A TAP pulse response experiment is a special type of transient response experiment which was invented by Gleaves and Ebner in the 1980s (Gleaves et al., 1988). Figure 3.1 shows simplified schematic of TAP-2 reactor system. Figure 3.2 shows the photograph of the TAP reactor system used in this study. The experimental system for TAP consists of

an external high speed pulsing valve, and high vacuum chambers that house a packed-bed

micro-reactor, and a computer controlled quadruple mass spectrometer.
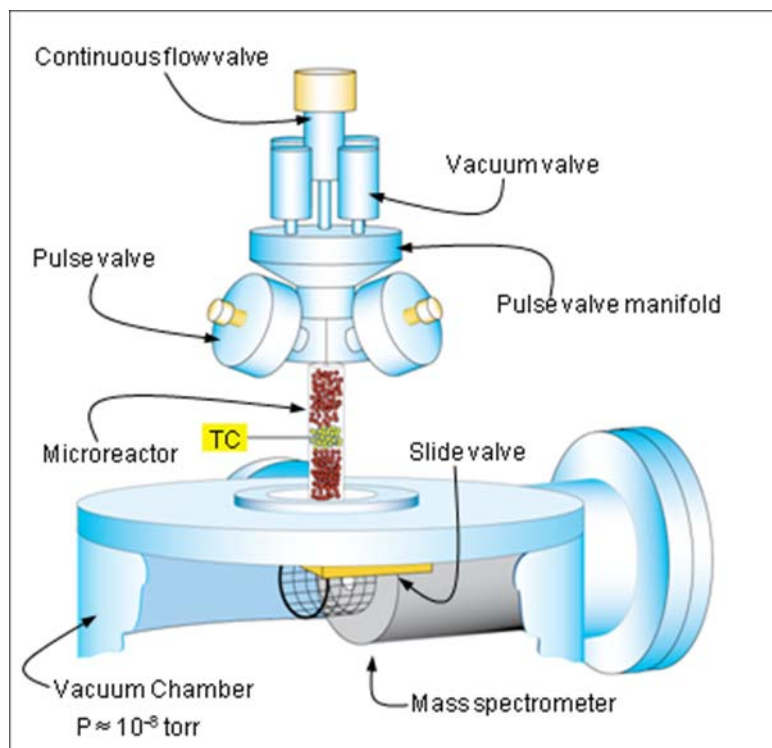
Figure 3.1: Simplified schematic of TAP-2 reactor system

(courtesy of Zheng et al., 2008)
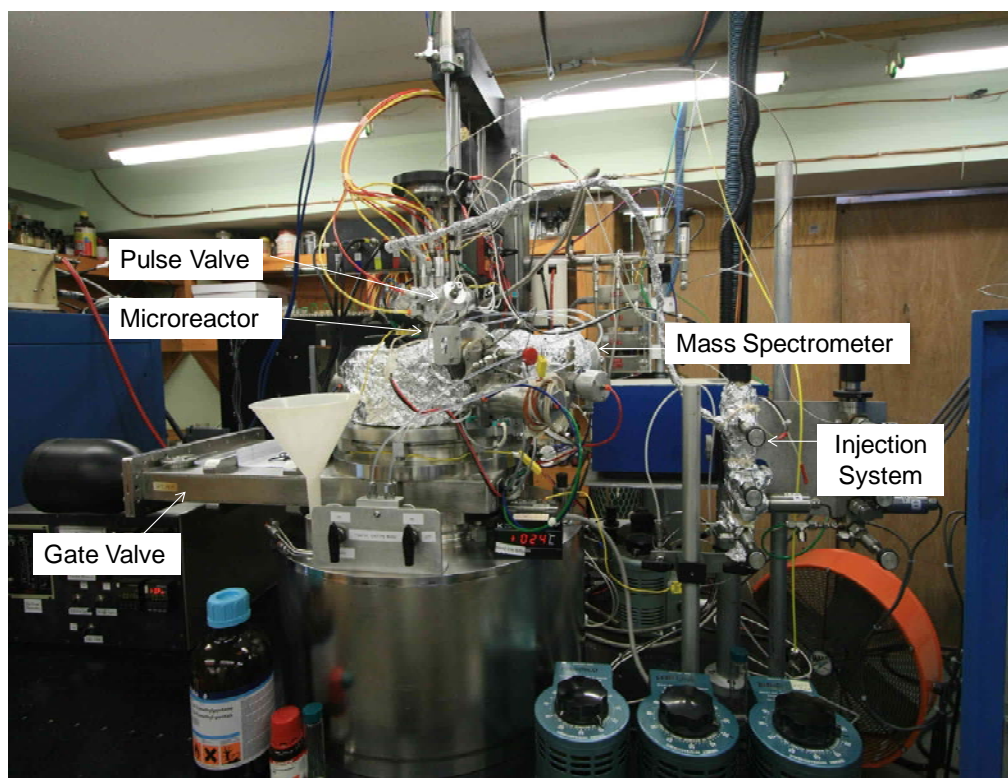
Figure 3.2: TAP reactor system

3.2.1 Single Pulse TAP Experiments

TAP experiments can be performed using single pulse or multi pulse experimental techniques. In this study the single pulse TAP experiments are performed. The underlying principle of single pulse TAP experiments is that the catalyst's state is insignificantly altered at the end of each pulse. In the single pulse mode of operation, a small number of probe molecules (10^{14} to 10^{18} molecules/ pulse) are pulsed for a short interval ($< 100\,\mu s$) at the entrance of the micro-reactor, and the probe molecules are evacuated at the other end (Figure 3.3). After exiting the micro-reactor, the probe molecules pass through the

detector of a mass spectrometer located at the exit. The mass spectrometer is set at the atomic mass unit of the desired probe species so that the real time intensity $\left(E_i(t)\right)$ is recorded. The response curve obtained from each pulse experiment contains the coded histories of different flow regimes and of the modes of interaction experienced by the probe molecules while travelling through the micro-reactor. Then the response curve is represented by appropriate theoretical models to extract quantitative information (Keipert and Baerns, 1998; Nijhuis et al., 1999).

3.2.2 Thin Zone Reactor Configuration

The micro-reactor can be packed in different configurations. The simplest configuration is a one zone TAP reactor, where a measured amount of zeolite particles is packed in the reactor. Two screens, one at each end of the zeolite bed, hold the zeolite particles in place. The use of small zeolite particles in the one zone TAP reactor configuration increases the bed resistance and causes the response curve to broaden, hence decreasing the signal to noise ratio (Delgado et al., 2004). To overcome these limitations, a thin zone reactor configuration (Shekhtman et al., 2003) is used. In the thin zone reactor configuration, a very small amount of zeolite particles is sandwiched between two inert zones containing larger non-porous quartz particles. This sandwich enables use of small zeolite particles without high bed resistance, and the thin zeolite zone is easily maintained at isothermal temperature. In this study, the zeolite particles (mass = 5 mg, diameter ~ $5\,\mu m$) are packed between two inert zones of nonporous quartz particles (mass = 800

mg, diameter $\sim 200\,\mu m$) in the micro-reactor of length $= 33 \times 10^{-03}$ m, and diameter $= 5 \times 10^{-03}$ m, as indicated in Figure 3.3. The resulting lengths in the reactor of inert zone I and inert zone II are 16.2×10^{-03} m each, and the length of the zeolite layer is 5.1×10^{-04} m.
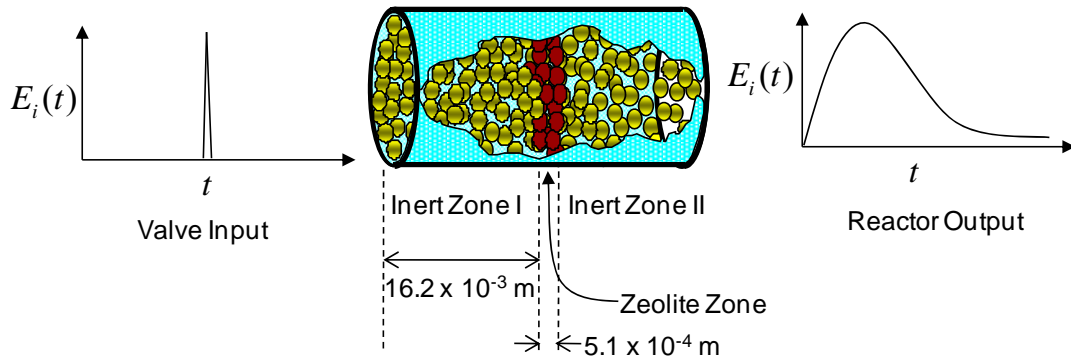
Figure 3.3: Pictorial representation of single pulse TAP response experiments. Thin zeolite zone is sandwiched between two inert zones of non-porous quartz particles.

3.2.3 Mathematical Treatment of TAP Experimental Data

As mentioned earlier, the molecule count $\left(E_i(t)\right)$ emerging from the exit of the micro-reactor is recorded in real time using a computer controlled quadruple mass spectrometer. To obtain quantitative information, the time dependent intensity $\left(E_i(t)\right)$ measured by the mass spectrometer is related to the molecular flow $\left(F_i(t)\right)$ at the exit of the micro-reactor.

In a single pulse TAP experiment, the intensity of an experimental response is proportional to the exit molecular flow, and the relationship is given by

$$F_i = a_i E_i(t).$$ (3.1)

Here, a_i is the absolute calibration factor for species i, $E_i(t)$ is the experimental response curve, and F_i is exit molecular flow (moles/sec) of species i. The dimensionless exit flow F_i^* is given as

$$F_i^* = \frac{F_i}{N_i} \frac{\varepsilon_b L^2}{D_{K_i}}.$$ (3.2)

Integrating equation 3.1 with respect to time, we get

$$\int_0^\infty F_i \, dt = a_i \int_0^\infty E_i \, dt,$$

or

$$a_i = \frac{\int_0^\infty F_i \, dt}{\int_0^\infty E_i \, dt}.$$ (3.3)

For a probe species involved in a reversible process (as in this study) or for a non-reacting probe species, the integration of the exit flow with respect to time yields the number of moles of probe species i injected in the system:

$$\int_0^\infty F_i \, dt = N_i.$$ (3.4)

So equation (3.3) can be rewritten as

$$a_i = \frac{N_i}{\int_0^\infty E_i \, dt}.$$ (3.5)

Thus, the time dependent intensity $\left(E_i(t)\right)$ measured by the mass spectrometer is related to molecular flow $\left(F_i(t)\right)$ at the exit of the micro-reactor as

$$F_i = \frac{N_i}{\int\limits_0^\infty E_i \, dt} E_i \,, \tag{3.6}$$

and the dimensionless exit flow F_i^* can be rewritten as

$$F_i^* = \frac{E_i}{\int\limits_0^\infty E_i \, dt} \frac{\varepsilon_b L^2}{D_{K_i}} \,. \tag{3.7}$$

3.3 Theory

From classical reaction engineering studies, we know that reliable estimations of intra-particle diffusivity and adsorption-desorption constants require well understood and quantifiable information about the other resistances experienced by probe molecules. In most macroscopic experimental systems, such as chromatography, zero length columns (ZLC), and tapered element oscillating micro-balances (TEOM) the pulse or step change of probe molecules is introduced into a continuous flowing carrier stream. Plug flow or an axial-dispersion model is used to describe the inter-particle flow pattern, and film theory is used to describe the external mass transfer resistance. However, the TAP system is different, since there is no continuous flow of carrier gas in the micro-reactor.

The flow of probe molecules in the evacuated micro-reactor is initiated by the pulse valve, and that flow lasts until all the molecules introduced in the pulse are evacuated from the reactor. Based on kinetic gas theory, at 10^{-8} torr and 373 K the mean free path lengths (λ) of argon, isobutane, n-butane, 2,2,4-trimethylpentane, and 2,5-dimethylhexane are 0.63 x 10^4 m, 0.26 x 10^4 m, 0.32 x 10^4 m, 0.20 x 10^4 m, and 0.21 x 10^4 m respectively. In comparison the mean size of passages between the particles packed $(\bar{r})$ in the micro-reactor is 1.33 x 10^{-4} m. calculated for a particle size of 2 x 10^{-4} m. This indicates that the frequency of collision between probe molecules and the particles packed in the micro-reactor is at least 8 orders of magnitude higher than the frequency of collision between two probe molecules. As a result, the Knudsen regime prevails in the micro-reactor as previously established (Gleaves et al., 1997). In the Knudsen regime the mean free path of a molecule is not limited by the nearby molecules but by the reactor size and size of passages between the packed particles. Knudsen diffusivity is given by (Gleaves et al., 1997)

$$D_K = \frac{2\varepsilon_b \bar{r}}{3\varsigma_p}\sqrt{\frac{8RT}{\pi Mw}}.$$
(3.8)

Here, $\bar{r}$ is the mean inter-particle distance or mean size of passages between the packed particles, which for spherical particles with mean particle radius R_p can be calculated as

$$\bar{r} = \frac{2\varepsilon_b}{3(1-\varepsilon_b)}R_p.$$
(3.9)

3.3.1 Inert Zone Model

The thin zone TAP reactor, shown in Figure 3.3 consists of three zones. The first and the last zones contain non-porous quartz, which is considered to be inert. Zeolite particles are placed between these two zones. In the Knudsen flow regime, the equation of continuity for inert probe molecules in the micro-reactor packed with inert particles is (Gleaves et al., 1997)

$$\varepsilon_b \frac{\partial C_i}{\partial t} = D_{K_i} \frac{\partial^2 C_i}{\partial z^2}.$$

(3.10)

Here, C_i is the bulk concentration of species i, D_{K_i} is the effective Knudsen diffusivity of species i, t is time, z is axial position in the micro-reactor ε_b is the bed porosity. The dimensionless bulk concentration defined as $c_i = \dfrac{C_i}{N_i / AL\varepsilon_b}$ is a pulse-normalized bulk concentration. The dimensionless micro-reactor position and dimensionless time are defined as $\xi = \dfrac{z}{L}$, and $\tau = \dfrac{D_{K_i} t}{\varepsilon_b L^2}$, respectively. In dimensionless form of equation (3.10) becomes:

$$\frac{\partial c_i}{\partial \tau} = \frac{\partial^2 c_i}{\partial \xi^2}.$$

(3.11)

The dimensionless initial condition for equation (3.11) is (Zou et al., 1993; Gleaves et al., 1997)

$$c_i(0, \xi) = 0.$$

(3.12a)

Further, the dimensionless inlet and outlet boundary conditions are (Zou et al., 1993; Gleaves et al., 1997)

$$\left.\frac{\partial c_i(\tau,\xi)}{\partial \xi}\right|_{\xi=0} = -\delta^*(\tau) \text{ and} \tag{3.12b}$$

$$c_i(\tau,1) = 0 . \tag{3.12c}$$

Here, $\delta^*(\tau)$ is the pulse-normalized Dirac delta function defined in the nomenclature. The flux at the inlet of the micro-reactor is non-zero (Dirac pulse) for a small time (< 100 μs pulse duration time) and zero otherwise This (equation 3.12b) represents the pulse injection which occurs between the opening and closing of the pulse valve (Zou et al., 1993). The boundary condition at the reactor outlet (equation 3.12c) reflects the fact that it is maintained under vacuum and that the concentration of probe molecules there is almost zero. In a three zone TAP system the continuity of concentration and flux at the boundaries between zones must be maintained. Additional description of the boundary conditions can be found elsewhere (Zou et al., 1993). Equations (3.11) and (3.12 a, b, c)) are used to represent the inert zones I and II.

3.3.2 Zeolite Zone Model

In the thin zeolite zone, besides inter-particle diffusion, one must account for additional phenomena taking place within the zeolite particles. These are adsorption-desorption of the probe molecules on the active sites on the zeolite surface and diffusion into the zeolite pores (Keipert and Baerns, 1998; Nijhuis et al., 1999). Because the TAP experiments are

60

carried out under high vacuum conditions the mass transfer in the meso- and macro-pores of the zeolite particles (pore diameter > 2 nm), i.e. in the inter-crystalline space, also obeys Knudsen law. However, the diffusional resistance offered by meso- and macro-pores is negligible, (pore diameter < 0.2 nm) compared to the diffusion resistance in the nano-pore space (pore diameter > 2 nm), since the mean pore radius is order of magnitude larger in the meso- and macro-pores than in the nano-pores. In addition, investigated in this study the combined meso- and macro-pore surface areas contribute only 10.5 % and 8.3 % to the total surface areas of beta and USY zeolites, respectively. The combined pore volumes of meso- and macro-pores contribute only 22.3 % and 19.6 % to the total pore volumes of beta and USY zeolite, respectively and contribute less than 0.5 % to the total inter-particle void volume. As a result any resistance (time constant) due to meso- or macro-pores cannot be dominant and clearly investigations under high vacuum conditions are well suited to address and attempt to quantify the resistances related to the small zeolite particles. The equation of continuity, given the low surface coverage in the inter-particle space of the thin zeolite zone, is

$$\varepsilon_b \frac{\partial C_i}{\partial t} = D_{K_i} \frac{\partial^2 C_i}{\partial z^2} - (1 - \varepsilon_b) q_{max} \left[k_{a_i} C_i - k_{d_i} \theta_i \right]_{r=R_p}. \tag{3.13}$$

Here θ_i is the dimensionless surface coverage defined as $\theta_i = \dfrac{q_i}{q_{max}}$. The second term on the right hand side of equation (3.13) represents the net flux of probe molecules into the zeolite particles, from the bulk gas phase to the surface of the zeolite particles, and is given as the net rate of adsorption on the outside zeolite surface.

To complete the model one must describe the behavior within the zeolite particles. At the zeolite surface it is assumed that the probe molecules first adsorb reversibly. Then the adsorbed molecule either diffuses inside the particle or it desorbs from the surface (see Figure 3.4).
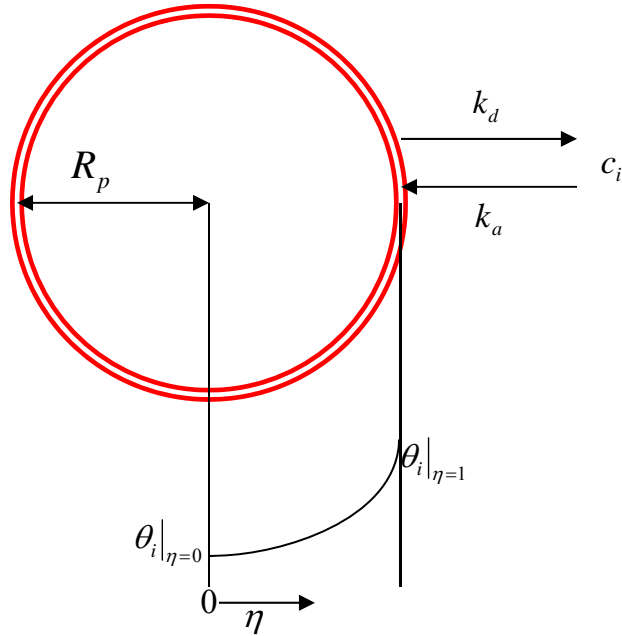
Figure 3.4: Pictorial representation of sorption processes on zeolite boundary and transport in zeolite's intra-particle space.

Within the pores the diffusing species in nano-porous zeolites never leave the force field of the pore walls (Van Den Broeke and Krishna, 1995). Hence, the molecules within the pores can be regarded as a single "adsorbed" phase (Ruthven and Karger, 1992). Thus, the true driving force for diffusion in intra-particle zeolite space is the gradient in the chemical potential, rather the gradient of concentration, as is assumed in Fick's

formulation. The one dimensional flux for a single component diffusing from the exterior surface to the center of a spherical zeolite particle with radius R_p, derived from the Maxwell-Stefan framework for non-ideal diffusion of binary liquids, is given as (Krishna et al., 2001)

$$J_i = -q_{max} D_{MS_i} \frac{\theta_i}{RT} \frac{d\mu_i}{dr}. \tag{3.14}$$

Here, J_i is the molar flux of species i, defined as moles of i transported per square meter per second, D_{MS_i} is the Maxwell-Stefan diffusivity, also referred to in the literature as the corrected diffusivity, and μ_i is the chemical potential of species i. The chemical potential gradient can be rewritten in terms of the gradient of the dimensionless surface coverage by assuming that the local adsorption equilibrium is attained on the zeolite wall, and by definition of chemical potential, $\mu_i = \mu_i^0 + RT \ln f_i$. Here, f_i is the fugacity of component i in the bulk phase.

In case of dilute gases, as under TAP experimental conditions, fugacity can be related to the bulk partial pressure or bulk molar concentration of species i. Thus, the chemical potential gradient is expressed as

$$\frac{\theta_i}{RT} \frac{d\mu_i}{dr} = \Gamma \frac{d\theta_i}{dr}, \tag{3.15}$$

and the one–dimensional flux along the spherical zeolite particle is given as

$$J_i = -q_{max} D_{MS_i} \Gamma \frac{d\theta_i}{dr}. \tag{3.16}$$

63

Here, Γ is the thermodynamic correction factor, defined as $\Gamma = \theta_i \dfrac{\partial \ln f_i}{\partial \theta_i} = \dfrac{\partial \ln f_i}{\partial \ln \theta_i}$.

Similarly the Fickian diffusivity or transport diffusivity (D_{T_i}) is related to the Maxwell-Stefan diffusivity (D_{MS_i}) by $\dfrac{D_{T_i}}{D_{MS_i}} = \Gamma$ (Krishna et al., 2001 and Paschek et al., 2003).

Under the limit of zero surface coverage $(\theta_i \to 0)$, the Fickian and Maxwell-Stefan diffusivities are identical $(D_{T_i} = D_{MS_i})$ and the thermodynamic correction factor is unity $(\Gamma = 1)$ (Paschek et al., 2003). This is normally the case under TAP experimental conditions, as the number of molecules in a single pulse is typically much smaller (1,000 – 1,000,000 times) than the number of active sites in the zeolite particles. Thus, the one-dimensional flux under the limit of zero surface coverage is given as

$$J_i = -q_{max} D_{T_i} \frac{d\theta_i}{dr}, \qquad \theta_i \to 0 . \tag{3.17}$$

For a spherical geometry, the mass balance in the intra-particle space is

$$\frac{\partial \theta_i}{\partial t} = D_{e_i} \left[\frac{\partial^2 \theta_i}{\partial r^2} + \frac{2}{r} \frac{\partial \theta_i}{\partial r} \right]. \tag{3.18}$$

Equations (3.13) and (3.18) can be transformed in dimensionless form as

$$\frac{\partial c_i}{\partial \tau} = \frac{\partial^2 c_i}{\partial \xi^2} - (1 - \varepsilon_b) k_{d_i}^* \left[K_{eq_i} c_i - \overline{\theta_i} \right]_{\eta=1} \tag{3.19}$$

and

$$\frac{\partial \overline{\theta}_i}{\partial \tau} = \tau_{p_i} \left[\frac{\partial^2 \overline{\theta}_i}{\partial \eta^2} + \frac{2}{\eta} \frac{\partial \overline{\theta}_i}{\partial \eta} \right]. \tag{3.20}$$

The dimensionless boundary conditions for equation (3.20) at the zeolite particle exterior surface and center are given as

$$\left. \frac{\partial \overline{\theta}_i}{\partial \eta} \right|_{\eta=1} = \frac{k_{d_i}^*}{3\tau_{p_i}} \left[K_{eq_i} c_i - \overline{\theta}_i \right]_{\eta=1} \tag{3.21 a}$$

and

$$\lim(\eta \frac{\partial \overline{\theta}_i}{\partial \eta}) \Big|_{\eta=0} = 0. \tag{3.21 b}$$

Here, $\overline{\theta}_i$ is the pulse-normalized dimensionless surface coverage, analogous to the pulse-normalized dimensionless bulk concentration (c_i). It is the ratio of the concentration of sites occupied by the adsorbing species (q_i), and the bulk concentration in the micro-reactor that would result if all the molecules introduced by the pulse valve were distributed instantaneously throughout the inter-particle space in the micro-reactor. It is the product of the dimensionless surface coverage $\theta_i = \frac{q_i}{q_{max}}$ and the ratio of the maximum concentration of adsorption sites to the pulse intensity, and it is defined as

$\overline{\theta}_i = \theta_i \frac{q_{max}}{N_i / AL\varepsilon_b}$. The dimensionless particle time τ_{p_i}, dimensionless desorption constant $k_{d_i}^*$, and dimensionless equilibrium adsorption constant K_{eq_i} for species i are the three dimensionless constants of the developed model defined as

$$\tau_{p_i} = \frac{L^2 / D_{K_i}}{R_p^2 / D_{e_i}} = \frac{Characteristic\ diffusion\ time\ in\ micro-reactor}{Characteristic\ diffusion\ time\ in\ zeolite\ crystal}, \qquad (3.22)$$

$$k_{d_i}^* = \frac{L^2 / D_{K_i}}{1 / k_{d_i}} = \frac{Characteristic\ diffusion\ time\ in\ micro-reactor}{Characteristic\ desorption\ time}, \qquad (3.23)$$

and

$$K_{eq_i} = q_{max} \frac{1 / k_{d_i}}{1 / k_{a_i}} = \frac{Characteristic\ desorption\ time}{Characteristic\ adsorption\ time}. \qquad (3.24)$$

Equations (3.11), (3.12, a, b, c), (3.19), (3.20), and (3.21 a, b) describe the thin zone reactor configuration and different interactions taking place within the zeolite particles. The three dimensionless constants τ_{p_i}, $k_{d_i}^*$, and K_{eq_i} affect the shape, peak position and height of the model simulated response curve. Attempts were made to reduce the model to a two parameter one (τ_{p_i} and K_{eq_i}) by assuming that the bulk concentrations inside and outside the zeolite pores are in pseudo-equilibrium (Keipert and Baerns, 1998; Delgado et al., 2004; Berger et al., 2008). If in addition one assumes that the intra-particle diffusion is not the rate limiting step, then the model is reduced to only one dimensionless constant, K_{eq_i} (Berger et al., 2008). In this study no such assumptions are made, as our goal is to investigate the use of the single pulse TAP response experiment and of the full model in estimating intra-particle diffusivity and adsorption-desorption constants.

3.4 Solution Procedure

The governing equations for the TAP micro-reactor and zeolite particles are second order PDEs numerically solved by using the method of lines (Schiesser and Silebi, 1997). The method relies on the approximation of spatial derivatives, reducing partial differential equations (PDEs) to sets of ordinary differential equations (ODEs). The resulting ODEs are solved using stiff ODE solvers from NETLIB libraries.

Cubic spline approximation is used to discretize the second order spatial derivatives for the TAP micro-reactor model. Such cubic spline approximation offers a unique advantage by allowing non-uniform spatial grids. Thus, the grid points can be selected to concentrate in the region of the thin zone, where there is rapid variation in $c_i(\tau, \xi)$ with ξ, due to the presence of zeolite particles. Consequently, the number of grid points in the thin zone can be increased without significantly increasing the total number of grid points to solve the TAP micro-reactor model, which, decreases the overall CPU time. Five point biased upwind and central difference approximations are used to discretize the first and second order spatial derivatives, respectively, for the zeolite particle model. The indeterminate form of $\dfrac{2}{\eta}\dfrac{\partial \theta_i}{\partial \eta}$ at $\eta = 0$ due to the boundary condition $\left.\dfrac{\partial \theta_i}{\partial \eta}\right|_{\eta=0} = 0$ can be easily removed by the application of l'Hospital's rule.

3.5. Results and Discussion

In this section the key results are shown and discussed. Section 3.5.1 demonstrates the experimental validation of the assumption of Knudsen diffusion in the inter-particle void of the TAP micro-reactor and the known temperature and molecular weight dependence of effective Knudsen diffusivity under TAP experimental conditions. The sensitivity ranges of the time constants in the developed model are analyzed in section 3.5.2, so we can determine the reliability of the estimated parameters. Section 3.5.3 describes the methodology to tune the experimental conditions to obtain reliable estimates.

3.5.1 Knudsen Diffusivity in the Inter-particle Voids

When an inert gas like argon is pulsed into the TAP micro-reactor containing a zeolite sample, the gas molecules interact weakly on the surface of the particles (both zeolite and nonporous quartz). Olea and Iwasawa, (2004) found that when single pulse of argon was introduced over the micro-porous particles (< 2 nm in diameter), both inter- and intra-particle diffusion affects the response curve. As a result, both inter- and intra-particle diffusivities were needed to represent the argon response curve. These authors used the one-zone micro-reactor configuration and the experiments were performed at or near ambient temperatures (300 K). However, in the present study, the use of the thin zone micro-reactor configuration allows us to neglect the resistance of inter-particle diffusion in the zeolite zone, as the total pore volume of both beta and USY zeolite particles

contributes less than 1% to the total inter-particle void volume. This assumption that only Knudsen diffusivity in the inter-particle voids affects the argon response curve was verified by comparing the experimental peak-normalized response to the theoretical peak-normalized plot (Gleaves et al., 1997). The experimental peak-normalized response curve is obtained by dividing the experimental response with the peak magnitude and plotting it as function of (t/t_m), where t_m is the time at which the maximum occurs. The theoretical peak-normalized plot (equation 3.25) is obtained from the series solution of the continuity equation assuming only Knudsen diffusion in the inter-particle void (Gleaves et al., 1997).

$$\frac{E_i(t)}{E_i^{max}(t)} = 1.70 \sum_{n=0}^{\infty} (-1)^n (2n+1) \exp(-(n+0.5)^2 \pi^2 \frac{t}{6t_m}). \tag{3.25}$$
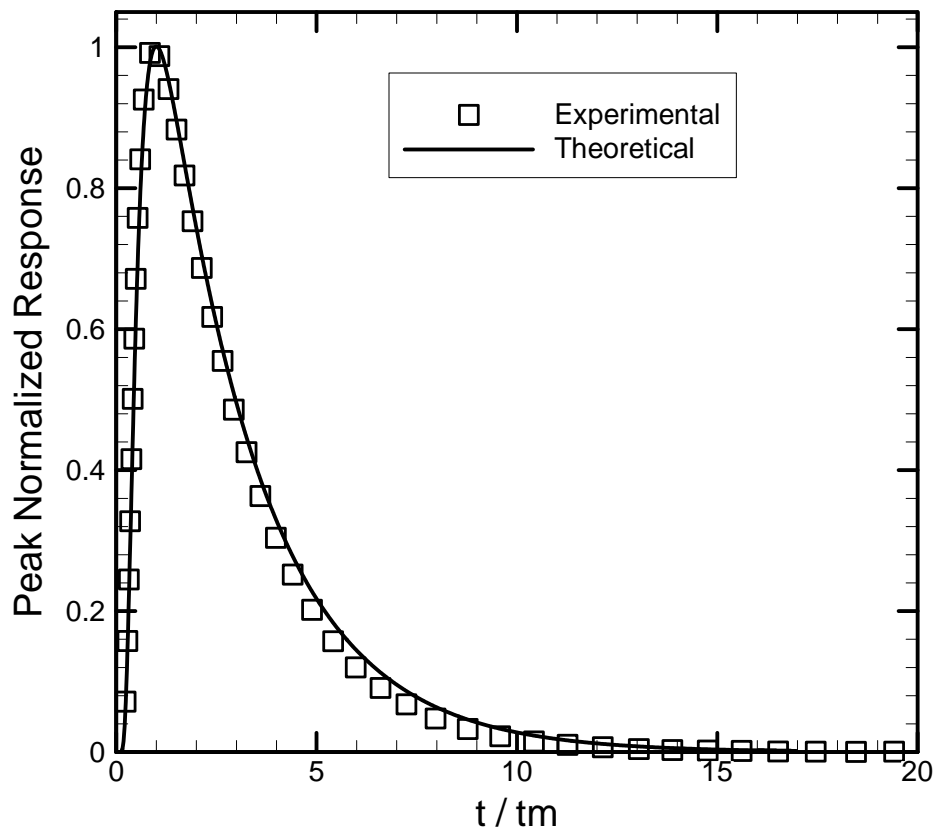
Figure 3.5: Comparison of experimental peak-normalized response of argon when pulsed over the thin zone micro-reactor containing beta zeolite at 373 K and theoretical peak normalized plot.

Figure 3.5 shows the comparison of the experimental peak-normalized response of argon when pulsed over the thin zone micro-reactor containing beta zeolite at 373 K with the theoretical peak normalized plot. A good match is found between the experimental and model predicted peak-normalized plots. Similar results are also found for the temperature range used in this study and when argon is pulsed over the micro-reactor with a thin zone

of USY zeolite. Hence, argon is used to estimate the effective Knudsen diffusivity in the inter-particle voids.

The effective Knudsen diffusivity of any other probe molecule is then computed by using the known temperature and molecular weight dependence of Knudsen diffusivity which is $D_{K_i} \propto \sqrt{T/Mw_i}$. To verify this dependency under TAP experimental conditions single pulses of argon and isobutane are introduced into the evacuated micro-reactor packed with inert particles (nonporous quartz) at various temperatures. The experiments are repeated to check for the reproducibility of the experimental data. The characteristic diffusion times in the micro-reactor for each pulse are calculated from the method of moments approach. Here the jth moment is defined as $M_j = \int_0^\infty E(t) \times t^j \, dt$. Here $E(t)$ is the experimental response obtained from the TAP reactor in real time t. The mean residence time of the response curve is determined by dividing the first moment (M_1) with the zeroth moment (M_0). In the case of strictly Knudsen diffusion with diffusivity D_{K_i} in the inter-particle space the mean residence time is the characteristic diffusion time of the probe molecule under investigation in the micro-reactor. Thus, for species i, the characteristic diffusion time in the reactor is

$$\frac{L^2 \varepsilon_b}{D_{K_i}} = \frac{\int_0^\infty E_i(t) \times t \, dt}{\int_0^\infty E_i(t) \, dt}. \tag{3.26}$$

71

Here, L is the length of the TAP micro-reactor (33×10^{-03} m) and ε_b is the bed porosity

(~0.38), which is measured independently.

It is found that the relative error of the characteristic diffusion time in the micro-reactor for each pulse of argon and isobutane at each temperature is less than 2.5 %. In the nonporous quartz bed, at temperatures above ambient, both argon and isobutane interact only weakly on the surface of the particles and the characteristic diffusion time of the micro-reactor reflects only the transport process in the inter-particle voids which has been established to be Knudsen diffusion (Gleaves et al., 1997; Keipert and Baerns, 1998; Nijhuis et al., 1999).

Figure 3.6 shows the characteristic diffusion times in the micro-reactor for isobutane and

argon, divided by the square root of their respective molecular weights $\dfrac{L^2 \varepsilon_b / D_{K_i}}{\sqrt{Mw_i}}$, as a

function of the inverse square root of temperature. Figure 3.6 clearly demonstrates that the characteristic diffusion times of isobutane and argon in the micro-reactor follow the square root of temperature and square root of molecular weight dependencies in the given temperature range. Furthermore, extrapolating the line that connects all the experimental data points in Figure 3.6 leads to zero intercept on the ordinate, as it should, and the line has a positive slope. This confirms that the inter-particle transport in the TAP micro-reactor can be characterized as Knudsen diffusion.
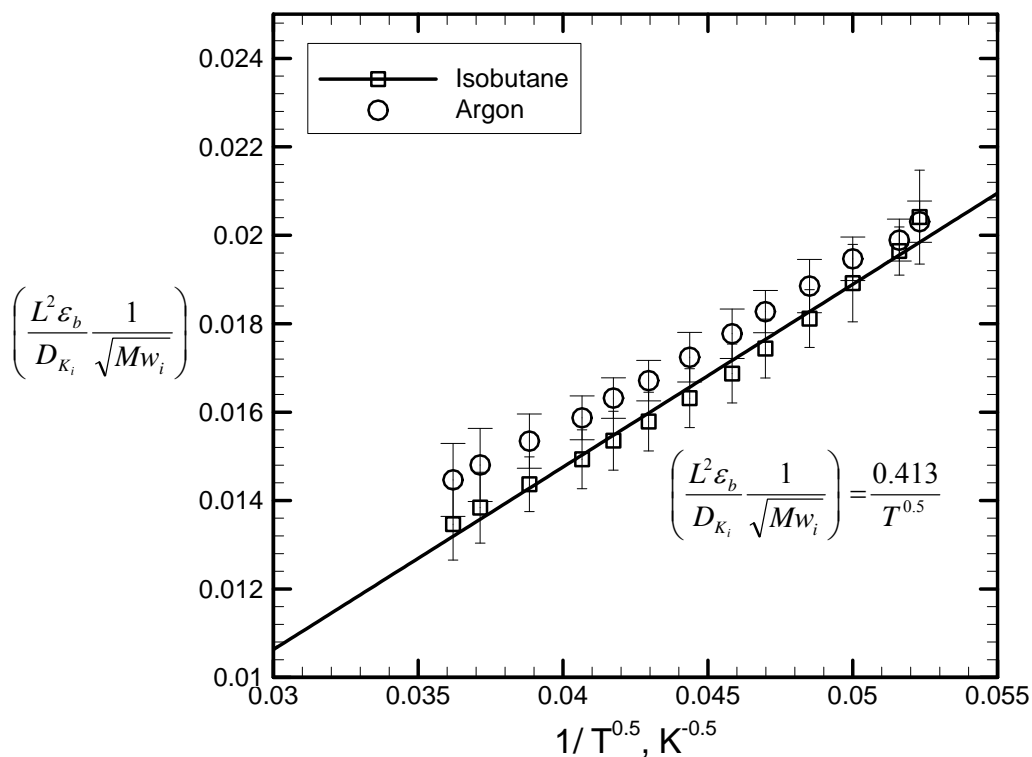
Figure 3.6: The characteristic diffusion times in the micro-reactor of isobutane and argon, divided by the square root of their respective molecular weights, as a function of the inverse square root of temperature. The micro-reactor was packed with non-porous quartz particles (total mass = 800 mg and mean diameter = 200 μm).

Consequently, in this study for a thin zone TAP micro-reactor packed with beta or USY zeolite the effective Knudsen diffusivities in the inter-particle voids for isobutane n-butane, 2,2,4-trimethylpentane and 2,5-dimethylhexane are estimated from argon response curve. These values are reported in Chapter 4.

73

3.5.2 Sensitivity Analysis of Dimensionless Constants

In transient experimental techniques such as TAP, only certain ranges of intra-particle diffusion and adsorption-desorption constants can be determined (Keipert and Baerns, 1998; Nijhuis et al., 1999; Berger et al., 2008). Keipert and Baerns, (1998) found the intra-particle diffusivity range within which its values affect the shape of the TAP response curves. They did this by simulating the response curves for varied intra-particle diffusivities while other parameters were kept constant. A similar approach is adopted in this study. In the model the three dimensionless constants τ_{p_i}, K_{eq_i}, and $k_{d_i}^*$ affect the shape of the TAP response curve. Simulations were carried out at τ_{p_i}, K_{eq_i}, and $k_{d_i}^*$ of different orders of magnitudes to discriminate between the time scales of intra-particle diffusion, adsorption-desorption, and inter-particle diffusion. The mean and variance of the simulated response curves were calculated to find the ranges of τ_{p_i}, K_{eq_i}, and $k_{d_i}^*$ within which the response curve is sensitive to their values. Here, the mean and variance of the response curve are defined as

$$\bar{\tau} = \frac{\int_0^\infty F_i^*(\tau) \times \tau \, d\tau}{\int_0^\infty F_i^*(\tau) \, d\tau}, \tag{3.27}$$

and

$$\sigma^2 = \frac{\int\limits_0^\infty F_i^*(\tau) \times \tau^2 \; d\tau}{\int\limits_0^\infty F_i^*(\tau) \; d\tau} - \overline{\tau}^2 \; . \qquad\qquad (3.28)$$

Figures 3.7 a and b display some of the calculations performed and clearly establish that asymptotic values of the moments of the response at some very small or very large parameter values preclude reliable estimates of these constants. These parametric sensitivity studies established that the above constants must be in the ranges indicated in Table 3.1 for the reliable estimation of various parameters to be possible. Since the values of these dimensionless groups cannot be known 'a priori', this implies that proper estimation of system parameters by TAP will require an iterative approach. The values of the dimensionless constants have to be first estimated based on prior experience and the experiment designed based on these estimates so as to ensure that these constants fit in the ranges indicated in Table 3.1. Upon processing the experimental results if some constants were found outside the permissible range, the experiment should be redesigned to bring them into range. Unfortunately, we did not have access to the TAP equipment long enough to complete this iterative process and thus report only the results obtained with the original experimental design described earlier.

Table 3.1: The upper and lower limits of the dimensionless parameters τ_{p_i}, K_{eq_i}, and $k^*_{d_i}$
that affect the shape of the TAP response curve.

Dimensionless time constants	Lower limit	Upper limit
τ_{p_i}	10^{-6}	10^0
$k^*_{d_i}$	10^{-2}	10^0
K_{eq_i}	10^0	N/A
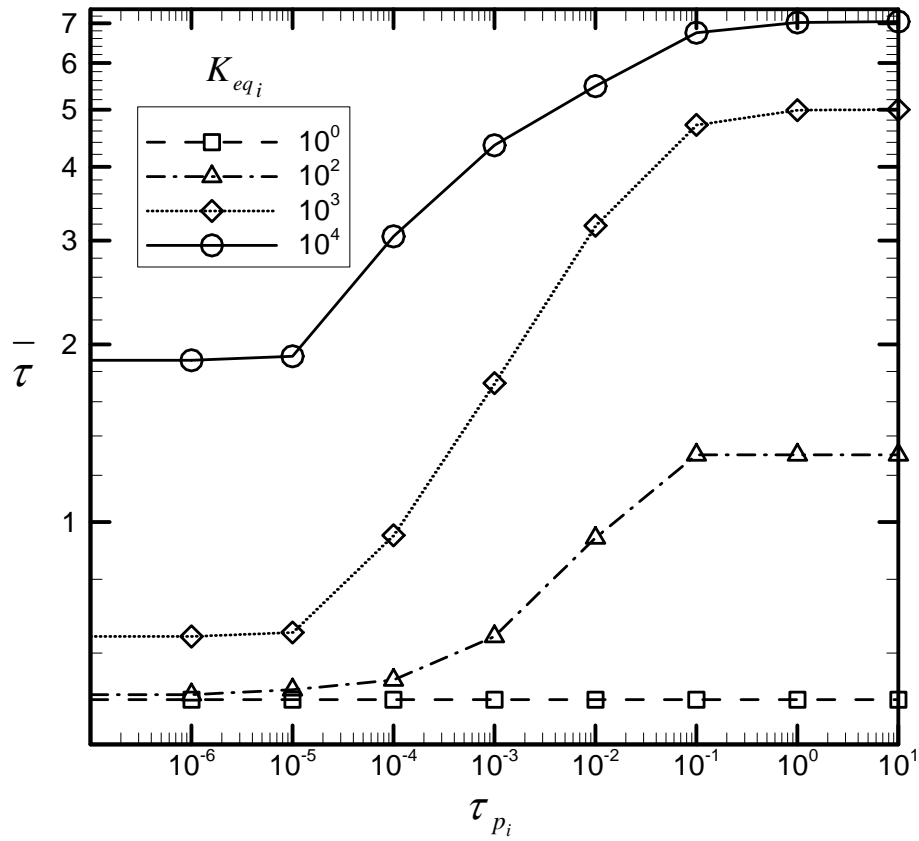
(a)
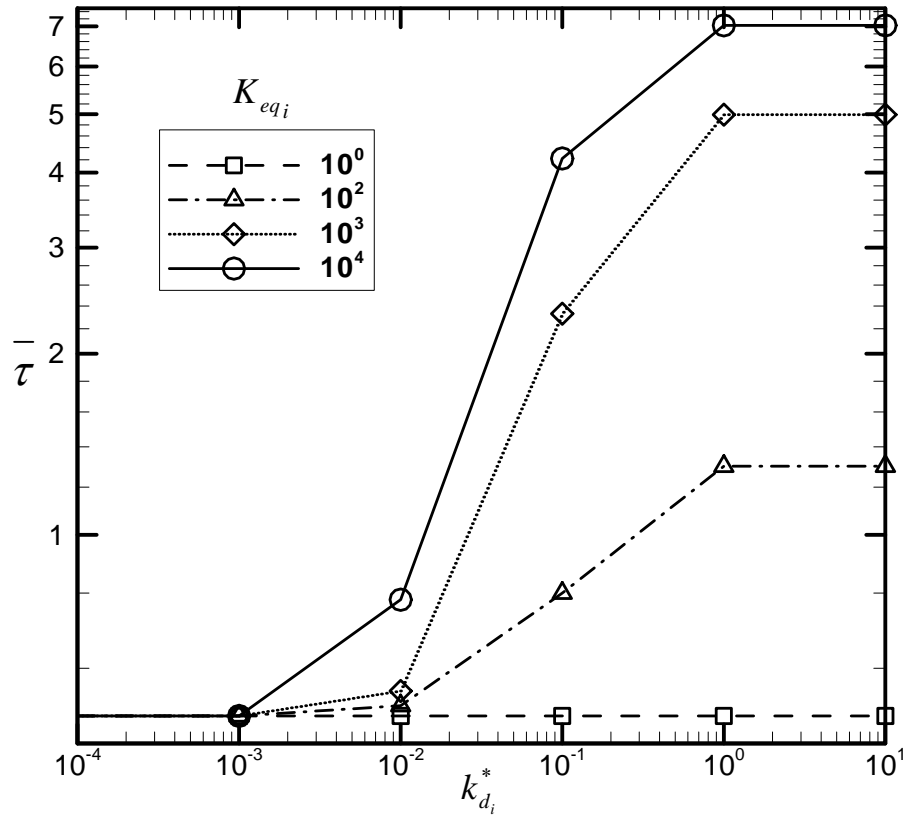
(b)

Figure 3.7: Results of numerical experiments. (a) calculated means $(\bar{\tau})$ of the simulated response curves as the function of dimensionless time constants τ_{p_i}, and K_{eq_i}. (b) calculated means $(\bar{\tau})$ of the simulated response curves as the function of dimensionless time constants $k_{d_i}^*$, and K_{eq_i}.

As an illustration of the physical reasoning as to why certain parameters cannot always be estimated from the TAP response curve, consider the range of the dimensionless τ_{p_i} for different values of K_{eq_i} as shown in Figure 3.7 a. As mentioned earlier, the dimensionless τ_{p_i} is the ratio of the characteristic diffusion time in the micro-reactor to the characteristic diffusion time in the zeolite pores. A value of τ_{p_i} equal to unity means that the time scales for intra-particle and inter-particle diffusion are the same, and that the characteristic diffusion time in the zeolite particles is not a rate limiting parameter. In this case, the concentration gradient in the intra-particle space is negligible and the effective intra-particle diffusivity of adsorbed species is fast. When the effective intra-particle diffusivity of adsorbed species is very small, for example in the case of τ_{p_i} equals 10^{-6}, the difference in time scales for intra-particle and inter-particle diffusion is very large. Under this limiting case, most of the flux of the adsorbing species reaches the micro-reactor outlet before considerable diffusion can occur in the zeolite pores. Similar limitations are also observed in other the transient experiments, such as ZLC (Ruthven and Lee, 1981) and TEOM (Lee et al., 2004).

Figure 3.7 a also illustrates the effects of the dimensionless equilibrium constant K_{eq_i} on the mean residence time $(\bar{\tau})$ over a range of τ_{p_i}. The range of τ_{p_i} that affects the value of the mean residence time is not affected by different K_{eq_i} values. One exception is when K_{eq_i} is unity and in that case the mean residence time is unaffected by values of τ_{p_i} over

the whole range. At larger values of K_{eq_i}, the calculated mean values of the simulated response curves increase as the K_{eq_i} value increases. Consequently, there is no upper limit on K_{eq_i} that makes the response insensitive to its value. The value of K_{eq_i} equal to unity represents the case when the characteristic desorption time is equal to characteristic adsorption time; hence the species is weakly adsorbed. This is particularly true in the case of a noble gas such as argon. Here the shape of the response curve is not affected over the entire range of slow to fast effective intra-particle diffusivity (relative to Knudsen diffusion in the bed). This further justifies the use of argon in the current experiments. Similar effects are also observed for the dimensionless constant $k_{d_i}^*$ schematized in Figure 3.7 b.

3.5.3 Tuning Experimental Conditions to Get Reliable Estimates

The range of dimensionless model constants reported in Table 3.1 indicates the parameter space within which the model can reliably estimate the quantities we are seeking, e.g. intra-particle diffusivity and adsorption–desorption constants. This range of the dimensionless constants cannot be altered; therefore the experimental conditions should be tuned so that the estimated parameters τ_{p_i} and $k_{d_i}^*$ fall within their desired ranges reported in Table 3.1. Accordingly the following alterations of the experimental conditions are proposed. For probe molecules with low intra-particle diffusivities, represented by the lower limit of time constant τ_{p_i}, the value of τ_{p_i} can be augmented by

decreasing the zeolite particle size, by increasing the micro-reactor length, or by decreasing the Knudsen diffusivity in the inter-particle voids in the bed by using smaller inert particles in the micro-reactor. In contrast, for fast diffusing probe molecules in the intra-particle space, represented by the upper limit in the permissible range , the lower value of τ_{p_i} is achieved by doing exactly the opposite. Similarly, by altering the micro-reactor length and Knudsen diffusivity in the inter-particle void, the experiments can be tuned so that $k_{d_i}^*$ falls within the required range. These alterations in the experimental conditions should provide guidance for future single pulse TAP experiments to obtain reliable estimates of intra-particle diffusivity and adsorption-desorption constants.

3.6 Conclusions

The thin zone TAP micro-reactor experiments are used to observe adsorption-desorption dynamics for isobutane, n-butane, 2,24-trimethylpentane and 2,5-dimethlyhexane and evaluate their pertinent parameters in beta and USY zeolites. Under the ultra high vacuum condition in the TAP micro-reactor, the inter-particle transport occurs in the Knudsen regime and can be well characterized by the single effective Knudsen diffusivity of the probe molecule. Furthermore, the estimates of the intra-particle diffusion and adsorption-desorption constants are carried out in the absence of external mass transfer resistance, without influence of a carrier stream, and at constant temperature. It was found that the inert gas argon was sufficient to obtain Knudsen diffusivity in the inter-particle void, as the time spent by argon in the intra-particle zeolite space was negligible.

The effective Knudsen diffusivity of isobutane, n-butane, 2,2,4-trimethylpentane and 2,5-dimethlyhexane is then computed by using the known temperature and molecular weight dependence $D_{K_i} \propto \sqrt{T/Mw_i}$.

It is established that various system parameters can only be reliably estimated form a single pulse TAP experiment in a thin zone micro-reactor when the three dimensionless constants of the model fall into certain ranges. Since these constants are not known 'a priori', reliable estimation of system parameters may involve an iterative procedure of experimental design and data interpretation to establish the range of constants needed for reliable estimates. However, TAP offers opportunities for quantification of dynamics of transport and adsorption–desorption in the particles if the experimental design is carefully chosen.

The simulated TAP response curves were fitted to the experimentally obtained ones for isobutane, n-butane, 2,2,4-trimethylpentane and 2,5-dimethlyhexane in beta and USY zeolites by adjusting the three model parameters τ_{p_i}, K_{eq_i}, and $k_{d_i}^*$. The estimated values of these parameters and the pertinent discussion are reported in Chapter 4.

Acknowledgement

Nomenclature

A cross sectional area of micro-reactor, m^2

a_i absolute calibration factor, moles/ Mv

C_i bulk concentration of species i, moles/ m^3

c_i pulse-normalized bulk concentration

D diffusivity, m^2/ sec

D_{e_i} effective diffusivity in the intra-particle space defined as $D_{e_i} = \dfrac{\varepsilon_p}{\varsigma_p} D_{T_i}$ m^2/ sec

D_{K_i} effective Knudsen diffusivity, m^2/ sec

D_{MS_i} Maxwell-Stefan diffusivity, m^2/ sec

D_{T_i} Fickian diffusivity, m^2/ sec

$E_i(t)$ time dependent intensity measured by the mass spectrometer, Mv/ sec

$E_i^{max}(t)$ maximum peak intensity measured by the mass spectrometer, Mv/ sec

$F_i(t)$ exit molecular flow, moles/ sec

$F_i^*(t)$ dimensionless exit flow

f_i fugacity, Pa

J_i molar flux of species i, moles/ m^2-sec

k_{a_i} adsorption constant, m^3/ moles-sec

k_{d_i} desorption constant, 1/ sec

$k_{d_i}^*$ dimensionless desorption constant

K_{eq_i} dimensionless equilibrium adsorption constant

L micro-reactor length, m

Mw_i molecular weight of species i, kg/ moles

M_j j$^{\text{th}}$ moment

N_i number of moles

q_i adsorbed phase concentration, moles/ m^3

$q_{\max}$ maximum concentration of adsorption sites, moles/ m^3

R universal gas constant, kJ/ moles-K

R_p zeolite particle radius

$\bar{r}$ mean inter-particle distance, m

T Temperature, K

t observation time, sec

t_m time at which the peak maximum occurs, sec

$\bar{t}$ mean of the dimensionless response curve

$\left\langle x^2(t) \right\rangle$ mean square displacement

Greek letters

θ_i dimensionless surface coverage or fraction surface coverage

$\bar{\theta}_i$ pulse-normalized surface coverage

$\delta^*(\tau)$ pulse-normalized delta function defined as $\delta^*(\tau) = \dfrac{\varepsilon_b L^2}{D_{K_i}} \delta(t)$

τ dimensionless time

τ_{p_i} dimensionless particle time defined as $\dfrac{L^2 / D_{K_i}}{R_p^2 / D_{e_i}}$

μ_i chemical potential of species i

Γ thermodynamic correction factor

ξ dimensionless spatial distance within the micro-reactor

η dimensionless spatial distance within the zeolite particle

ε_b solid holdup

ε_p zeolite particle porosity

ζ_p particle tortuosity

σ^2 variance of the dimensionless response curve

References

Anderson, B. G., F. J. M. M. de Gauw, N. J. Noordhoek, L. J. van Ijzendoorn, R. A. van Santen and M. J. A. de Voigt (1998). "Mass transfer of alkanes in zeolite packed-bed reactors studied with positron emission profiling (pep). 1. Experiments." Industrial & Engineering Chemistry Research 37(3): 815-824.

Bárcia, P. S., J. A. C. Silva and A. E. Rodrigues (2005). "Adsorption equilibrium and kinetics of branched hexane isomers in pellets of beta zeolite." Microporous and Mesoporous Materials 79(1-3): 145-163.

Bárcia, P. S., J. A. C. Silva and A. E. Rodrigues (2007). "Separation of branched hexane isomers using zeolite bea for the octane improvement of gasoline pool." Studies in Surface Science and Catalysis Volume 170, Part 1: 955-960.

Berger, R. J., F. Kapteijn, J. A. Moulijn, G. B. Marin, J. De Wilde, M. Olea, D. Chen, A. Holmen, L. Lietti, E. Tronconi and Y. Schuurman (2008). "Dynamic methods for catalytic kinetics." Applied Catalysis, A: General 342(1-2): 3-28.

de Jong, K.P., Mesters, C.M.A.M., Peferoen, D.G.R., van Brugge, P.T.M. and de Groote, C., (1996). Paraffin alkylation using zeolitie catalysts in a slurry reactor: Chemical engineering principles to extend catalyst lifetime. Chem. Eng. Sci. 51, 2053.

Delgado, J. A., T. A. Nijhuis, F. Kapteijn and J. A. Moulijn (2004). "Determination of adsorption and diffusion parameters in zeolites through a structured approach." Chemical Engineering Science 59(12): 2477-2487.

Denayer, J. F., G. V. Baron, J. A. Martens and P. A. Jacobs (1998a). "Chromatographic study of adsorption of n-alkanes on zeolites at high temperatures." Journal of Physical Chemistry B 102(17): 3077-3081.

Denayer, J. F., W. Souverijns, P. A. Jacobs, J. A. Martens and G. V. Baron (1998b). "High-temperature low-pressure adsorption of branched c5−c8 alkanes on zeolite beta, zsm-5, zsm-22, zeolite y, and mordenite." Journal of Physical Chemistry B 102(23): 4588-4597.

Eic, M. and D. M. Ruthven (1988). "A new experimental technique for measurement of intracrystalline diffusivity." Zeolites 8(1): 40-45.

Gleaves, J. T., G. S. Yablonskii, P. Phanawadee and Y. Schuurman (1997). "Tap-2: An interrogative kinetics approach." Applied Catalysis, A: General 160(1): 55-88.

Gong, K. (2008). Adsorption/desorption studies on solid acid alkylation catalysts using a tapered element oscillating microbalance (teom), University of Kansas. Ph.D.

Hagelstein, M., U. Hatje, H. Förster, T. Ressler and W. Metz (1994). "Dexafs studies on the diffusion of ammonia into zeolite cunay." Studies in Surface Science and Catalysis Volume 84, Part 2: 1217-1222.

Iyengar, V. and M.-O. Coppens (2004). "Dynamic monte-carlo simulations of binary self-diffusion in zeolites: Effect of strong adsorption sites." Chemical Engineering Science 59(22-23): 4747-4753.

Karge, H. G. and W. Nießen (1991). "A new method for the study of diffusion and counter-diffusion in zeolites." Catalysis Today 8(4): 451-465.

Karger, J. and D. M. Ruthven (1992). Diffusion in zeolites and other microporous solids. New York, John Wiley and Sons.

Keipert, O. P. and M. Baerns (1998). "Determination of the intracrystalline diffusion coefficients of alkanes in h-zsm-5 zeolite by a transient technique using the temporal-analysis-of-products (tap) reactor." Chemical Engineering Science 53(20): 3623-3634.

Lee, C. K., S. Ashtekar, L. F. Gladden and P. J. Barrie (2004). "Adsorption and desorption kinetics of hydrocarbons in fcc catalysts studied using a tapered element oscillating microbalance (teom). Part 1: Experimental measurements." Chemical Engineering Science 59(5): 1131-1138.

Lima, P. M., C. V. Gonçalves, C. L. Cavalcante Jr and D. Cardoso (2008). "Sorption kinetics of linear paraffins in zeolite bea nanocrystals." Microporous and Mesoporous Materials 116(1-3): 352-357.

Mittelmeijer-Hazeleger, M. C., A. F. P. Ferreira and A. Bliek (2002). "Influence of helium and argon on the adsorption of alkanes in zeolites." Langmuir 18(25): 9613-9616.

Nijhuis, T. A., L. J. P. van den Broeke, M. J. G. Linders, J. M. van de Graaf, F. Kapteijn, M. Makkee and J. A. Moulijn (1999). "Measurement and modeling of the transient adsorption, desorption and diffusion processes in microporous materials." Chemical Engineering Science 54(20): 4423-4436.

Olea, M. and Y. Iwasawa (2004). "Transient studies on carbon monoxide oxidation over supported gold catalysts: Support effects." Applied Catalysis, A: General 275(1-2): 35-42.

Plant, D. F., G. Maurin, I. Deroche, L. Gaberova and P. L. Llewellyn (2006). "Co2 adsorption in alkali cation exchanged y faujasites: A quantum chemical study compared to experiments." Chemical Physics Letters 426(4-6): 387-392.

Raghavan, N. S. and D. M. Ruthven (1983). "Numerical simulation of a fixed-bed adsorption column by the method of orthogonal collocation." AIChE Journal 29(6): 922-925.

Raghavan, N. S. and D. M. Ruthven (1985). "Simulation of chromatographic response in columns packed with bidisperse structured particles." Chemical Engineering Science 40(5): 699-706.

Ruthven, D. M. and L.-K. Lee (1981). "Kinetics of nonisothermal sorption: Systems with bed diffusion control." AIChE Journal 27(4): 654-663.

Sarsani, V.S.R., (2007). Solid acid catalysis in liquid, gas-expanded liquid and near critical reaction media: Investigation of isobutane/ butene alkylation and aromatic acylation reactions. Ph D. Dissertation, University of Kansas.

Schiesser, W. E. and C. A. Silebi (1997). <u>Computational transport phenomena : Numerical methods for the solution of transport problems</u>. Cambridge, U.K., Cambridge University Press.

Schuurman, Y., C. Delattre, I. Pitault, J. P. Reymond and M. Forissier (2005). "Effect of coke deposition on transport and sorption in fcc catalysts studied by temporal analysis of products." Chemical Engineering Science 60(4): 1007-1017.

Skoulidas, A. I. and D. S. Sholl (2003). "Molecular dynamics simulations of self-diffusivities, corrected diffusivities, and transport diffusivities of light gases in four silica zeolites to assess influences of pore shape and connectivity." The Journal of Physical Chemistry A 107(47): 10132-10141.

Smith, J. M. (1981). <u>Chemical engineering kinetics</u>. New York, McGraw-Hil.

Simpson M. F., Wei J., and Sundaresan S., (1996). Kinetic Analysis of Isobutane/Butene Alkylation over Ultrastable H-Y zeolite. Ind. Eng. Chem. Res. 35, 3861-3873.

Truitt, M. J. and J. L. White (2009). "In-situ nmr studies of isobutane activation and exchange in zeolite beta." Solid State Nuclear Magnetic Resonance 35(2): 100-103.

Wender, A., A. Barreau, C. Lefebvre, A. Di Lella, A. Boutin, P. Ungerer and A. Fuchs (2007). "Adsorption of n-alkanes in faujasite zeolites: Molecular simulation study and experimental measurements." Adsorption 13(5): 439-451.

Zhang, J., Z. Zhao, A. Duan, G. Jiang, J. Liu and D. Zhang (2009). "Chromatographic study on the adsorption and diffusion of light hydrocarbons in zsm-5 and usy zeolites." Energy & Fuels 23(2): 617-623.

Zheng, X., J. T. Gleaves, G. S. Yablonsky, T. Brownscombe, A. Gaffney, M. Clark and S. Han (2008). "Needle in a haystack catalysis." App. Cat. A. 341(1-2): 86-92.

Zou, B., M. P. Dudukovic and P. L. Mills (1993). "Modeling of evacuated pulse micro-reactors." Chemical Engineering Science 48(13): 2345-2355.

CHAPTER 4

Estimation of Intra-particle Diffusivity, and Adsorption-Desorption and Equilibrium Constants in Beta and USY Zeolites in Alkylation Processes

Excerpts of this chapter have been submitted to Journal of Catalysis

Abstract

The dimensionless equilibrium constant, apparent heats of adsorption, intra-particle diffusivities and activation energies at very low surface coverage are determined for the reactants, products and byproducts of alkylation processes in beta and USY zeolite. Two different adsorption-desorption dynamics were observed in these zeolites: (1) straight and zig-zag channels of beta zeolite exhibit similar affinity for adsorbing branched and straight C_4 alkanes and, stronger affinity for adsorbing dimethyl-branched over trimethyl-branched C_8 isoalkanes, (2) super cages of USY zeolite exhibit stronger affinity for adsorbing straight chain C_4 alkanes and similar affinity for adsorbing dimethyl-branched and trimethyl-branched C_8 isoalkanes. Based on this understanding, it is concluded that the ideal solid acid catalyst for alkylation processes should feature some characteristics of beta and USY zeolites to increase product selectivity and decrease the rate of deactivation.

4.1 Introduction

Zeolites are crystalline aluminosilicates whose composition is very similar to sand. Zeolites have a wide range of applications in the field of catalytic processes and adsorptive separation techniques (Karger et al., 2005). Most of the commercial zeolites are bound together using inorganic binders to form macro-porous pellets (Ruthven, 1984), giving rise to a wide range of pore sizes (pore sizes: > 2 nm to < 50 nm) in such pellets and different transport mechanism inside different diameter pores (Karger and Ruthven, 1992; Van Den Broeke and Krishna, 1995; Krishna and Wesseling, 1997; Kacznarski et al., 2003).

The key role on catalytic processes and adsorptive separation techniques of nano-pore diffusion (especially in pore sizes < 2 nm) and adsorption/ desorption dynamics in zeolites is widely acknowledged (Karger and Ruthven, 1992). In alkylation processes catalyzed by zeolites, these phenomena are often responsible for reduced catalytic activity and selectivity (Simpson et al., 1996; Martinis and Forment, 2006).

Several important questions about alkylation processes catalyzed by zeolites remain to be answered. How do organic molecules diffuse inside a nano-porous zeolite? How does the pore morphology of a zeolite influence diffusion, adsorption/ desorption and reaction pathway of organic molecules?

This study is devoted to improve the basic understanding of diffusion and adsorption/ desorption in a nano-porous host system. As stated earlier, nano-porous zeolites have multiple applications; however, this study focuses on phenomena related to the alkylation of isobutane and n-butene in nano-porous zeolites. Beta zeolite (de Jong et al., 1996; Sarsani 2007) and ultrastable Y zeolite (USY) (Simpson et al., 1996,) have exhibited high product selectivity and relatively long activity on stream for alkylation reactions. Thus, these two zeolites are selected for this study. The probe molecules tested are basically the reactants, products and byproducts of the alkylation reactions.

Single pulse TAP experiments with thin zone reactor configuration, as described in the Chapter 3 (Section 3.2), are employed to indentify the different phenomena taking place in the zeolite particle. The effective Knudsen diffusivities in the inter-particle voids of the adsorbing species are independently measured from the argon response curve by the procedure described in Chapter 3 (Section 3.5.1). To estimate the model parameters τ_{p_i}, K_{eq_i}, and $k_{d_i}^*$ the thin zone reactor model developed in the Chapter 3 (Equations (3.11), (3.12, a, b, c), (3.19), (3.20), and (3.21 a, b)) is numerically solved. The simulated TAP response curves are then fitted to the experimentally obtained ones by adjusting these three model parameters. The values of the estimates which fall with the prescribed range (Table 3.1) are only reported here. The definitions of the dimensionless constant are

$$\tau_{p_i} = \frac{L^2 / D_{K_i}}{R_p^2 / D_{e_i}} = \frac{Characteristic\ diffusion\ time\ in\ micro-reactor}{Characteristic\ diffusion\ time\ in\ zeolite\ pore}, \qquad (4.1)$$

$$k_{d_i}^* = \frac{L^2 / D_{K_i}}{1/k_{d_i}} = \frac{Characteristic\ diffusion\ time\ in\ micro-reactor}{Characteristic\ desorption\ time}, \qquad (4.2)$$

and

$$K_{eq\,i} = q_{max} \frac{1/k_{d_i}}{1/k_{a_i}} = \frac{Characteristic\ desorption\ time}{Characteristic\ adsorption\ time}. \qquad (4.3)$$

The organization structure of this chapter is as follows. Section 4.2 describes the physical and chemical properties of beta and USY zeolites and the probe molecules tested in this study. The method of moments used to estimate effective Knudsen Diffusivities and their values are reported in Section 4.3. The minimization method for estimating τ_{p_i}, $K_{eq\,i}$, and $k_{d_i}^*$ is described in Section 4.4. The key results with pertinent discussions are reported in Section 4.5. The rational design of ideal solid acid catalyst is discussed in Section 4.6. The conclusion of this work is provided in Section 4.7.

4.2 Physical and Chemical Properties

4.2.1 Beta and USY zeolites

The beta and USY zeolites used in our experiments were obtained from GRACE Davison. The beta zeolite (SMR 5-9858-01062) has a Si/Al ratio of 13, and the USY zeolite (SMR 5-9858-01061) has Si/Al ratio of 3, indicating that the beta zeolite has lower concentration of Brønsted acid sites than USY zeolite. This claim is supported by

our ammonia temperature-program desorption experiments where we found that the acidity of beta zeolite is 291 μmole NH_3/g catalyst and USY zeolite is 466 μmole NH_3/g catalyst.
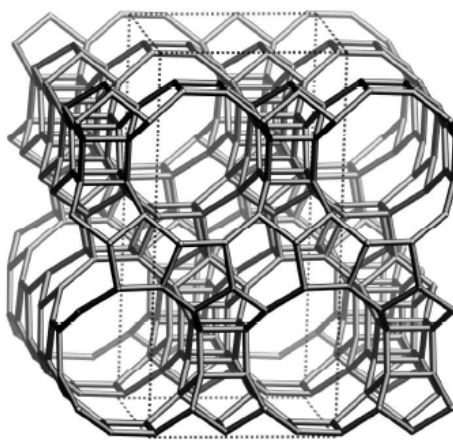
(a) Framework of beta-zeolite viewed along [010]
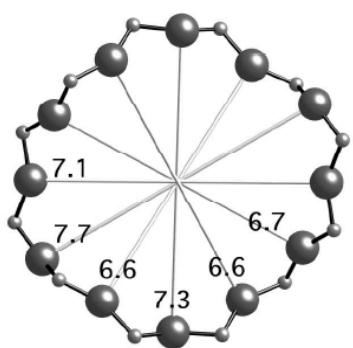
Viewed along [100] and [010]   Viewed along [001]
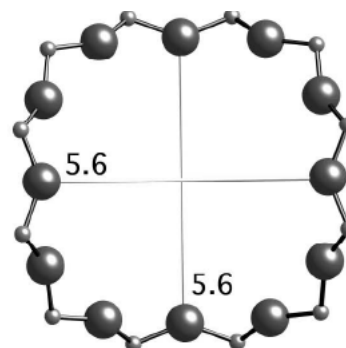
(b) 12-member ring of beta-zeolite

Figure 4.1: Framework and free aperture of straight and zigzag channels of beta-zeolites

(Baerlocher et. al., 2001)

Beta-zeolite framework (Figure 4.1a) consists of straight 12-member-ring channels of free aperture 0.66 x 0.71 nm, viewed along axes [100] and [010] (Figure 4.1b) and zig-zag 12-member-ring channels of free aperture 0.56 x 0.56 nm, viewed along axes [001] (Figure 4.1b) (Baerlocher et. al., 2001). Note: Figure 4.1 is not drawn to scale and in Figure 4.1b the big circular atoms represent the oxygen atoms.

USY zeolite framework (Figure 4.2a) consists of 12-member-ring channels of free aperture 0.74 x 0.74 nm viewed along axes [111] (Figure 4.2b), and a super cage of free aperture of 1.23 x 1.23 nm (Baerlocher et. al., 2001). Note: Figure 4.2 is not drawn to scale, and in Figure 4.2b the big circular atoms represent the oxygen atoms.
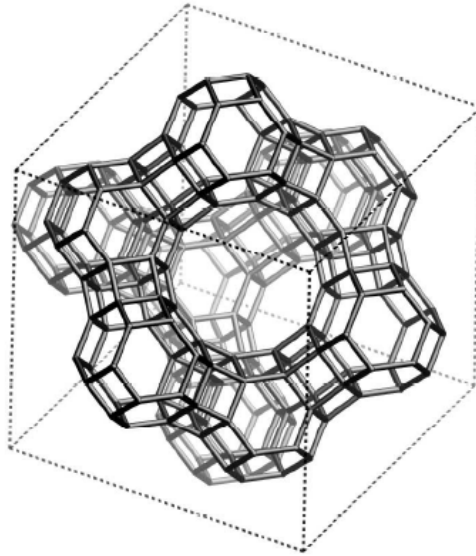
(a) Framework of USY zeolite viewed along [111]
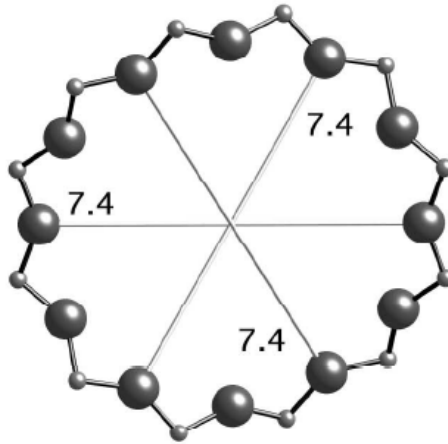
(b) 12-member ring of USY viewed along [111]

Figure 4.2: Framework and free aperture of 12-member ring channels of USY zeolites.

(Baerlocher et. al., 2001)

The chemical composition and basic physical properties of both zeolites are shown in Table 4.1. As indicated by SEM images, the average particle size of beta zeolites is ~ 5 μm, (see Figure 4.3 a) and the average crystal size is ~ 0.3 μm, (see Figure 4.3 b) while the average particle size of USY zeolites is ~ 5 μm, (see Figure 4.4 a) and the average crystal size is ~ 0.25 μm (see Figure 4.4 b). The XRD analysis showed absence of inorganic binder in both zeolites indicating that the zeolite particles are self-aggregates of small crystals.
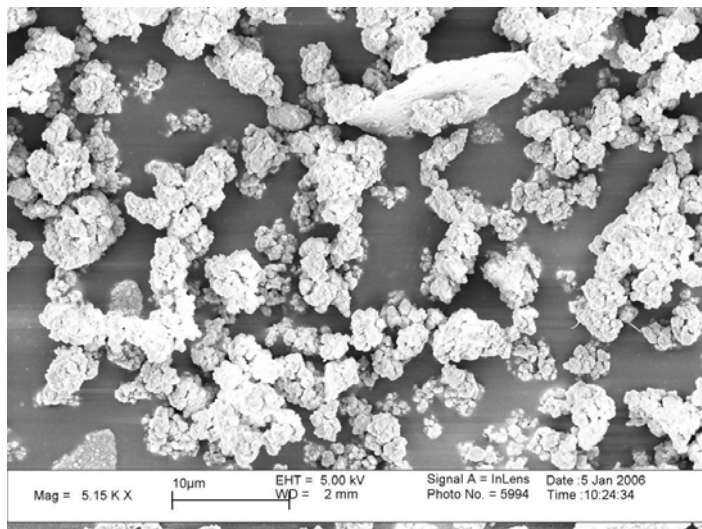
(a)
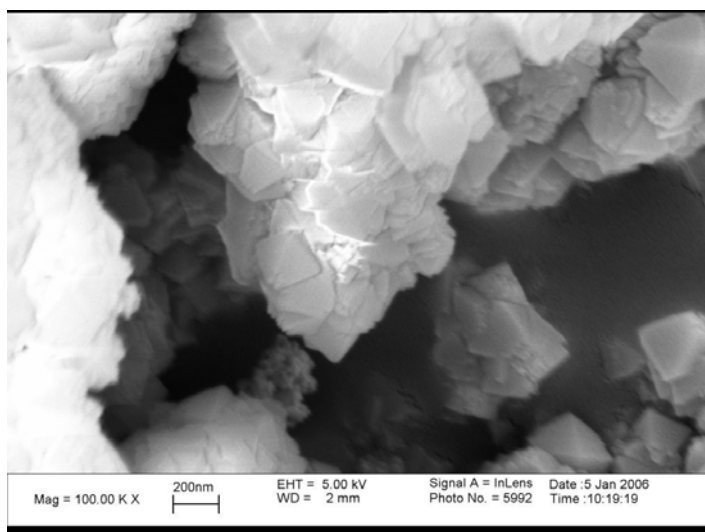
(b)

Figure 4.3: SEM images, (a) showing particle size distribution and (b) showing the

crystallites of beta zeolite.
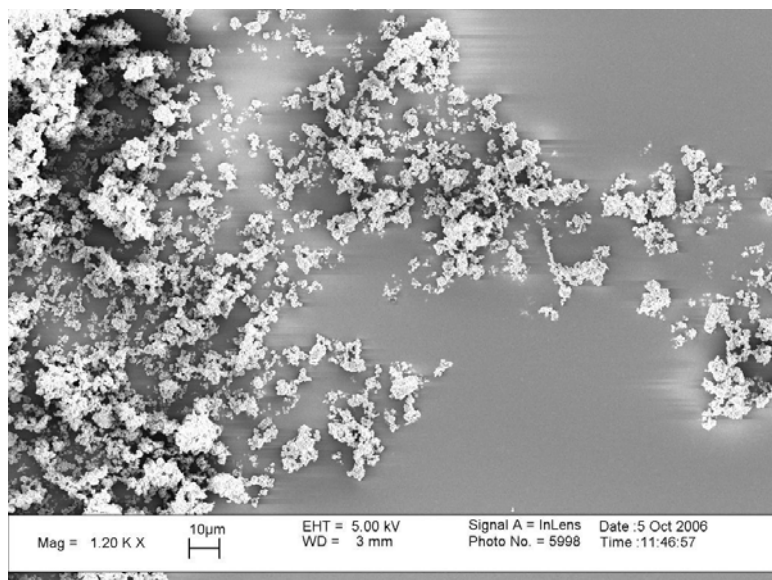
(a)
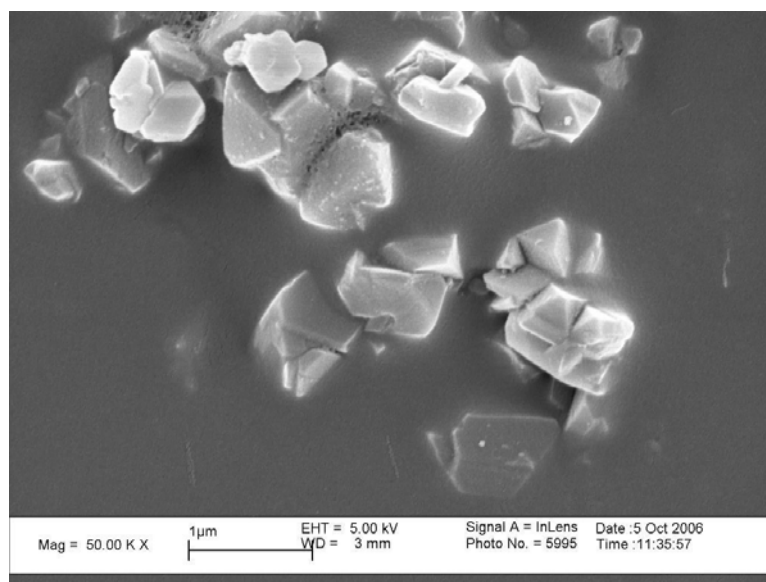
(b)

Figure 4.4: SEM images, (a) showing particle size distribution and (b) showing the

crystallites of USY zeolite.

Table 4.1: The chemical composition and basic physical properties of beta and USY

zeolites (Gong 2008)

Properties	Beta	USY
Si/ Al ratio (moles/moles)	13.3	2.90
Average crystal size (μm)	0.30	0.25
Average agglomerate size (μm)	0.50	0.50
Total surface area (m^2/ g)	605	665
Surface area with pores < 0.2 nm (m^2/ g)	542	610
Surface area with pores > 0.2 nm (m^2/ g)	64	55
Total pore volume (cc/ g)	0.286	0.312
Pore volume with pores < 0.2 nm (m^2/ g)	0.222	0.251
Pore volume with pores > 0.2 nm (m^2/ g)	0.064	0.061
Acidity (μmole NH_3/g catalyst)	291	466

For the single pulse TAP experiments the zeolites under investigation are calcined in situ in the micro-reactor at 698 K for 60 minutes. After calcination pretreatment, the zeolite is cooled to the desired temperature.

4.2.1 Probe Molecules Tested

As explained previously, alkylation reactions are catalyzed on the Brønsted acid sites. A majority of Brønsted acid sites are normally located inside the nano-porous zeolites structures. Consequently, the reactants from the bulk phase have to adsorb on zeolite surface then have to be transported to reactive Brønsted acid sites inside the pores. The

products formed have to diffuse away from the reactive center and be desorbed from the zeolite pore to facilitate the next reaction.

To decrease the rate of zeolite catalyst deactivation it is vital to increase the concentration of isobutane over n-butene near the vicinity of the Brønsted acid sites. In zeolites, achieving preferential adsorption and faster transportation of isobutane over n-butene to the Brønsted acid sites will lead to higher isobutane/ n-butene ratio near the Brønsted acid sites. Consequently, sorption and transport of isobutane and n-butene in zeolites has significant impact on the performance of zeolite catalyst alkylation processes.

In this study, isobutane one of the reactant of alkylation reactions was tested. Instead of n-butene, (the second reactant for the alkylation reactions) n-butane was tested. This was done since n-butene oligomerizes and irreversibly adsorbs in both the zeolites tested (as shown in reaction R1) at the temperature conditions we studied making it impossible to conduct single pulse TAP experiments. Further, n-butane and n-butene both have straight carbon chain and similar kinetic diameters (Qian and Yan, 2001). Future studies can be conducted using multi-pulse TAP experiments to study these reactions and quantify the rate constants (see Appendix A).

$$C_4H_8 + C_4H_8 + S \xrightarrow{k_1} C_8H_{16} + C_4H_8 + S \xrightarrow{k_2} C_{12}H_{24}S \xrightarrow{k_3} \ldots\ldots \qquad (R1)$$
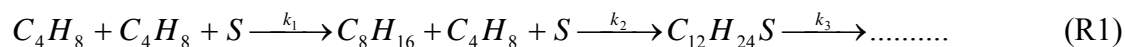
As mentioned earlier, the major products formed from the alkylation reactions are highly branched trimethylpentanes with high octane numbers. However, dimethylhexanes

having lower-octane blend values are also present in the product stream at varying levels. It will be interesting to understand how the different zeolite morphologies influence the intra-particle diffusivities and adsorption-desorption dynamics of these trimethyl-branched and dimethyl-branched C_8 isoalkanes. As a result, in this study 2,2,4-trimethylpentane with 100 RON (Research Octane Number) and 2,5-dimethylhexane with 70 RON were tested. These molecules further explore the shape selective nature of the beta and USY zeolites. To provide the information on transport in the inter-particle voids argon was tested. The chemical and the physical properties of these probe molecules are reported in the Table 4.2.

Table 4.2: Chemical and physical properties of probe molecules used in this work

Probe Molecules	Molecular formula/ Symbol	Kinetic Diameter[a,b], nm	Atomic Weight/ Molar Mass, g/ g-mole	Boiling Point, C
Argon	Ar	0.37	39.948	-185.85
Isobutane	i-C_4H_{10}	0.58	58.12	-11.7
n-Butane	n-C_4H_{10}	0.52	58.08	-0.5
2,2,4-trimethylpentane	2,2,4-C_8H_{18}	0.6547	114.2	99.3
2,5-dimethylhexane	2,5-C_8H_{18}	0.6511	114.23	108

[a] Gounaris et al., (2006); [b]Funke et al, (1996)

Here, the kinetic diameter can be understood as the diameter of a pore needed to let that specific molecule pass.

4.3 Method of Moments to Estimate Effective Knudsen Diffusivity D_{K_i}

The effective Knudsen diffusivity D_{K_i} in an inert zone can be determined by either fitting in the time domain the experimental TAP response curve with a model (equation 3.11 and 3.12 a,b, and c) generated one or by matching the moments of the predicted and measured responses. Both have been successfully employed in the past (Zou et al., 1993; Shekhtman et al., 2003)**.** Moreover there is ample evidence that the response curve obeys Knudsen diffusion in an inert zone (Gleaves et al., 1997; Keipert and Baerns, 1998; Nijhuis et al., 1999; Shekhtman et al., 2003). Recently, (Feres and Yablonsky, 2004) have presented a stochastic model that confirmed the findings of the previous continuum based models. The method of moments is used in this study to determine the effective Knudsen diffusivity in the inter-particle voids of the TAP micro-reactor. A single effective Knudsen diffusivity for each probe molecule is sufficient to describe the inter-particle transport provided the inter-particle space in the bed has a unimodal pore size distribution. This assumption is particularly true for the thin zone TAP reactor, as more than 99% of the packed micro-reactor volume is filled with non porous quartz particles with a mean diameter of 200 μm .

As shown earlier, (see Chapter 3, Section 3.5.1) the use of the thin zone micro-reactor configuration allows us to neglect the resistance of inter- and intra-particle diffusion in the zeolite zone for argon response curve. Consequently, argon response curves are used to estimate the effective Knudsen diffusivities of adsorbing species such as isobutane, n-

butane, 2,2,4-trimethylepentane and 2,5-dimethyhexane, by using the known temperature and molecular weight dependence $D_{K_i} \propto \sqrt{T/Mw_i}$ (see Chapter 3, Section 3.5.1 for more details). Equation 4.4 is used for estimating effective Knudsen diffusivity from the argon response curve. Equation 4.4 is a modified form of the equation 3.26 present in Chapter 3.

$$D_{K_i} = L^2 \varepsilon_b \frac{\int\limits_0^\infty E_{Ar}(t)\, dt}{\int\limits_0^\infty E_{Ar}(t) \times t\, dt} \qquad\qquad (4.4)$$

Here the $\int\limits_0^\infty E_{Ar}(t)\, dt$ is the zeroth moment (M_0) and $\int\limits_0^\infty E_{Ar}(t) \times t\, dt$ is the first moment (M_1) of the argon response curve. L is the length of the TAP micro-reactor (33 X 10^{-03} m) and ε_b is the bed porosity (~0.38). Table 4.3 reports the effective Knudsen diffusivities estimated from argon response curve in thin zone TAP reactor at different temperatures.

Table 4.3: Effective Knudsen diffusivity for argon at different temperatures

Temperature, K	Effective Knudsen Diffusivity, (10^{-3}) m^2/ sec
373	0.96
398	0.97
423	1.01
448	1.03
498	1.09
523	1.14
548	1.16
573	1.17
623	1.21
648	1.25
673	1.27

4.4 Minimization Method

The dimensionless constants, τ_{p_i} (the ratio of characteristic diffusion time in the micro-reactor to characteristic diffusion time in zeolite pore), K_{eq_i} (the ratio of characteristic desorption time to characteristic adsorption time), and $k_{d_i}^*$ (the ratio of characteristic diffusion time in the micro-reactor to characteristic desorption time) for adsorbing molecules (isobutane, n-butane, 2,2,4-trimethylpentane and 2,5-dimethylhexane) are estimated by fitting the dimensionless exit flux obtained from a single pulse TAP experiment with the numerically calculated dimensionless exit flux defined as

$F_i^* = \dfrac{\partial c_i(\tau,\xi)}{\partial \xi}\bigg|_{\xi=1}$. The experimental dimensionless exit flux is obtained by relating the

count intensity from the mass spectrometer to the molecular flow as explained in the

Chapter 3, Section 3.2.3. The numerically calculated model predicted dimensionless exit flux is obtained by solving the thin zone TAP reactor model (equations (3.11), (3.12, a, b, c), (3.19), (3.20), and (3.21 a, b). The numerical solution of the model equations is described in the Chapter 3, Section 3.4. Here the minimization method used to estimate the model parameters is described.

Figure 4.5 shows a flowchart of the minimization method used to estimate the model parameters τ_{p_i}, K_{eq_i}, and $k_{d_i}^*$. The heart of the minimization scheme is ODRPACK, a public domain software for minimizing the sum of the square weighted orthogonal distances from experimental data to a curve or surface. Using this method, the orthogonal distance between the experimental exit flux and modeled exit flux is minimized for every time step by changing the parameters. A detailed discussion about the algorithm, its stability, efficiency and advantage over the ordinary least squares method, especially in the case of nonlinear problems, can be found elsewhere (Boggs et al., 1987).

The following steps are taken during the minimization:
1. The minimization routine starts with an initial guess given by the user. A good initial guess is required for faster convergence of the solution.
2. Every time the routine needs to evaluate the sum of the squares of weighted orthogonal distances for given new estimates, the TAP model solver (PDE solver) is called and the model provides the newly computed solution for comparison.

3. The sum of the squares of weighted orthogonal distances is calculated by comparing the dimensionless exit flux of the model with the experimentally determined one.

4. When the convergence criteria have been reached, the routine outputs the parameters which give the smallest sum of the square of weighted orthogonal distances. The following three convergence criteria are used in this routine: (i) the sum of squares convergence, (ii) the parameter convergence and (ii) iteration limit is reached.
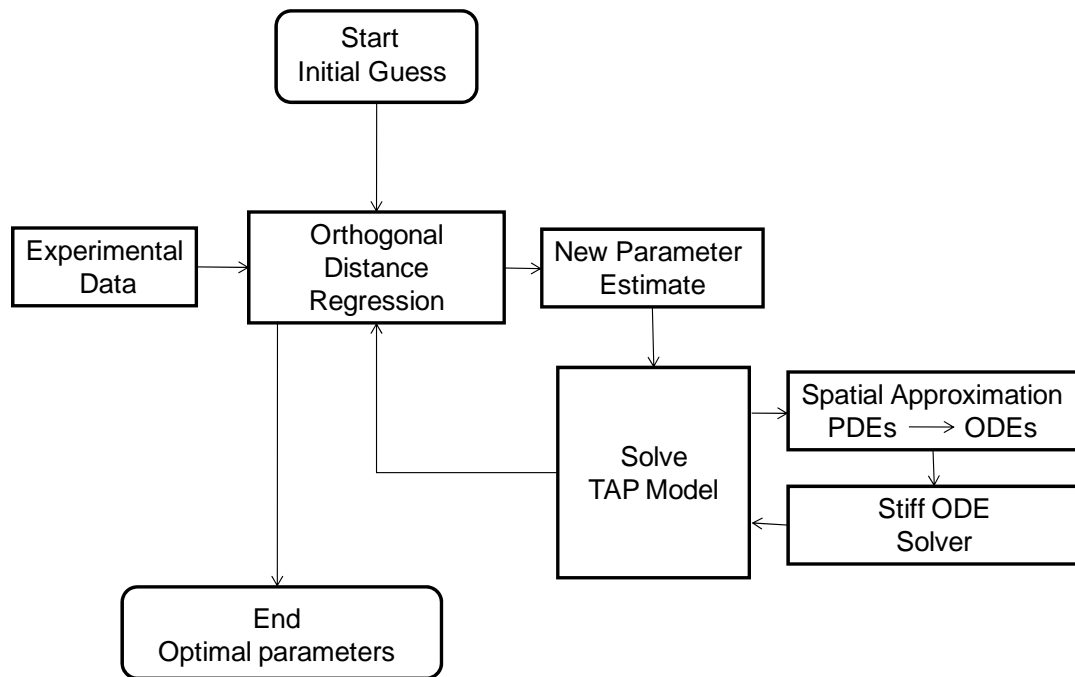
Figure 4.5: Flowchart of the minimization scheme

4.4.1 Covariance Matrix

To get the reliability and precision of the estimates the covariance matrix is used to construct the confidence region and intervals (Simon et al., 1997). The covariance matrix contains the covariance of the estimated parameters with each other. The primary diagonal therefore contains the variance (standard deviation) of the estimated parameters. From these values the confidence interval may be determined. The covariance matrix can be approximated as

$$V = \hat{\sigma}^2_{\beta_K} \left(J^T J \right)^{-1}.$$ (4.5)

Here, $\hat{\sigma}^2_{\beta_K}$ is the estimated residual variance, since the real value of $\sigma^2_{\beta_K}$ is usually not known, and J is the Jacobian matrix evaluated for the estimated values. The 95 % confidence intervals are computed using

$$\hat{\beta}_K \pm t_{.975,\mu} \hat{\sigma}_{\beta_K}.$$ (4.6)

Here, $\hat{\beta}_K$ is the estimated value and $t_{.975,\mu}$ is the appropriate value for the construction a two-sided 95 % confidence interval using the Student's t value for μ degrees of freedom (the degrees of freedom is the number of observations minus the number of parameters actually being estimated). In subsequent sections the estimated values of τ_{p_i}, K_{eq_i}, and $k^*_{d_i}$ are reported and discussed.

4.5 Results and Discussion

4.5.1 Comparison of Response Curves Obtained from Single Pulse TAP Experiments

In this section, single pulse TAP experiments with isobutane, n-butane, 2,2,4-trimethylpentane, and 2,5-dimethylhexane in beta and USY zeolites are discussed.. These experiments were carried out at various temperatures. A mass balance check was made for the conditions of each run to ensure that there was no reaction or irreversible adsorption of the probe molecules on the zeolite surface. This check consisted of comparing the number of molecules exiting the micro-reactor (zero[th] moment (M_0)) containing the thin zone of zeolite with the response of the same micro-reactor packed only with non-porous quartz, for the same input pulse intensity. Please note that the average value of M_0 is 0.01642 with standard deviation of 0.00044 for the argon response curve at pulse intensity 6.0 with 15.0 D.C voltage.

4.5.1.1 Beta Zeolite

Figure 4.6 a shows the dimensionless experimental response curves at 423 K for isobutane and n-butane obtained when pulsed over the micro-reactor packed with the thin

zone of beta zeolite. The shapes of the isobutane and n-butane response curve are similar, indicating that the differences in transport and adsorption-desorption phenomena for isobutane and n-butane in beta zeolite are negligible and that beta zeolite has a similar affinity for both branched and straight chain C_4 alkanes. This similarity was observed for all temperatures investigated in this study. However, for C_8 isoalkanes, it is observed that the magnitude of the peak for 2,2,4-trimethylpentane compared to 2,5-dimethylhexane is larger, and the elution time for 2,5-dimethylhexane response curve is much longer than the one for 2,2,4-trimethylpentane (see Figure 4.6 b). These differences in the two experimental response curves indicate that the 2,5-dimethylhexane was preferentially adsorbed and the intra-particle diffusion time of 2,5-dimethylhexane was slower in comparison to 2,2,4-trimethylpentane in beta zeolite. Similar behavior is also reported by Denayer et. al., (1998b) in zeolites such as beta, ZSM-5, mordenite and ZSM-22.

(a)

108

(b)
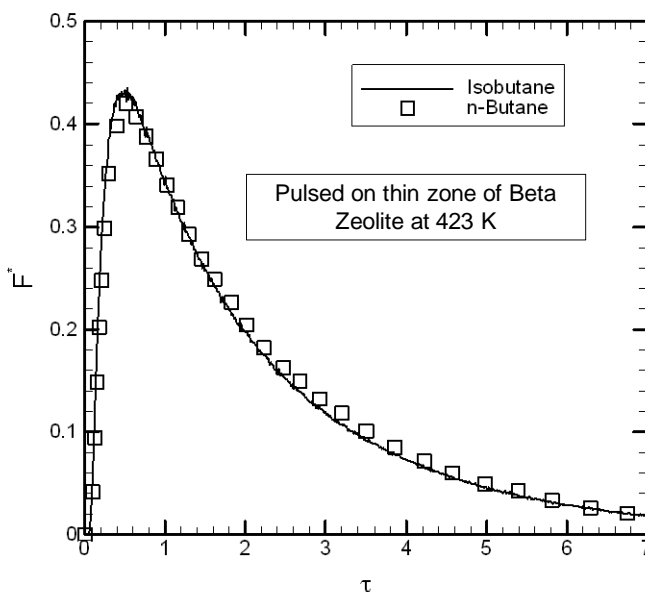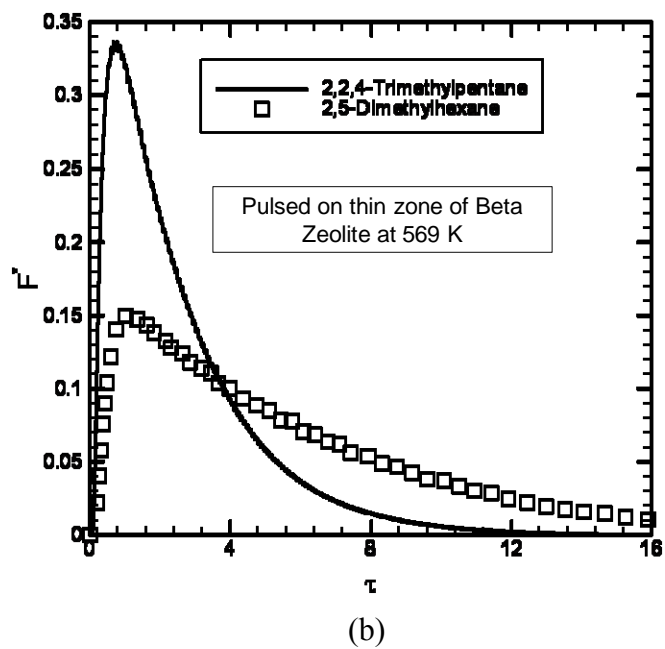
Figure 4.6: Dimensionless experimental response curves of adsorbing probe molecules

obtained when pulsed over thin zone of beta zeolite.

(a)

109
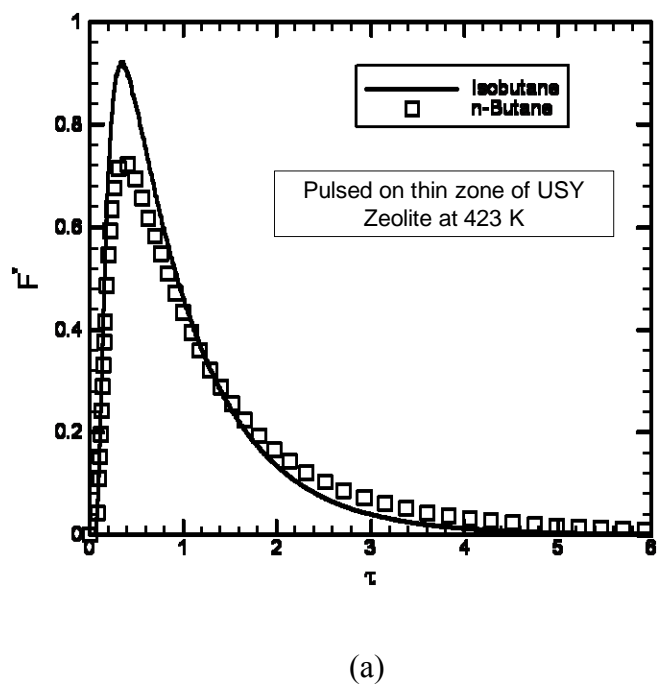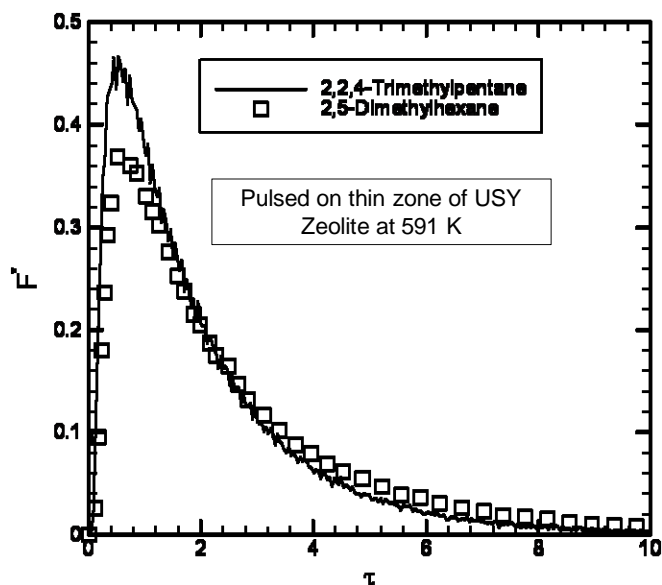
(b)

Figure 4.7: Dimensionless experimental response curves of adsorbing probe molecules

obtained when pulsed over thin zone of USY zeolite.

4.5.1.2 USY Zeolite

In the case of USY zeolite, the magnitude of the peak for isobutane TAP response curve

compared to the one for n-butane is larger, and the elution time for the n-butane response

curve is much longer than the one for isobutane (see Figure 4.7 a). This indicates that in

USY zeolite the retention capacity for n-butane is larger than for isobutane. This may be

due to isobutane being able to access less of the USY pore space than n-butane or due to

faster dynamics of iobutane adsorption-desorption and transport than for n-butane.

Hence, USY zeolite exhibits stronger affinity for adsorbing straight chain C_4 alkanes. For

110

C$_8$ isoalkanes, USY zeolite showed slightly stronger affinity towards dimethyl-branched isoalkanes in comparision to trimethyl-branched isoalkanes (see Figure 4.7 b).

At a given temperature for the probe molecules investigated, the USY response curve peak appears sooner than on the beta zeolite, and the curve exhibits a generally shorter elution time than the one for beta zeolite. These differences indicate that the characteristic nano-pore diffusion and characteristic desorption times are faster in USY zeolite than in beta zeolite and this may be caused by the larger pore diameter and smaller crystal size of USY zeolite. As an illustration, dimensionless experimental response curves of isobutane and n-butane pulsed over a thin zone of beta and USY zeolites at 423 K are shown in Figure 4.8.
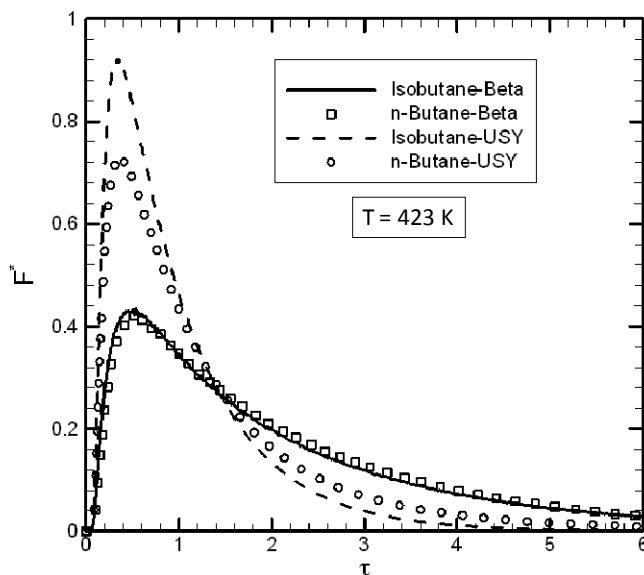
Figure 4.8: Dimensionless experimental response curves of isobutane and n-butane obtained when pulsed over thin zone of beta or USY zeolite at 423 K

111

4.5.2 Comparison of Experimental and Simulated TAP Response Curve

The simulated TAP response curves were fitted to the experimentally obtained ones by adjusting the three dimensionless model parameters τ_{p_i}, K_{eq_i}, and $k_{d_i}^*$.

4.5.2.1 Beta Zeolite

Figures 4.9 a, b, c and d compare the simulated and experimental dimensionless exit flux

$$\left(F_i^* = \frac{\partial c_i(\tau,\xi)}{\partial \xi}\bigg|_{\xi=1} \right)$$ of isobutane, n-butane, 2,2,4-trimethylpentane, and 2,5-

dimethylhexane as a function of dimensionless times (τ) at selected temperatures. It is observed that the experimental F_i^*, obtained from single pulse TAP experiments where beta zeolite (mass = 5 mg and mean diameter = 5 μm) was sandwiched between two inert zones (nonporous quartz, mass = 800 mg and mean diameter = 200 μm), is matched well with the developed model, which justifies the assumptions used in developing the thin zone TAP reactor model.
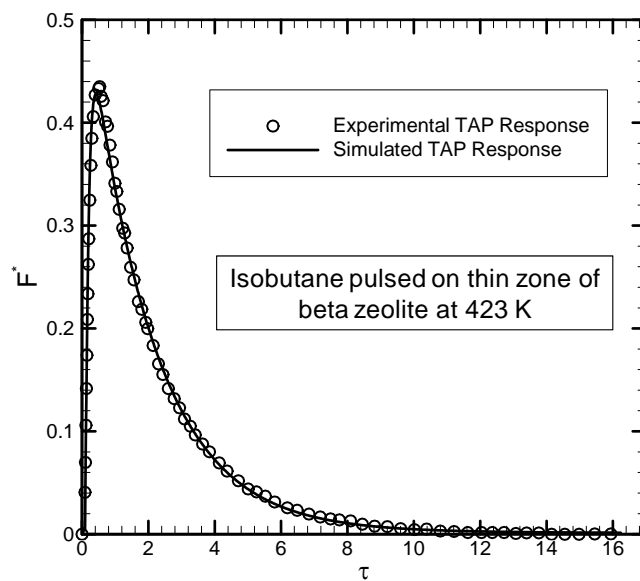
(a)
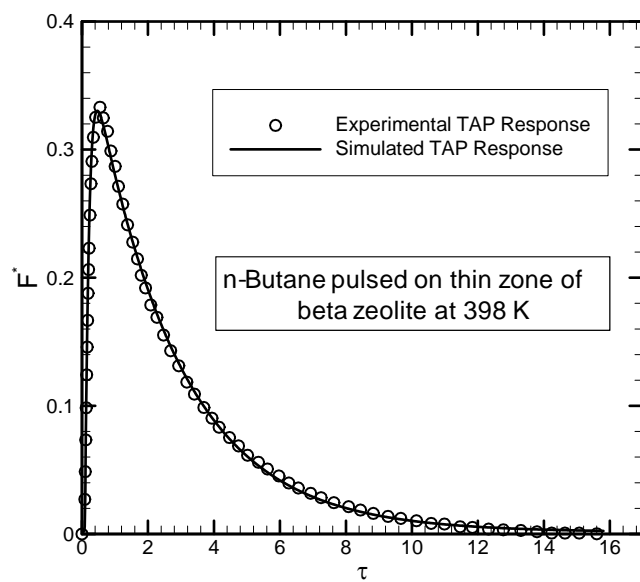
(b)
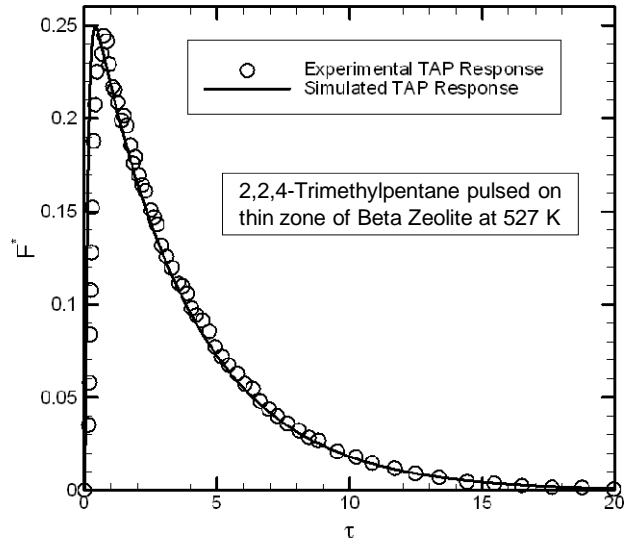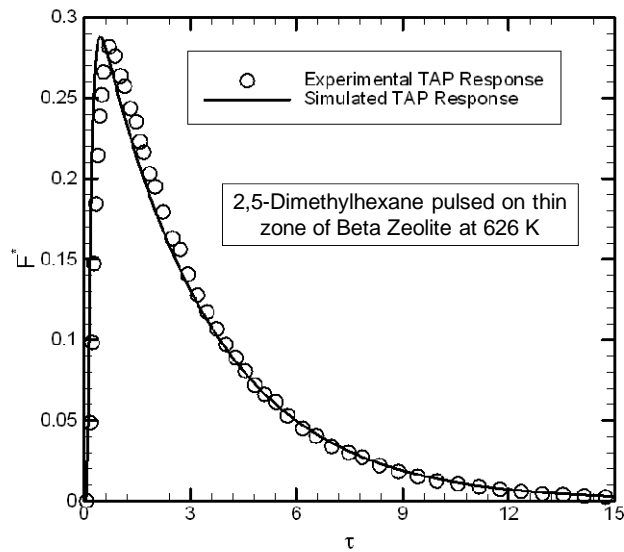
113

(c)

(d)

Figure 4.9: Simulated and experimental dimensionless exit flux as a function of

dimensionless times for adsorbing probe molecules pulsed over thin zone of beta zeolite

at selected temperatures.

4.5.2.2 USY Zeolite

Figures 4.10 a, b, c and d show the simulated and experimental dimensionless exit flux of isobutane, n-butane, 2,2,4-trimethypentane, and 2,5-dimethylhexane as a function of dimensionless time at selected temperatures. The experimental F_i^* was obtained from single pulse TAP experiments conducted over a thin zone of USY zeolite. Figures 4.10 c and d illustrate that the developed model predicts well the dimensionless exit flux. However, for the experimental responses of isobutane and n-butane in USY zeolite, the developed model underpredicts the dimensionless exit flux near the peak, but is in good agreement elsewhere. This is apparently caused by the faster intra-particle diffusion and shorter desorption times observed in USY zeolite for C_4 alkanes. This more rapid dynamics in USY zeolite particles the developed model is unable to capture as the estimated respective dimensionless constants falls outside the prescribed model sensitivity range.
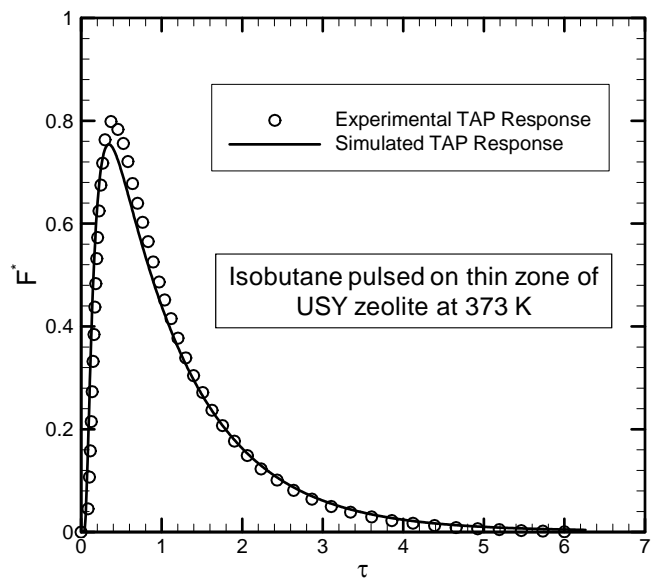
(a)
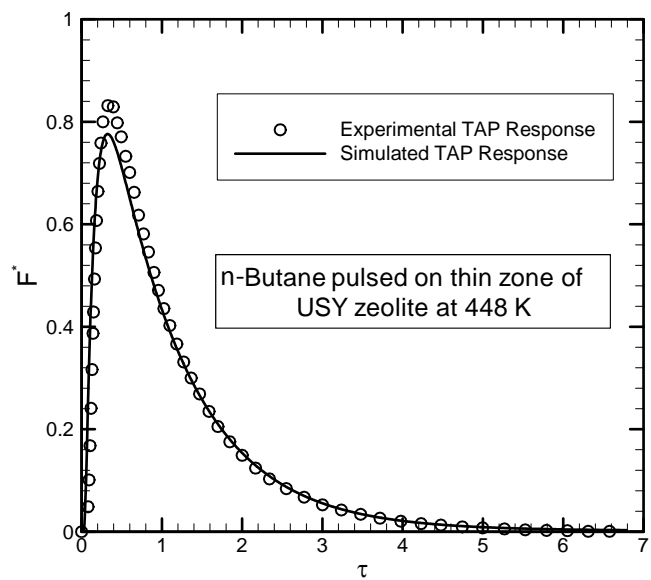
(b)
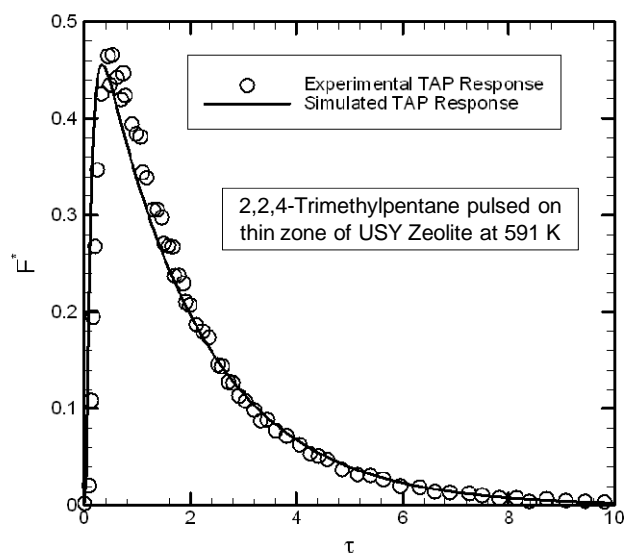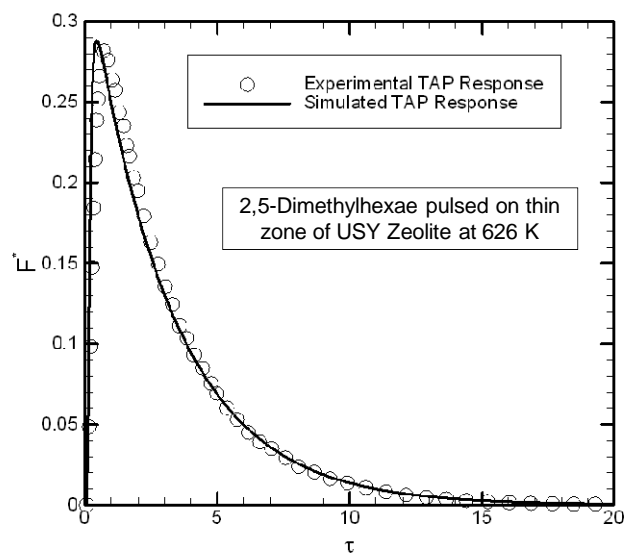
116

(c)

(d)

Figure 4.9: Simulated and experimental dimensionless exit flux as a function of dimensionless times for adsorbing probe molecules pulsed over thin zone of USY zeolite at selected temperatures.

117

4.5.3 Dimensionless Equilibrium Parameter $\left(K_{eq_i} \right)$

4.5.3.1 Beta Zeolite

Table 4.4 shows the values of the dimensionless equilibrium parameter $\left(K_{eq_i} \right)$, their standard deviation, and the 95% confidence interval, estimated by regressing the experimental TAP responses at different temperatures with the model simulated ones.

It is observed that the higher estimates of K_{eq_i} in beta zeolite were obtained for longer alkanes rather than shorter alkanes. Further, it is evident that on beta zeolite the estimated K_{eq_i} for branched paraffin (isobutane) was lower than for the straight chain one (butane), however the differences in the estimated K_{eq_i} values are minor. For example, the dimensionless K_{eq_i} value at 423 K for isobutane/ beta is 2480 and n-butane/ beta is 2638. Similar observations are also reported in the literature. For example, the estimation of the Langmuir adsorption constants of isobutane and n-butane in beta zeolite at 323 K by the TEOM (Tapered Element Oscillating Microbalance) method yielded 445 1/bar and 498 1/bar, respectively (Gong, 2008).

Table 4.4: The values of the dimensionless equilibrium parameter $\left(K_{eq_i}\right)$ for beta zeolite, with the standard deviation and 95% confidence interval, and apparent heats of adsorption $\left(\Delta H\right)$ obtained from the van't Hoff's plot with standard deviation

Probe Molecules	T, K	K_{eq} (x 10^3)	Std. Deviation (x 10^1)	95 % Confidence Interval (x 10^3)	$-\Delta H$, kJ/ mole
Isobutane	373	6.268	7.11	6.128 to 6.400	23.6
	398	4.288	1.75	4.288 to 4.288	(s.d. 2.32)
	423	2.480	0.78	2.460 to 2.498	
	448	1.416	1.64	1.384 to 1.448	
	473	1.318	3.00	1.259 to 1.377	
	498	1.031	2.68	0.962 to 1.060	
n-Butane	373	7000	7.44	6.790 to 7.230	24.5
	398	3.525	1.17	3.502 to 3.548	(s.d. 2.51)
	423	2.638	4.00	2.560 to 2.716	
	448	1.451	3.81	1.376 to 1.526	
	473	1.345	1.75	1.311 to 1.380	
	498	0.990	2.37	0.943 to 1.036	
2,2,4-TMP	518	18.40	23.9	17.93 to 18.87	50
	527	11.10	14.5	10.81 to 11.38	(s.d. 3.49)
	556	10.56	17.0	8.155 to 11.86	
	569	9.469	85.2	7.796 to 11.14	
	591	5.790	6.22	5.668 to 5.912	
	606	2.925	19.5	2.541 to 3.308	
	613	2.387	4.21	2.304 to 2.470	
	624	2.165	15.3	1.863 to 2.467	
	639	1.443	6.05	1.324 to 1.562	
2,5-DMH	542	55.93	426	47.57 to 64.29	55.44
	569	19.98	37.1	19.25 to 20.70	(s.d. 2.99)
	586	16.71	312	10.56 to 22.80	
	604	15.19	26.7	13.93 to 17.44	
	616	8.855	23.3	8.396 to 9.314	
	639	5.892	8.17	5.731 to 6.053	
	644	5.862	19.6	5.475 to 6.249	
	663	4.963	10.7	4.751 to 5.170	
	667	3.655	11.9	3.420 to 3.891	
	690	2.676	10.2	2.474 to 2.879	

Note: s.d. is the standard deviation of the apparent heat of adsorption; 2,2,4-TMP is 2,2,4-trimethylpentane; and 2,5-DMH is 2,5-dimethylhexane.

Assuming that the number of adsorption sites for 2,2,4-trimethypentane and 2,5-dimethylhexane are the same, for C_8 isoalkanes it was observed that the more the carbon skeleton is branched the lower the K_{eq_i} value:

$$K_{eq_i}(\text{2,5-dimethylhexane}) > K_{eq_i}(\text{2,2,4-trimethypentane}). \qquad (4.7)$$

The lower value of K_{eq_i} in beta zeolite for 2,2,4-trimethypentane indicates that the trimethyl-branched-alkanes were weakly adsorbed, lose fewer degrees of freedom on adsorption, and jumped more frequently from site to site, in comparison to dimethyl-branched-alkanes. This behavior of preferential adsorption of the dimethyl-branched-alkanes in beta zeolite has been observed previously (Denayer et al., 1998b).

In the straight and zig-zag channels of beta zeolite, the adsorption of probe molecules takes place inside the channels. As a result, smaller molecules such as isobutane and n-butane can easily access all the adsorption sites, hence beta is not so shape-selective for these molecules. However, when the molecular dimension is similar to the pore dimension, beta zeolite exhibits a peculiar shape selective nature as it adsorbs preferentially the slightly smaller 2,5-dimethylhexane (the average pore diameter of a straight channel is 0.69 nm and the kinetic diameters of 2,2,4-trimethylpentane and 2,5-dimethylhexane are 0.6547 nm and 0.6511 nm, respectively). Denayer et al., (1998a) reported similar behavior, as they found that the differences in their estimated Henry's constants for isoalkanes compared to n-alkanes increased as the carbon number increases. They investigated the $C_5 - C_8$ alkanes in beta zeolite using tracer and perturbation

chromatographic techniques. Consequently, the number of carbon atoms in alkanes influences the adsorption-desorption phenomena in beta zeolite.

4.5.3.2 USY Zeolite

Table 4.5 shows the values of the dimensionless equilibrium parameter $\left(K_{eq_i}\right)$, their standard deviation and the 95% confidence interval, estimated from thin zone TAP responses for adsorbing probe molecules in USY zeolites at different temperatures.

As reported for beta zeolite, the higher estimates of K_{eq_i} in USY zeolite were obtained for longer alkanes. Furthermore, lower estimates of K_{eq_i} were obtained for isobutane than for n-butane, indicating USY zeolite's stronger affinity for a straight chain paraffin, assuming that the maximum sites for adsorption of isobutane and n-butane are the same. For example, the dimensionless K_{eq_i} value at 423 K for isobutane/ USY zeolite is 802 and for n-butane/ USY zeolite is 1177. Similar behavior was also reported in the literature. For example, Gong, (2008) estimated the Langmuir adsorption constants for isobutane and n-butane in USY zeolites as 71 1/bar and 102 1/bar at 303 K, respectively, and Zhang et al., (2009) estimated the dimensionless Henry's constants for isobutane and n-butane at 303 K in USY zeolite as 2.1 and 3.8, respectively. For C_8 isoalkanes, the estimated K_{eq_i} for 2,2,4-trimethylpentane was generally lower than 2,5-dimethylhexane.

Table 4.5: The values of the dimensionless equilibrium parameter $\left(K_{eq_i}\right)$, with the standard deviation and 95% confidence interval, and apparent heats of adsorption $\left(\Delta H\right)$ obtained from the van't Hoff's plot for USY zeolite.

Probe Molecules	T, K	K_{eq} (x 10^3)	Std. Deviation (x 10^1)	95 % Confidence Interval (x 10^3)	$-\Delta H$, kJ/ mole
Isobutane	323	2.777	2.75	2.744 to 2.811	14.12
	348	1.482	1.71	1.431 to 1.533	(s.d. 1.85)
	373	1.047	2.61	0.951 to 1.100	
	398	0.919	2.58	0.869 to 0.970	
	423	0.802	2.69	0.758 to 0.847	
	448	0.742	1.78	0.707 to 0.776	
	483	0.733	1.94	0.695 to 7.716	
n-Butane	323	5.240	3.08	5.189 to 5.310	16.7
	348	3.689	1.58	3.658 to 3.720	(s.d. 0.80)
	373	2.239	0.80	2.223 to 2.253	
	398	1.476	0.90	1.459 to 1.494	
	423	1.177	0.60	1.165 to 1.189	
	448	0.941	1.60	0.910 to 0.973	
	483	0.788	1.56	0.757 to 0.819	
2,2,4-TMP	518	15.83	358	8.790 to 22.88	48
	543	9.464	17.2	7.255 to 12.04	(s.d 7.40)
	567	7.056	63.9	5.798 to 8.314	
	591	5.231	33.6	4.569 to 5.893	
	618	3.573	3.58	3.502 to 3.643	
	645	2.317	5.44	2.210 to 2.424	
	667	1.930	7.22	1.797 to 2.080	
2,5-DMH	470	33.08	144	30.24 to 35.92	46.1
	494	16.40	14.2	16.12 to 16.68	(s.d. 10.6)
	546	11.58	121	9.204 to 13.97	
	567	8.367	17.5	8.021 to 8.712	
	591	5.944	8.76	5.771 to 6.162	
	615	5.532	8.50	5.365 to 5.698	
	638	5.043	16.1	4.726 to 5.360	

Note: s.d. is the standard deviation of the apparent heat of adsorption; 2,2,4-TMP is 2,2,4-trimethylpentane; and 2,5-DMH is 2,5-dimethylhexane.

However the difference in the estimated K_{eq_i} values for 2,2,4-trimethylpentane and 2,5-dimethylhexane are minor in comparison to ones observed in beta zeolites.

The lower values of K_{eq_i} for isobutane compared to n-butane can be explained by understanding the physical and chemical properties of the USY zeolite. The average pore diameter (pore diameter 0.74 nm) of USY zeolite to access the super cage is much larger than the kinetic diameter of the isobutane and n-butane. Hence, these molecules can easily access the super cages. Furthermore, the absence of framework alumina in USY zeolite causes separation of the adsorption sites from one another (Denayer et al., 1998a). An isobutane molecule can more easily jump from one isolated adsorption site to another in the super cage as the molecular structure of isobutane is spherical and its kinetic diameter is much lower compared to super cage diameter. Hence, in USY zeolite ramified isobutane is weakly adsorbed in comparison to straight chain n-butane. However, when the carbon number increases the mobility of the alkanes with different molecular structure but same molecular weight becomes to some extent comparable in the super cages of USY zeolite (Denayer et al., 1998ab, Gilliland et al., 1974). This explains why in USY zeolite the differences in the estimates of K_{eq_i} for C$_8$ isoalkanes are minor than beta zeolite. Table 4.6 shows the estimated K_{eq_i} in beta and USY zeolites for 2,2,4-trimethylpentane and 2,5-dimethylhexane.

Table 4.6: The values of the K_{eq_i} in beta and USY zeolites.

Probe Molecules	Zeolite	T, K	K_{eq} (x 10^3)
2,2,4-trimethylpentane	beta	569	9.469
2,5-dimethylhexane	beta	569	19.98
2,2,4-trimethypentane	USY	591	5.231
2,5-dimethylhexane	USY	591	5.944

At this point it is instructive to discuss the differences between the equilibrium constants obtained by various techniques reported in the literature, and the K_{eq_i} values obtained by TAP. The former actually calculate the equilibrium constant by dividing the experimentally determined number of molecules of adsorbed species per unit mass of zeolite, normalized with the total number of sites that are available per unit mass of zeolite, with the equilibrium partial pressure of the adsorbing species (hence units of atm^{-1} or bar^{-1} as quoted earlier, appear in the literature). The important normalization factor of the total number of sites available for adsorption per unit mass of the zeolite is obtained at sufficiently high partial pressure of the adsorbing species when all sites are occupied and are in equilibrium with the fluid phase. Thus, the sites comprising the total possess different energies for adsorption. In contrast, in single pulse TAP experiments one does not have access to the total number of sites, and the K_{eq_i} values are obtained from dynamic experiments by computing the ratio of characteristic desorption and adsorption times. The needed normalization factor now represents the total sites available for adsorption at zero coverage and could change with temperature and experimental

124

conditions. Thus, quantitative comparison of TAP obtained equilibrium constant values and those obtained by other techniques cannot be made at present. Yet TAP values are well suited for comparison with molecular dynamics calculations. Moreover, the trends in the values should be comparable, as discussed earlier.

4.5.3.3 Temperature Dependency of the Equilibrium Parameter $\left(K_{eq_i}\right)$

The temperature dependency of the obtained dimensionless equilibrium constant $\left(K_{eq_i}\right)$ is represented by van't Hoff's equation. Figures 4.10 a and b display the van't Hoff plot for the equilibrium constant K_{eq_i} calculated for adsorbing probe molecules in beta and USY zeolites. The estimated apparent heat of adsorption with standard deviation for each adsorbing probe molecule in beta and USY zeolites are reported in Table 4.4 and Table 4.5, respectively. It is found that the apparent heat of adsorption estimated here is considerably lower than what is reported in the literature. For example, the heat of adsorption estimated by Gong, (2008) for isobutane/ USY zeolite is 35 ±4 kJ/mole, compared to 14.3 (s.d. 2.3) kJ/mole estimated in this study. Similarly, for butane/ USY zeolite the heat of adsorption was reported as 39 ±4 kJ/mole (Gong, 2008), compared to 16.3 (s.d.0.8) kJ/mole estimated in this study.

One possible reason for the discrepancy may be the influence of the carrier gas. Mittelmeijer-Hazeleger et al., (2002) reported that the type of carrier gas affects the rate

of adsorption and the shape of the adsorption isotherm in zeolites. They found that this is more pronounced at lower pressures and temperatures.

In this study the K_{eq_i} and ΔH were estimated by a transient method in the absence of carrier gas, in vacuum, and at conditions of very low coverage. One should recall that the equilibrium constant, defined as $K_{eq_i} = q_{\max_i} \dfrac{k_{a_i}}{k_{d_i}}$, is the product of the maximum sites available for adsorption of species i and the ratio of the adsorption and desorption rate constants for species i. In TAP experiments only the ratios of characteristic desorption and adsorption times are obtained but no independent information is available on $q_{\max_i}$ which logically speaking represents the maximum sites available at zero coverage. In other techniques, as mentioned above, the equilibrium constant values are obtained directly by the ratio of the adsorbed to bulk normalized concentrations. Thus, any changes in $q_{\max_i}$ with species, or from zeolite to zeolite, are reflected in the values of normalized adsorbed equilibrium concentrations. In the TAP case, one relies on the established fact that equilibrium properties like K_{eq_i} can be assesses by dynamic experiments as long as the system is linear. However, that assumes perfect measurement, as often the information is buried in the tail of the response curve, which is not readily measured.
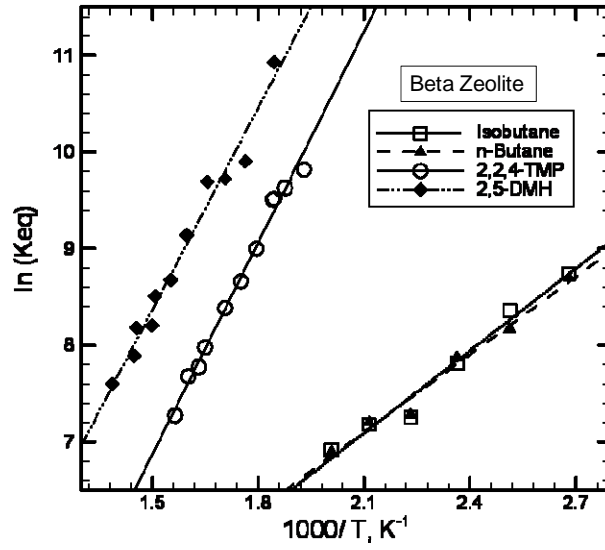
(a)
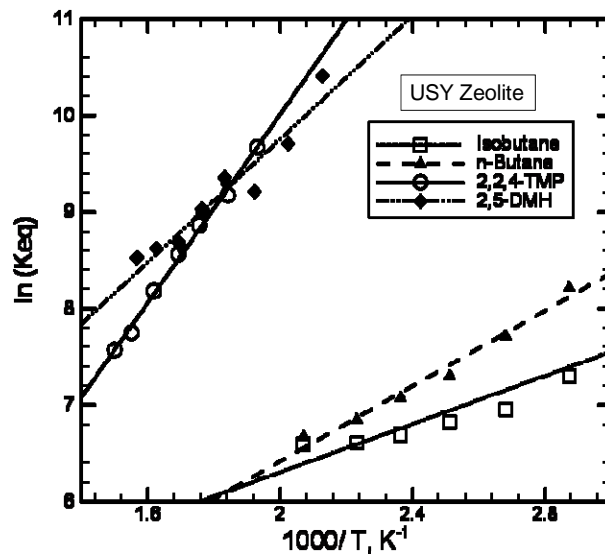
(b)

Figure 4.10: van't Hoff plot for equilibrium constant K_{eq_i} calculated for adsorbing probe

molecules in beta (Figure a) and USY (Figure b) zeolites. (2,2,4-TMP is 2,2,4-

trimethylpentane, and 2,5-DMH is 2,5-dimethylhexane)

In the TAP experiment we cannot capture the equilibrium values directly, but we can obtain the ratios of the characteristic times for adsorption and desorption and from them evaluate the equilibrium constant. The problem in obtaining accurate values lies in the fact that the accessible q_{max_i} varies with temperature, and this variation is reflected in the characteristic adsorption time. One would expect that as molecular mobility increases with temperature more active sites can be reached. Thus, the apparent q_{max_i}, which is sensed experimentally via TAP response through the adsorption-desorption time constants, becomes larger. While the ratio of the adsorption and desorption constants decreases with temperature, the rise in q_{max_i} with temperature reduces the apparent heat of adsorption.

It should be noted that while the absolute values of the heats of adsorption determined by TAP are much lower, the trends on the same zeolite for various species is the same as determined by other techniques. The difference between zeolites for the same species also tracks the trend established by equilibration techniques. For example, the apparent heat of adsorption values estimated in this study for isobutane in beta and USY zeolites are 23.6 (s.d. 2.32) kJ/ mole and 14.6 (s.d. 1.85) kJ/ mole, respectively. Gong (2008) reports values for isobutane in beta and USY zeolites 47 ±4 kJ/mole and 35 ±4 kJ/mole, respectively. This confirms that in transient techniques such as TAP there is not sufficient time for equilibration of gas and solid phase. As a result, the molecules do not reach all the adsorption sites of high energy (Condor and Young, 1979), hence further decreasing

the apparent heat of adsorption. This is why we call this quantity apparent heat of adsorption.

Further, as the temperature increases, the octahedral coordinated aluminum (Al) is converted to tetrahedral coordination (Zhang et al., 2000; Omegna et al., 2005), and the tetrahedral coordinated Al species are Brønsted sites (Zhang et al., 2000; Omegna et al., 2005). It has been reported that at low surface coverage the adsorption of alkanes occurs only on the Brønsted acid sites in zeolites (Denayer et al., 1998a). As a result, the maximum concentration of adsorption sites will increase with temperature, making more sites available during the TAP experiment. If one represented the increase in accessible sites with temperature with an Arrhenius type dependence, that would explain the reduction in the observed heat of adsorption while maintaining the van't Hoff's plot linearity

It is noteworthy that semi-quantitatively the apparent heats of adsorption for isobutane, n-butane, 2,2,5-trimethylpentane and 2,5-dimethylhexane in USY and beta zeolites obtained from TAP experiments match the trends reported in the literature. In beta zeolite, the apparent heat of adsorption for isobutane is slightly lower than for n-butane, (see Table 4.4). This is in agreement with the heat of adsorption values reported in the literature for alkanes in beta zeolite (Denayer et al., 1998b). In USY zeolite, the apparent heat of adsorption for n-butane is higher than for isobutane, which is in agreement with the values observed by other researchers such as Denayer et al., (1998b) and Gong,

(2008). The weak adsorption of isobutane in USY zeolite is likely due to its ramified skeleton, which allows easier motion of adsorbed molecules from site to site.

For C_8 isoalkanes, it was observed that the apparent heat of adsorption for 2,24-trimethylpentane was lower than 2,5-dimethylpentane in beta zeolite. Since, 2,5-dimethylpentane has more accessibility to adsorption sites in beta zeolite than 2,2,4-trimethylpentane due to the molecular structure and slightly smaller kinetic diameter. In USY zeolite, where both these molecules have equal accessibility to adsorption sites 2,2,4-trimethylpentane shows a slightly higher apparent heat of adsorption than 2,5-dimethylhexane.

The apparent heat of adsorption for the tested probe molecules was higher in beta zeolite than in USY zeolite (see Table 4.4 and 4.5). This is in comparison with the literature as shown above. As mentioned earlier, the beta zeolite framework consists of straight and zig-zag 12-member-ring channels of maximum free aperture 0.71 nm, compared to USY zeolite framework, which contains a super cage of free aperture 1.23 nm. As a result, the distance between the adsorbed molecules and beta zeolite framework is shorter than in USY zeolite, causing a stronger dispersive interaction and thus a higher heat of adsorption in beta zeolite.

4.5.4 Intra-particle Diffusion Time $\left(D_{e_i} / R_p^2\right)^{-1}$

4.5.4.1 Beta Zeolite

Table 4.7 reports the dimensionless parameter τ_{p_i} $\left(\tau_{p_i} = \dfrac{L^2 / D_{K_i}}{R_p^2 / D_{e_i}}\right)$ estimated for isobutane, n-butane, 2,2,4-trimethylpentane and 2,5-dimethylhexane pulsed over beta zeolite. The values reported in Table 4.7 falls inside the model sensitivity range. The characteristic time for intra-particle diffusion $\left(R_p^2 / D_{e_i}\right)$ was then estimated at each temperature by multiplying the τ_{p_i} obtained for the model match of experimental results by the characteristic diffusion time in the micro-reactor $\left(L^2 / D_{K_i}\right)$.

It is observed that the dimensionless parameter τ_{p_i} and characteristic intra-particle diffusivities time of n-butane and isobutane have the same order of magnitude. These similarities further indicate that the large pore beta zeolite (average pore diameter of straight channel ~ 0.69 nm) is not very shape selective for small molecules of similar diameter (the kinetic diameter of isobutane ~ 0.58 nm and of n-butane ~ 0.52 nm).

Table 4.7: The values of the dimensionless parameter τ_{p_i} (with the standard deviation and the 95% confidence interval), the intra-particle diffusivity $\left(D_{e_i}/R_p^2\right)$, and activation energies $\left(E_a\right)$ obtained from the Arrhenius plot, estimated over a thin zone of beta zeolites.

Probe Molecules	T, K	τ_{p_i} (x 10^{-5})	Std. Deviation (x 10^{-6})	95 % Confidence Interval (x 10^{-5})	$\left(D_{e_i}^0/R_p^2\right)$ (x 10^{-5}) sec^{-1}	E_a kJ/ mole
Isobutane	373	1.240	1.21	1.120 to 1.360	3.93	20.9
	398	1.850	0.65	1.780 to 1.920	5.98	(s.d. 2.78)
	423	1.810	0.78	1.730 to 1.890	5.88	
	448	2.330	4.05	1.930 to 2.740	7.92	
	473	3.900	4.89	3.500 to 4.310	13.8	
	498	4.710	4.70	4.310 to 5.120	17.0	
n-Butane	373	1.290	0.51	1.240 to 1.340	4.06	20.5
	398	1.500	0.59	1.440 to 1.560	4.74	(s.d. 3.08)
	423	1.700	2.88	1.410 to 1.990	5.61	
	448	2.340	4.67	1.870 to 2.810	7.99	
	473	3.920	4.70	3.450 to 4.390	14.3	
	498	4.270	4.08	3.800 to 4.700	16.0	
2,2,4-TMP	556	0.317	0.16	0.292 to 0.356	0.71	57
	606	0.537	0.20	0.347 to 0.654	1.25	(s.d. 10.4)
	624	0.914	0.27	0.841 to 1.025	2.16	
	634	1.690	0.95	0.967 to 2.239	4.03	
2,5-DMH	586	0.132	0.13	0.091 to 0.198	0.30	72
	592	0.138	0.11	0.935 to 0.237	0.53	(s.d 6.48)
	606	0.297	0.12	0.201 to 0.360	0.70	
	708	1.960	4.43	1.091 to 2.835	4.92	

Note: s.d. is the standard deviation of the activation energies; 2,2,4-TMP is 2,2,4-trimethylpentane; and 2,5-DMH is 2,5-dimethylhexane.

However, for larger C_8 isoalkanes both the dimensionless parameter τ_{p_i} and intra-particle diffusivities are much higher for trimethyl-branched-alkanes than dimethyl-branched-alkanes in beta zeolite:

132

$$\tau_{p_i}(2,2,4\text{-trimethypentane}) > \tau_{p_i}(2,5\text{-dimethylhexane}), \tag{4.8}$$

and

$$\left(D_{e_i}/R_p^2\right)(2,2,4\text{-trimethypentane}) > \left(D_{e_i}/R_p^2\right)(2,5\text{-dimethylhexane}). \tag{4.9}$$

The preferential adsorption of 2,5-dimethylhexane to that of 2,2,4-trimethylpentane in beta zeolite decreases its mobility from site to site, and this effect is manifested by a lower intra-particle diffusivity value. It is concluded that in beta zeolite, the molecular shape selective effects perturb the intra-particle transport behavior for C_8 isoalkanes.

In comparison to shorter alkanes, the longer alkanes showed lower intra-particle diffusivity values due bigger kinetic diameter, which restricts their motion in beta zeolite channels. Table 4.8 reports the intra-particle diffusivity values at 606 K in beta zeolite (particle size of $5\,\mu m$) for adsorbing molecules. Please note that the intra-particle diffusivity values reported in Table 4.8 for isobutane and n-butane were extrapolated to 606 K using Arrhenius equation. These intra-particle diffusivity values are in agreement with the range of the intra-particle diffusivities values reported in the literature for similar large pore zeolites with small particle size (Karger and Ruthven, 1992).

Table 4.8: The values of the D_{e_i} at 606 K in beta zeolite.

Probe Molecules	D_{e_i}, m^2/sec
Isobutane	2.07×10^{-15}
n-butane	2.07×10^{-15}
2,2,4-trimethypentane	7.81×10^{-17}
2,5-dimethylhexane	4.37×10^{-15}

133

4.5.4.2 USY Zeolite

Table 4.9 shows the values of the dimensionless parameter τ_{p_i}, their standard deviation and the 95% confidence interval, and intra-particle diffusivities estimated for 2,2,4-trimethylpentane and 2,5-dimethylhexane in USY zeolites at different temperatures. Unfortunately, the dimensionless constants τ_{p_i} at different temperature conditions for isobutane and n-butane estimated by the minimization procedure were found to be outside the model sensitivity range shown, in Table 3.1. This is apparently a result of the faster intra-particle diffusion for short alkanes in large pore USY zeolite, which can be corrected in the future experiments by tuning the experimental conditions as explained in Chapter 3, Section 3.5.3.

It was observed that the dimensionless parameter τ_{p_i} and characteristic intra-particle diffusivity time of 2,2,4-trimethylpentane and 2,5-dimethylhexae had the same order of magnitude. This resemblance further verifies that in the large pore USY zeolite with super cage C_8 isoalkanes have similar mobility from one isolated site to another. It was concluded that due to the non-shape selective nature of USY zeolite towards C_8 isoalkanes, the difference in estimated intra-particle diffusivity values is minor.

Table 4.9: The values of the dimensionless parameter τ_{p_i} (with the standard deviation and 95% confidence interval), the intra-particle diffusivity $\left(D_{e_i}/R_p^2\right)$ and activation energies $\left(E_a\right)$ obtained from the Arrhenius plot, estimated over a thin zone of USY zeolites.

Probe Molecules	T, K	τ_{p_i} (x 10^{-5})	Std. Deviation (x 10^{-6})	95 % Confidence Interval (x 10^{-5})	$\left(D_{e_i}^0/R_p^2\right)$ (x 10^{-6}) sec^{-1}	E_a kJ/ mole
2,2,4-TMP	518	0.278	0.16	0.183 to 0.339	6.04	26.65
	543	0.315	0.19	0.253 to 4.169	7.00	(s.d. 3.58)
	570	0.375	0.13	0.230 to 0.501	8.50	
	591	0.411	0.12	0.303 to 5.855	9.48	
2,5-DMH	470	0.201	0.16	0.119 to 0.257	4.47	24.5
	546	0.294	0.13	0.255 to 0.521	7.03	(s.d. 1.67)
	638	0.580	0.72	0.401 to 0.750	12.9	

Note: s.d. is the standard deviation of the activation energies; 2,2,4-TMP is 2,2,4-trimethylpentane; and 2,5-DMH is 2,5-dimethylhexane.

4.5.4.3 Temperature Dependency of Intra-particle Diffusivity

Figures 4.11 a and b show the Arrhenius plot for reciprocal values of intra-particle diffusion times in beta and USY zeolites. Tables 4.7 and 4.9 report the activation energies for the adsorbing probe molecules obtained from the Arrhenius plot in beta and USY. It was observed that the longer molecules have higher activation energy to diffuse in nano-pores of beta zeolite.
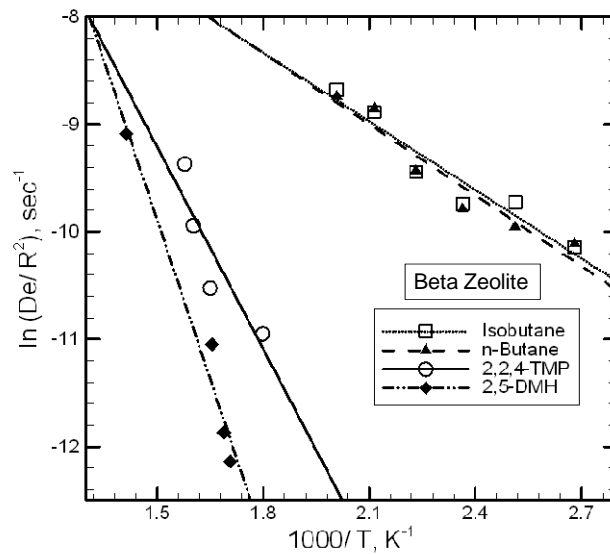
(a)
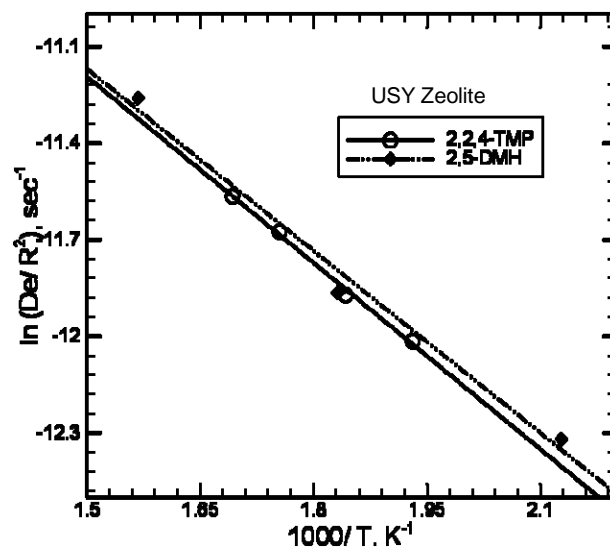
(b)

Figure 4.11: Arrhenius plot for reciprocal values of intra-particle diffusion times

calculated for adsorbing probe molecules in beta (Figure a) and USY (Figure b) zeolites.

(2,2,4-TMP is 2,2,4-trimethylpentane, and 2,5-DMH is 2,5-dimethylhexane

For example the activation energy for isobutane/ beta is 20.9 kJ/ mole compared to 57 kJ/ mole for 2,2,4-trimethylpentane/ beta. Furthermore, the activation energies of C_4 alkanes are similar, indicating the transport of these molecules in channels of beta zeolite has similar temperature dependencies. In contrast, the activation energy for 2,2,4-trimethylpentane is lower than for dimethylhexane, indicating lower a temperature dependency.

For USY zeolite it was observed that both 2,2,4-trimethylpentane and 2,5-dimethyhexane have similar temperature dependencies. Furthermore, when the activation energies for the same molecules are compared for different zeolites it was observed:

$$E_a \text{ (beta zeolite)} > E_a \text{ (USY zeolite).} \tag{4.9}$$

This observation indicates that the stronger dispersive interaction caused by the relatively shorter distance between the adsorbed molecules and beta zeolite framework results in increased activation energy.

4.5.5 Dimensionless Desorption Constant $\left(k_{d_i}^* \right)$

In this investigation the dimensionless desorption constant $\left(k_{d_i}^* \right)$ was estimated only for isobutane/ beta and n-butane/ beta at 378 K. For all the other temperature conditions, and for all the other probe molecules and zeolite combinations, the estimated value $\left(k_{d_i}^* \right)$ was

found to fall outside the model sensitivity range. The estimated $k_{d_i}^*$ values with their

standard deviations and confidence intervals are reported in Table 4.10.

Table 4.10: The values of the dimensionless desorption constant $\left(k_{d_i}^*\right)$, with the standard

deviation and 95% confidence interval estimated over a thin zone of beta zeolite.

Probe Molecules	T, K	$k_{d_i}^*$ (x 10^{-1})	Std. Deviation (x 10^{-2})	95 % Confidence Interval (x 10^{-1})
Isobutane	373	5.860	1.47	5.580 to 6.151
Butane	373	2.690	0.40	2.610 to 2.770

4.6 Rational Design of Solid Acid Catalyst for Alkylation Processes

Longer catalyst activity with time on stream (TOS) and higher 2,2,4-trimethylpentane

selectivity are the important assets required in an ideal solid catalyst for alkylation

processes (Gong et al., 2008). The understanding gained so far about the transport and

sorption in beta and USY zeolites is applied here to develop a rational design of an ideal

catalyst for alkylation reactions.

For longer catalyst activity with TOS, it is beneficial to maintain a higher isobutane to n-

butene ratio near the Brønsted acid sites (see Chapter 2, Section 2.6.3). We know that in

the zeolites the olefin adsorbs stronger than the paraffin (Rege et al., 1998). However,

until the theory is available to explain the difference, let us assume that the intra-particle

diffusion, adsorption-desorption dynamics and equilibria of n-butane is similar to n-

butene in the tested zeolites. Further, there are ample of evidence in the literature that the single-component adsorption-desorption dynamics and transport characteristic in nano-porous zeolite is not significantly perturb in the multi-component systems (Denayer et al., 1998b; Karger and Ruthven, 1992). Then we can postulate that the beta zeolite will non-selectively adsorb and transport both isobutane and n-butene in intra-particle space. In contrast, USY zeolite will more preferentially adsorb n-butene compared to isobutane. As a result, for a given feed isobutane to n-butene (P/ O) ratio, straight and zig-zag channels of beta zeolite have ability to maintain comparable P/ O ratio as bulk near the Brønsted acid sites, whereas super cages of USY zeolite will maintain lower ratio P/ O ratio than bulk near the Brønsted acid sites. Hence, if both beta and USY zeolite have equal concentrations of Brønsted acid sites, beta zeolite will yield longer catalyst activity with TOS. However, in reality beta zeolite has lower concentration of Brønsted acid sites than USY zeolite (see Table 4.1). This explains why the researchers in past have shown similar deactivation behavior for beta and USY zeolites (Corma et al, 1994 and Sarsani, 2007) for alkylation processes.

On the other hand, to achieve higher selectivity for 2,2,4-trimethylpentane, the super cages of USY zeolite will be more beneficial than the straight and zig-zag channels of beta zeolite, since we found, beta zeolite has a stronger affinity for the undesired 2,5-dimethylhexane than towards the desired 2,2,4-trimethylpentane. As a result, beta zeolite will have more tendency to form 2,5-dimethylhexane than USY zeolite. In USY zeolite the adsorption and transport characteristics of 2,2,4-trimethylpentane and 2,5-

dimethylhexane are similar. This explains why Sarsani, (2007) reported better selectivity to 2,2,4-trimethylpentane in USY zeolite than beta zeolite under otherwise identical experimental conditions. Further, based on the estimated the heats of adsorption and activation energies for diffusion it is recommended that the USY zeolite will require less energy for regeneration than beta zeolite.

Based on this finding, the ideal alkylation catalyst should be a hybrid of beta and USY zeolites. A hypothetical zeolite morphology for an ideal solid catalyst is proposed, containing the following physical and chemical properties:

1. Straight and zig-zag channels with an average pore diameter of 0.74 nm, for non-selective adsorption and transport of reactants and for lower heat of adsorptions and activation energies

2. Small cages in between these channels with an average pore diameter less than 1.2 nm but more than 0.74 nm, for higher formation of 2,2,4-trimethylpentane in these cages

3. Lower Si/ Al ratio, for higher Brønsted acid sites concentration.

Figure 4.12 shows the of pore morphology of the hypothetical solid acid catalyst for alkylation of isobutane and n-butene to form 2,2,4-trimethylpentane.
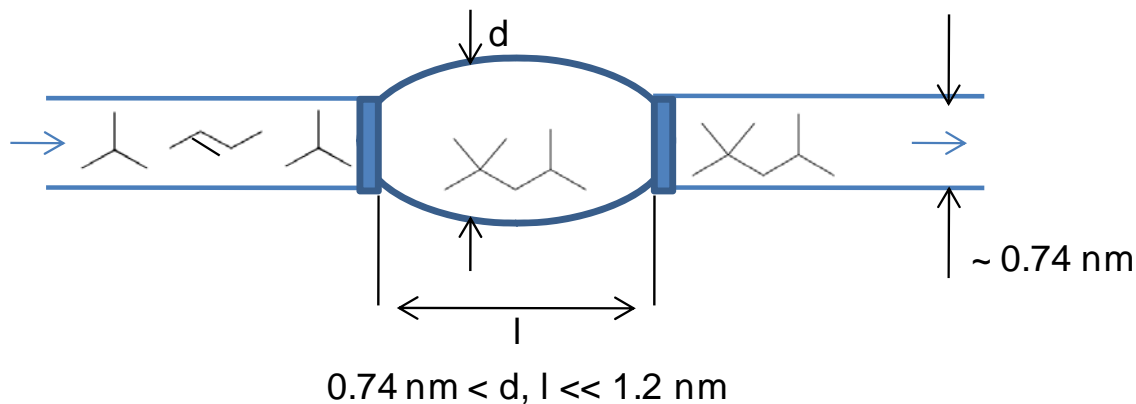
Figure 4.12: Pictorial depiction of pore morphology of an ideal solid acid catalyst for alkylation processes.

4.7 Conclusions

Thin zone TAP micro-reactor experiments were used to observe adsorption-desorption dynamics for n-butane, isobutane, 2,2,4-trimethylpentane, and 2,5-dimethylhexane and to evaluate their pertinent parameters in beta and USY zeolites. The apparent heat of adsorption and activation energy for diffusion in beta zeolite is higher than in USY zeolite, due to the shorter distance between adsorbed molecules in the beta zeolite framework. Based on the values of the equilibrium constants and the intra-particle diffusivities, it is concluded that branching of the C_4 alkanes has little effect in beta zeolites. However, for C_8 isoalkanes, beta zeolite shows preferential adsorption of the less branched carbon skeletons. Consequently, the number of carbons in alkanes influences the adsorption-desorption phenomena in beta zeolite. It was found that USY zeolite preferentially adsorbed n-butane over isobutane. However, for C_8 isoalkanes,

USY zeolite exhibited similar adsorption behavior. Consequently, USY zeolite shows affinity for alkanes with lower carbon numbers.

Based on the parameters estimated, which are outside the permissible model sensitivity range, it is concluded that the intra-particle diffusivity for isobutane and n-butane in USY and the desorption constant for all adsorbing molecules tested in this study cannot be reliably estimated form the TAP experiments conducted. A redesign of experimental conditions is required to bring the parameters into the acceptable sensitivity range. Specifically, to get reliable estimates of these parameters, the experiments should be carried out with larger inert particles or with a shorter micro-reactor length.

It is noted that while the trends in the apparent heats of adsorption obtained from the TAP experiments (e.g., variation from species to species on the same zeolite, or variation of a value for a given species from zeolite to zeolite) are in agreement with the values reported in the literature, the TAP-determined apparent heats of adsorption are considerably lower in absolute value. It was concluded that this most likely is due to the variation with temperature of the maximum active sites accessible to the probe molecules. Thus, without additional calibration for total sites available at zero coverage as a function of temperature, the TAP experiment cannot be expected to produce quantitative measures of the traditional heat of adsorption. However, if the experimental design is carefully chosen TAP offers opportunities for quantification of the dynamics of transport and adsorption–desorption in the particles.

Finally, based on the finding in this study the ideal alkylation catalyst should be a hybrid of beta and USY zeolites.

Nomenclature

c_i pulse-normalized bulk concentration

D_{e_i} effective diffusivity in the intra-particle space defined as $D_{e_i} = \dfrac{\varepsilon_p}{\varsigma_p} D_{T_i}$ m^2/ sec

D_{K_i} effective Knudsen diffusivity, m^2/ sec

D_{T_i} Fickian diffusivity, m^2/ sec

E_a activation energy, kJ/ moles

$E_i(t)$ time dependent intensity measured by the mass spectrometer, Mv/ sec

F_i^* dimensionless exit flow

ΔH apparent heat of adsorption, kJ/ moles

J Jacobian matrix

k_{a_i} adsorption constant, m^3/ moles-sec

k_{d_i} desorption constant, 1/ sec

$k_{d_i}^*$ dimensionless desorption constant

K_{eq_i} dimensionless equilibrium adsorption constant

L micro-reactor length, m

Mw_i molecular weight of species i, kg/ moles

M_j j^{th} moment

q_{max} maximum concentration of adsorption sites, moles/ m^3

R universal gas constant, kJ/ moles-K

R_p zeolite particle radius

T Temperature, K

t observation time, sec

V covariance matrix

Greek letters

β_K estimated parameter

τ dimensionless time

τ_{p_i} $\dfrac{L^2 / D_{K_i}}{R_p^2 / D_{e_i}}$

μ degree of freedom

ξ dimensionless spatial distance within the micro-reactor

η dimensionless spatial distance within the zeolite particle

ε_b solid holdup

$\hat{\sigma}_{\beta_K}^2$ estimated residual variance

References

Baerlocher Ch., W. M. Meier, and D. H. Olson (2001). "Atlas of Zeolite Framework Types". 5th ed., Elsevier: Amsterdam.

Boggs, P. T., R. H. Byrd and R. B. Schnabel (1987). "A stable and efficient algorithm for nonlinear orthogonal distance regression." SIAM Journal on Scientific and Statistical Computing 8(6): 1052-1078.

Condor, J. L. and C. L. Young (1979). Physicochemical measurements by gas-adsorption chromography. Chicester, U.K, John Wiley and Sons.

Corma A., A. Martinez and C. Martinez (1994)." Isobutane / 2-butene alkylation on MCM-22 catalyst. Influence of zeolite structure and acidity on activity and selectivity". Cat. Lett. 28: 187-201

Denayer, J. F., G. V. Baron, J. A. Martens and P. A. Jacobs (1998a). "Chromatographic study of adsorption of n-alkanes on zeolites at high temperatures." Journal of Physical Chemistry B 102(17): 3077-3081.

Denayer, J. F., W. Souverijns, P. A. Jacobs, J. A. Martens and G. V. Baron (1998b). "High-temperature low-pressure adsorption of branched c5−c8 alkanes on zeolite beta, zsm-5, zsm-22, zeolite y, and mordenite." Journal of Physical Chemistry B 102(23): 4588-4597.

de Jong K. P, C.M.A.M.Mesters, D.G.R. Peferoen, P.T.M. van Brugge, C. de Groot, (1996). "Paraffin alkylation using zeolitie catalysts in a slurry reactor: Chemical engineering principles to extend catalyst lifetime". Chem. Eng. Sci. 51(1996) 2053.

Feres, R. and G. Yablonsky (2004). "Knudsen's cosine law and random billiards." Chemical Engineering Science 59(7): 1541-1556.

Funke H H., A. M. Argo, C. D. Beartsch., J. L Falconer, R. D. Noble, (1996). " Separation of close-boiling hydrocarbons with silicalite zeolite". J. Chem. Soc., Faraday Trans., 92(13) 2499

Gleaves, J. T., G. S. Yablonskii, P. Phanawadee and Y. Schuurman (1997). "Tap-2: An interrogative kinetics approach." Applied Catalysis, A: General 160(1): 55-88.

Gong, K. (2008). Adsorption/desorption studies on solid acid alkylation catalysts using a tapered element oscillating microbalance (teom), University of Kansas. Ph.D.

Gong, K., S. Chafin, K. Pennybaker, D. Fahey, and B. Subramaniam, (2008). "Economic and environmental impact analyses of solid acid catalyzed isoparaffin/olefin alkylation in supercritical carbon dioxide". Industrial & Engineering Chemistry Research (in press).

Gounaris G. E., C. A. Floudas, J. Wei (2006). "Rational design of shape selective separation and catalysis-I Concept and analysis". Chem Engg Sci., 61 7933

Kazansky V. B., M. V. Frash., R. A. van Santen (1996). "Quantumchemical study of the isobutane cracking on zeolites". Appl. Catal. A 146

Karger, J. and D. M. Ruthven (1992). Diffusion in zeolites and other microporous solids. New York, John Wiley and Sons.

Karger J., F., Grinbery, P., Heitjons P (2005). Diffusion Fundamental. Leipzig.

Keipert, O. P. and M. Baerns (1998). "Determination of the intracrystalline diffusion coefficients of alkanes in h-zsm-5 zeolite by a transient technique using the temporal-analysis-of-products (tap) reactor." Chemical Engineering Science 53(20): 3623-3634.

Krishna R., J. A. Wesselingh (1997). "The Maxwell-Stefan approach to mass transfer". Chem. Engg. Sci. Vol -52, 6, 861-911

Martinis and G. F. Forment, (2006). "Alkylation on solid acids. Part 1. Experimental investigation of catalyst deactivation". Ind. Eng. Chem. Res 45, 940-953.

Martinis and G. F. Forment, (2006). "Alkylation on solid acids. Part 2. Single-event kinetic modeling" Ind. Eng. Chem. Res 45, 954-967.
Mittelmeijer-Hazeleger, M. C., A. F. P. Ferreira and A. Bliek (2002). "Influence of helium and argon on the adsorption of alkanes in zeolites." Langmuir 18(25): 9613-9616.

Mittelmeijer-Hazeleger, M. C., A. F. P. Ferreira and A. Bliek (2002). "Influence of helium and argon on the adsorption of alkanes in zeolites." Langmuir 18(25): 9613-9616.

Nijhuis, T. A., L. J. P. van den Broeke, M. J. G. Linders, J. M. van de Graaf, F. Kapteijn, M. Makkee and J. A. Moulijn (1999). "Measurement and modeling of the transient adsorption, desorption and diffusion processes in microporous materials." Chemical Engineering Science 54(20): 4423-4436.

Omegna, A., R. Prins and J. A. van Bokhoven (2005). "Effect of temperature on aluminum coordination in zeolites h−y and h−usy and amorphous silica−alumina: An in situ al k edge xanes study." The Journal of Physical Chemistry B 109(19): 9280-9283.

Qian L and Z. -F. Yan (2001)." Micropore modification of zeolites with transition-metal oxides". Colloids and Surfaces A 180(3): 311-316

Ruthven, D. M (1984). Principles of Adsorption and Adsorption Processes. Wiley New Yorl USA.

Rege S. U, J. Padin, R. T. Yang (1998). "Olefin/paraffin separations by adsorption: π-Complexation vs. kinetic separation". AIChE 44(4): 799-809.

Sarsani, V.S.R., (2007). Solid acid catalysis in liquid, gas-expanded liquid and near critical reaction media: Investigation of isobutane/ butene alkylation and aromatic acylation reactions. Ph D. Dissertation, University of Kansas.

Shekhtman, S. O., G. S. Yablonsky, J. T. Gleaves and R. Fushimi (2003). ""State defining" Experiment in chemical kinetics--primary characterization of catalyst activity in a tap experiment." Chemical Engineering Science 58(21): 4843-4859.

Simon C, van der Linde, T. A. Nijhuis, F. H. M. Dekker, F. Kapteijn and J. A. Moulin (1997). "Mathematical treatment of transient kinetic data: Combination of parameter estimation with solving related partial differential equations". App. Cat. A 151: 22-27.

Simpson M. F., J. Wei, S. Sundaresan (1996). "Kinetic analysis of isobutane/butene alkylation over ultrastable H-Y zeolite", Ind. Eng. Chem. Res. 35, 3861-3873.

Van Den Broeke L. J. P., and R. Krishna (1995). "Experimental Verification of the Maxwell-Stefan Theory for Microscopic Diffusion". Chem. Engg. Sci. Vol 50, 16 , 2507-2522

Zhang, J., Z. Zhao, A. Duan, G. Jiang, J. Liu and D. Zhang (2009). "Chromatographic study on the adsorption and diffusion of light hydrocarbons in zsm-5 and usy zeolites." Energy & Fuels 23(2): 617-623.

Zhang, W., P. G. Smirniotis, M. Gangoda and R. N. Bose (2000). "Bronsted and lewis acid sites in dealuminated zsm-12 and β zeolites characterized by nh3-stpd, ft-ir, and mas nmr spectroscopy." The Journal of Physical Chemistry B 104(17): 4122-4129.

Zou, B., M. P. Dudukovic and P. L. Mills (1993). "Modeling of evacuated pulse micro-reactors." Chemical Engineering Science 48(13): 2345-2355.

CHAPTER 5

Conclusions and Recommendations

The successful commercialization of environmentally friendly processes requires not only a green catalyst but also an improved understanding at the molecular as well as reactor level. An example of such multi-scale research approach is reported in this study for zeolite catalyzed alkylation processes. Based on experimental and theoretical methods, we have shown that alkylate yield and catalyst activity can be significantly improved by better reactor flow configuration, optimal catalyst particle design and improved pore morphology.

Based on the theoretical modeling efforts for understanding the key kinetic steps of zeolite catalyzed alkylation reactions we concluded that:

1. The hydride transfer and oligomerization reaction are the key kinetic steps affecting the overall performance of zeolite catalyzed alkylation processes. It is desirable to have a high rate of hydride transfer, as it augments the production of alkylates and prolongs zeolite catalyst life by desorbing saturated hydrocarbon from the Brønsted acid sites. On the other hand, oligomerization reduces the production of alkylates and shortens zeolite catalyst life by producing unsaturated hydrocarbons which are irreversibly adsorbed on the Brønsted acid sites.

2. Adding efficient hydride donors such as adamantine and making the hydride transfer step less sterically hindered by extending the acid site away from the support should considerably improve alkylate yield and decrease the zeolite catalyst deactivation rate. Since, it was observed that as the values of ϕ_4^2 / ϕ_2^2 decreased from 4 to 0.25 (i.e. kinetic constant for hydride transfer was increased),

149

the maximum alkylate yield with TOS was improved from 40 % to 70 % and the time required for complete zeolite deactivation was increased from 6 hr to 10 hr.

3. High isobutane concentration near the Brønsted acid site increases the production of alkylate yield by increasing the probability of hydride transfer between isooctenes and isobutane. In addition, the undesired oligomerization between isooctenes and olefins are suppressed, hence the zeolite catalyst life is longer. By attaining reactor scale flow pattern close to plug flow for isobutane and high back-mixing for n-butene, will result in high local P/ O ratio. The high local ratio of P/ O can be also achieved by a high feed P/ O ratio. However with an increase in feed P/ O ratio, the cost associated with separation and recycling the unreacted isobutane also increases, and this needs to be addressed separately.

4. The egg shell type of Brønsted acid site distribution performed much better than the egg white and egg yolk distributions. Since the maximum alkylate yield with TOS for egg shell distribution was 50 % compared to 40 % for egg white and 15 % for egg yolk distribution. In the egg shell type of distribution the thin shell of Brønsted acid sites is placed just a small distance away from the external surface of the zeolite. Thus, n-butene diffuses through a finite intra-particle space to reach the Brønsted acid sites. As a result, the P/ O ratio in the intra-particle space is higher than in the bulk. Furthermore, alkylates formed in this thin shell can easily diffuse out to the bulk. The above stated phenomena cause an increase in the alkylate yield and longer zeolite catalyst life in the egg shell. Hence, employ egg shell type of Brønsted acid site distribution in zeolite particle.

5. The decrease in Si/ Al ratio increases the initial Brønsted acid site concentration. As a result, the alkylate yield and zeolite catalyst life increase. Hence, have lower Si/ Al ratio in the zeolite catalyst particle.

To further enhance the science of alkylation processes, single pulse TAP experiments were employed to study sorption and transport in nano-porous zeolites. Although, these experiments are conducted under ultra high vacuum conditions which do not mimic the true industrial systems, they still offer the following advantages:

1. They provide the direct estimate of transport and sorption processes at extremely low surface coverage $(\theta_i \rightarrow 0)$. Consequently, the intra-particle diffusivity and adsorption-desorption constants estimated from the single pulse TAP experiments can be considered independent of surface coverage.

2. The experiments are conducted in the absence of an inert carrier stream, with no external mass transfer resistance, and with a negligible thermal effect. Hence, further increasing the reliability of estimated parameters.

3. The use of a thin zone TAP reactor configuration enables the use of small, commercially available zeolite particles without causing high bed resistance. Hence, decreasing the signal to noise ratio.

A theoretical model that considers transport and adsorption–desorption phenomena in the inter-particle and intra-particle space of thin zone TAP reactor was developed and numerically solved. Key assumptions of the developed model were:

1. That the molecular transport at the zeolite particle boundary can be characterized by a local adsorption rate constant, k_{a_i}, and a local desorption rate constant, k_{d_i} instead of assuming rapid local equilibrium (Keipert and Baerns, 1998). This assumption is based on the fact that the molecules in the vapor or adsorbed on the external surface have to overcome an surface barrier to become adsorbed and transported within the internal pore space (Chandross et al., 2001; VignUe-Maeder et al., 1992).

2. That all molecules in the intra-particle space of zeolites were adsorbed on the wall of the zeolite. These assumptions were formulated based on considerations of the physical dimensions of the zeolite structure (the zeolite pores have molecular dimensions).

Based on these assumptions the developed model had three dimensionless parameters τ_{p_i}, (the ratio of characteristic diffusion time in the micro-reactor to characteristic diffusion time in zeolite pore), K_{eq_i} (the ratio of characteristic desorption time to characteristic adsorption time), and $k_{d_i}^*$ (the ratio of characteristic diffusion time in the micro-reactor to characteristic desorption time), that affected the shape, peak position and height of the model simulated response curve. It was established that various system parameters can only be reliably estimated form a single pulse TAP experiment in a thin zone micro-reactor when the three dimensionless constants of the model fall into certain ranges. Since these constants are not known 'a priori', reliable estimation of system

parameters may involve an iterative procedure of experimental design and data interpretation to establish the range of constants needed for reliable estimates.

Large pore beta zeolite with Si/ Al ratio of 13 and USY zeolite with Si/ Al ratio of 3 were chosen in this study as they have in the past shown high product selectivity and longer catalyst activity for alkylation processes (de Jong et al., 1996; Sarsani 2007; Simpson et al., 1996). The beta zeolite has straight (pore diameter is 0.66 x 0.71 nm) and zig-zag (pore diameter is 0.56 x 0.56 nm) channels. In contrast USY zeolite has super cages (super cages size 1.24 nm) with window opening of 0.74 nm. The distance between the adsorbed molecules and the beta zeolite framework is shorter than in USY zeolite. Consequently, it was found that both the apparent heat of adsorption and diffusion activation energy were higher in beta zeolite for a given molecule. For example, the apparent heat of adsorption values for isobutane in beta and USY zeolites are 23.6 (s.d. 2.32) kJ/ mole and 14.6 (s.d. 1.85) kJ/ mole, respectively, and the activation energy values for 2,2,4-trimethylpentane in beta and USY zeolites are 57 (s.d. 10.4) kJ/ mole and 26.65 (s.d. 3.58) kJ/ mole, respectively. It was concluded that the USY zeolite will require less energy for regeneration than beta zeolite.

Furthermore, two different adsorption-desorption dynamics were observed in these zeolites for molecules of similar molecular weight:

1. Straight and zig-zag channels of beta zeolite exhibit similar affinity for adsorbing branched and straight C_4 alkanes and, stronger affinity for adsorbing dimethyl-

branched over trimethyl-branched C_8 isoalkanes. Consequently, the number of carbon atoms in alkanes influences the adsorption-desorption phenomena in beta zeolite.

2. Super cages of USY zeolite exhibit stronger affinity for adsorbing straight chain C_4 alkanes and similar affinity for adsorbing dimethyl-branched and trimethyl-branched C_8 isoalkanes. Consequently, the USY zeolite shows affinity for alkanes with lower carbon numbers.

Based on our findings on transport and sorption in nano-porous zeolites, to achieve higher 2,2,4-trimethylpentane selectivity and longer catalytic activity it is recommended that the ideal zeolite morphology should feature characteristics of both beta and USY zeolites. Specifically, it should have straight and zig-zag channels for maintaining high P/O ratio near the Brønsted acid site. Further the average pore diameter of these channels should be 0.74 nm, for achieving lower heat of adsorption and activation energy for diffusion. For higher formation of 2,2,4-trimethylpentane it should have small cages in between these channels, with average pore diameter less than 1.2 nm but more than 0.74 nm.

This study exemplifies the need for multi-scale research efforts for efficient process development. This approach, in which fundamental understanding of catalysis, reaction engineering, and material science is applied, should be able to achieve elegant solutions and greener processes. Research efforts should be focused beyond the one-scale.

References:

de Jong K. P, C.M.A.M.Mesters, D.G.R. Peferoen, P.T.M. van Brugge, C. de Groot, (1996). "Paraffin alkylation using zeolitie catalysts in a slurry reactor: Chemical engineering principles to extend catalyst lifetime". Chem. Eng. Sci. 51(1996) 2053.

Chandross, M., E. B. Webb III, G. S. Grest, M. G. Martin, A.P. Thompson, and M. W. Roth, (2001). "Dynamics of exchange at gas-zeolite interfaces. I. Pure component n-butane and isobutene". Journal of Physical Chemistry B 105: 5700–5712.

Keipert, O. P. and M. Baerns (1998). "Determination of the intra-crystalline diffusion coefficients of alkanes in h-zsm-5 zeolite by a transient technique using the temporal-analysis-of-products (tap) reactor." Chem. Eng. Sci. 53(20): 3623-3634.

Sarsani, V.S.R., (2007). Solid acid catalysis in liquid, gas-expanded liquid and near critical reaction media: Investigation of isobutane/ butene alkylation and aromatic acylation reactions. Ph D. Dissertation, University of Kansas.

Simpson M. F., J. Wei, S. Sundaresan (1996). "Kinetic analysis of isobutane/butene alkylation over ultrastable H-Y zeolite", Ind. Eng. Chem. Res. 35, 3861-3873.

VignUe-Maeder, F., S. El Amrani, P. Guelin, (1992). "An approach to the surface barrier concept in diffusion in zeolites by computer simulation". J. Cat. 134: 536–541.

Single Pulse TAP Experiments

Aim: To estimate diffusivities and adsorption/ desorption constants of probe molecules on beta and USY zeolites particles (diameter $\sim 5 \ \mu m$) at zero surface coverage, using single pulse TAP experiments.

Principle: The underlying principle of single pulse TAP experiments is that the zeolite's state is insignificantly altered at the end of each pulse. For the non-conversion processes, the number of molecules exiting the micro-reactor (given by the zeroth moment, M_0) is equal to the number of molecules injected into the reactor. Thus, the probe molecule pulse does not significantly perturb the nano-porous zeolites. As a result, single pulse TAP experiments interpreted by an appropriate theoretical model, are applied to understand and quantify diffusion and adsorption/ desorption of a single species in nano-porous zeolites.

Apparatus used: Temporal Analysis of Product (TAP-2 and TAP-3)

Probe molecules used: Probe molecules used in this study and the reason behind selecting these probe molecules are given in Table A1.

Table A1

Probe Molecules	Reason behind selecting these probe molecules
Argon	Inert
Isobutane	Reactant of alkylation reaction
Butane	Proxy for n-butene
2,2,4-trimethylpentane	Desired product of alkylation reactions
2,5-dimethylhexane	Undesired product of alkylation reactions

Procedure:

1. In this study thin zone configuration is used to pack zeolites in the micro-reactor. In thin zone configuration measured zeolites (5 mg) is placed between two layers of inert nonporous quartz (where, the mass of inert nonporous quartz are kept equal and the total mass is 800 mg). The main advantages of using a thin zone TAP reactor configuration are as follows:

   • Only a small amount of catalysts are required for analysis

   • The catalysts zone can be easily maintained at the isothermal condition

   • Pressure drop across the catalysts zone is small

   • Catalysts are uniformly distributed

2. The feed tank is filled with 50 % by volume of adsorbing probe molecule and 50 % by volume of inert gas (argon), and is maintained at 30 psi.

3. The traces of water in zeolites and/ or any impurities deposited on zeolites surface and/ or in zeolites pores are removed by maintaining the zeolites at 450 C and flowing inert gas (e.g. argon) through the packed micro-reactor, for 1 hr.

4. After the pretreatment of zeolites the micro-reactor is maintained at temperature at which the TAP experiment is desired (temperature range for current TAP reactor is from 25 to 750 C) and inert flow is stopped.

5. The micro-reactor is evacuated to remove the traces of argon and is maintained under high vacuum condition (10^{-8} torr) using vacuum pumps.

6. Small amount of probe molecule is pulsed into the micro-reactor using automated pulsing valve. The response at the outlet is noted setting quadruple mass spectrometer at desired atomic mass unit.

Figure A1 shows the response curves at 359 K of isobutane and argon obtained from thin zone tap reactor, where the beta zeolite (mass = 5 mg and diameter ~ 5 μm) is sandwiched between two inert zones (nonporous quartz, mass = 800 mg and diameter ~ 200 μm) for single pulse experiments. It is observed that the time required for all

157

isobutane molecules to exit the micro-reactor is much higher than for argon molecules.
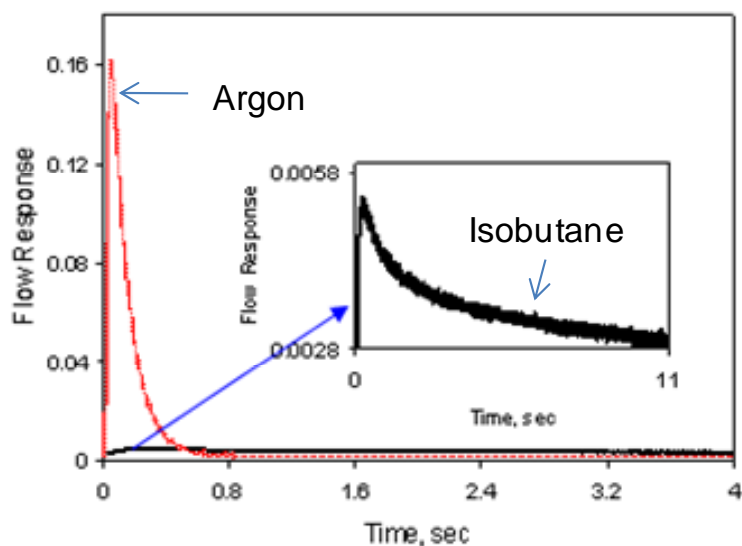
Figure A1: Response curves at 359 K of isobutane and argon obtained from thin zone tap reactor, where the beta zeolite (mass = 5 mg and diameter ~ 5 μm) is sandwiched between two inert zones (nonporous quartz, mass = 800 mg and diameter ~ 200 μm) for single pulse experiments.

Multi Pulse TAP Experiments

Aim: To understand zeolite deactivation by n-butene oligomerization reactions, using multi-pulse TAP experiments.

Principle: In multi pulse TAP experiments the catalysts state is altered in a controlled manner using a series of small pulses or a long pulse in between a series of small pulses. This experimental technique is normally applied for irreversible processes such as adsorption with a low desorption rate or a deactivation reaction. Thus, the catalysts loading or activity can be changed as a function of the number of pulses injected. Consequently multi pulse TAP experiments can be interpreted by an appropriate theoretical model to study the deactivation rate of zeolite catalyst by n-butene

158

oligomerization. Here the experimental procedure for multi-pulse TAP experiments is discussed.

Note: Given the limited availability of TAP experimental set-up these experiments were not completed. However, the procedure is explained to guide future work.

Apparatus used: Temporal Analysis of Product (TAP-2)

Probe molecules used: Probe molecules used in this study and the reason behind selecting these probe molecules are given in Table A2.

Table A2

Probe Molecules	Reason behind selecting these probe molecules
Argon	Inert
n-butene	to study the effect of n-butene oligomerization on zeolite catalyst

Procedure:

1. Steps 1 to 5 are same as mentioned above (see the procedure for single pulse TAP experiments)
2. Small amount of probe molecule is pulsed in short intervals to TAP micro-reactor and response of each pulse as function of time at outlet is noted using mass spectrometer
3. Initially, the number of the molecules observed at the outlet is zero, due to irreversible adsorption of the n-butene. Gradually the number of the molecules at the outlet starts increasing as the number of pulse increases, till it reaches a constant value, due to complete deactivation of zeolite catalyst. Consequently, the multi pulse TAP experiments interpreted by appropriate theoretical model will allow us to quantify the deactivation rate by oligomerization.

Figure A2 a shows the flow responses of n-butene pulsed over thin zone of beta zeolite at 298 K. Figure A2 b shows the calculated zero[th] moment, M_0 of these response curves as a function of number of pulses. It is observed that as the number of pulses increases the M_0 increases and ultimately reaches unity, due to complete deactivation of beta zeolite. Please note that the M_0 equal to unity indicates that the number of molecules exiting the micro-reactor is equal to the number of molecules injected into the reactor.
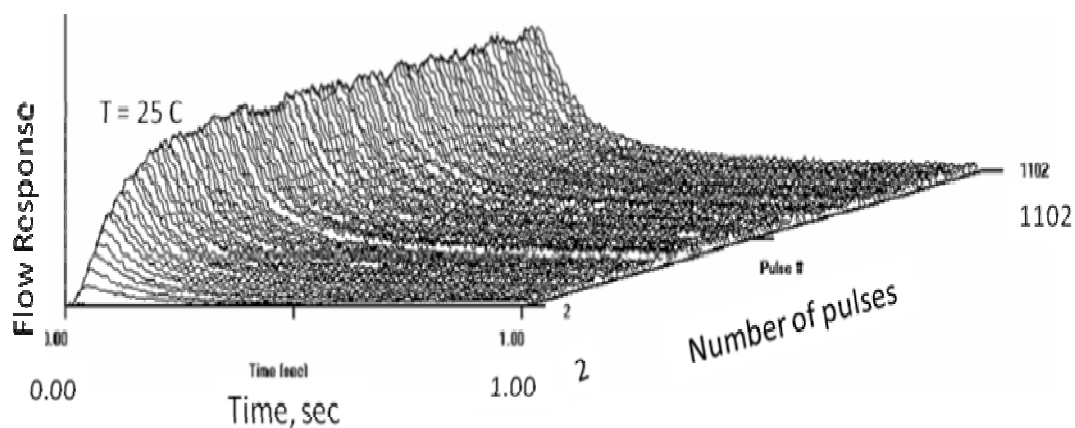
(a)
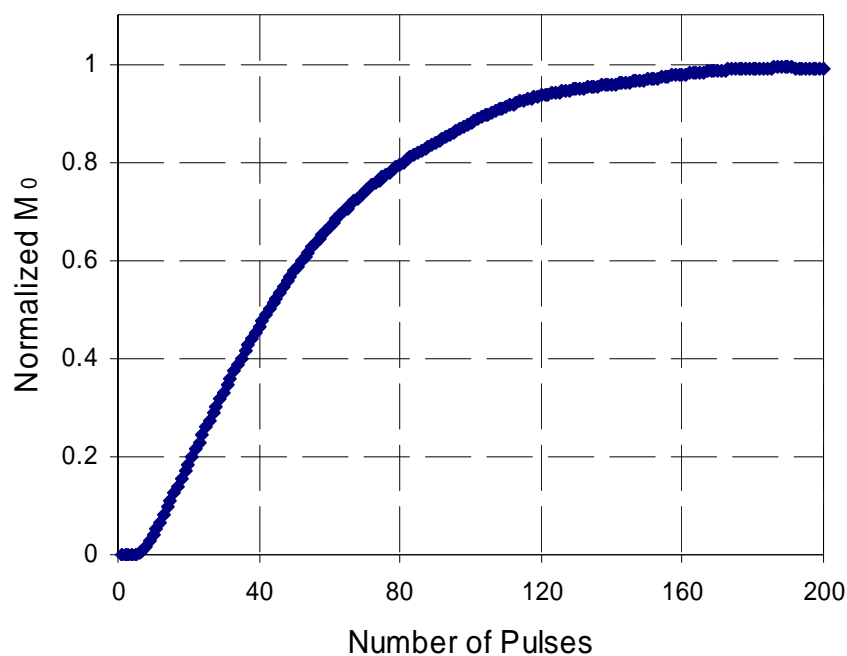
(b)

Figure A2: Multi pulse TAP experiment at 298 K for n-butene over thin zone of beta zeolite; (a) flow responses of n-butene as function of time and number of pulses; (b) calculated M_0 of n-butene response curves as a function of number of pulses.

Simultaneous - Alternating TAP experiments

Aim: To study the influence on transport and kinetic mechanism of one probe molecule in the presence of another probe molecule in nano-porous zeolites.

Principle: During these experiments two alternating pulses at user defined time intervals or two single pulses simultaneous are injected in the micro-reactor. As a result, influence on transport and kinetics of one probe molecule in presence of another can be studied.

Note: Given the limited availability of TAP experimental set-up these experiments were not performed. Here the procedure is explained to guide future work.

161

: Temporal Analysis of Product (TAP-2)

Probe molecules used: Probe molecules used in this study and the reason behind selecting these probe molecules are given in Table A3.

Table A3

Probe Molecules	Reason behind selecting these probe molecules
Argon	Inert
Isobutane	Reactant of alkylation reaction
n-butene	Reactant of alkylation reaction
2,2,4-trimethylpentane	Desired product of alkylation reactions
2,5-dimethylhexane	Undesired product of alkylation reactions

Procedure:

1. Steps 1 to 5 are same as mentioned above (see the procedure for single pulse TAP experiments).

2. Two different sets of experiments are discussed as follows:

    a) Displacement effect: In this set of experiments, one probe molecule is pre-adsorbed (e.g. 2,2,4-trimethylpentane) on nano-porous zeolite packed (at room temperature or lower) in TAP micro-reactor, and then small amount of another probe molecule (e.g. isobutane) is pulsed into the TAP micro-reactor. As a result, the displacement of pre-adsorbed molecules during the adsorption of the second probe molecule can be studied. This study will help in understanding how the desorption process of a particular species in nano-porous zeolites is influenced by the adsorption of another species, which will help in setting up optimal regeneration protocol.

    b) Kinetic effect: In this set of experiments one of the reactant of alkylation reaction (e.g. isobutane) is pre-adsorb on nano-porous zeolites and then series of small amount of another reactant (e.g. n-butene) is pulsed into the TAP micro-reactor. Consequently, the products formed at the end of each

162

pulse and the number of pulses required for the zeolite to completely deactivate at the given operating conditions can be monitored. This study will help future development of the kinetic steps discussed earlier.

Macroscopic chromatographic technique

Aim: To study transport and equilibrium using breakthrough and elution curves.

Principle: The macroscopic chromatographic technique can be used for obtaining transport and equilibrium parameters. The technique is based on the measurement of the response of a packed column filled with zeolite particles to a perturbation in the tracer concentration at the inlet. The conventional methods use either a pulse or step injection of the tracer, after which the desired diffusion constants can be extracted by using moments analysis, which relates the time lag and broadening of the response curve to diffusive and adsorptive properties (Mills and Dudukovic, 1981, Dudukovic and Ramachandran, 1985), or by fitting an approximate analytical solution to the measured response of the column (Haynes and Sarma, 1973). More recently, with the advent of fast computers, more numerical methods are also used to analyze the results (Petchev et al., 2002 and Ahmet et al., 2004).

Note: The packed bed reactor system was installed and tested in CREL laboratory to perform breakthrough experiments in commercially available beta and USY zeolite. However, given the small size of these zeolite particles single pulse TAP experiments were preferred than breakthrough experiments to get reliable estimate of transport and sorption of molecules. Here the procedure is given for future reference.

Apparatus used: Figure A3 illustrates the packed bed reactor system P & ID. The reactor (volume = 50 ml), fabricated from titanium alloy to withstand corrosion and is placed in an aluminum jacket for isothermal temperature control. The pressure in the reactor and the process lines are controlled using back pressure regulator. The maximum operating pressure and temperature of the system are 80 bar and 623 K, respectively. The out flow

of the reactor is heat traced through back pressure regulator into the gas chromatograph to ensure that homogenous mixture of gas is analyzed.
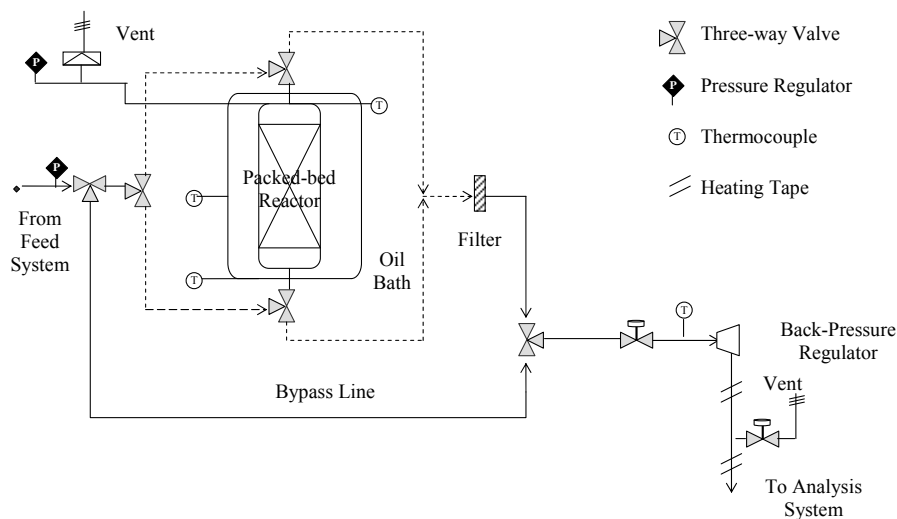
Figure A3: Packed bed reactor system, P & ID

Probe molecules used: Probe molecules used in this study and the reason behind selecting these probe molecules are given in Table A4.

Table A4

Probe Molecules	Reason behind selecting these probe molecules
Nitrogen	Inert
Helium	Carrier Gas
Isobutane	Reactant of alkylation reaction
n-butene	Reactant of alkylation reaction
2,2,4-trimethylpentane	Desired product of alkylation reactions
2,5-dimethylhexane	Undesired product of alkylation reactions

<u>Procedure:</u> The adsorption and desorption experiments can be carried out at atmospheric and elevated pressures in vapor and liquid phases. In the adsorption experiments a step input of species is introduced to a packed column. The packed column consists of three zones, where zeolite catalyst of interest is sandwiched between two inert zones. Desorption experiments is performed by purging the column which is in equilibrium with adsorbed component, with inert gas. In both the experiments the effluent concentration is measured continuously with online gas chromatograph. The inlet concentration of the adsorbing species can be varied by mixing the pure component with a known amount of inert.

<u>Protocol to use packed bed reactor system in Urbauer 210:</u>

Pre-experiment Procedure:
1) Preheat the catalyst to 550 C for 3.5 hours and then keep it aside to cool to room temperature with lid on it
2) Fill the packed bed reactor with preheated catalyst and glass wool support at both ends
3) Assemble the packed bed reactor in heating jacket
4) Start the GC
5) Start the heating fluid flow in jacket to get desired temperature in the packed bed reactor

Experiment Procedure:
1) Once the desired temperature is reached in the bed start the carrier gas (Helium) flow
2) Give a step input of inert gas (Nitrogen) in carrier gas flow
3) Start collecting the GC response on channel 2 (TCD)
4) Give step down input of inert gas (Nitrogen) after 45 minutes
5) Wait till there is no trace of Nitrogen left, that is channel 2 (TCD) response is 0

6) Give a step input of tracer gas (e.g. isobutane) in carrier gas flow so the volume fraction of tracer is 0.5

7) Start collecting the GC response on channel 1 (FID)

8) Wait till a equilibrium is reached

9) Give a step down after 45 minutes

10) Collect data points in note pad for further processing

11) Turn off GC, carrier gas flow and flowing fluid in the jacket

12) Dissemble the packed bed rector out of the jacket and collect the spent catalyst in crucible

13) Clean the place

Caution: The heating fluid may cause minor burn if not handled carefully.

Protocol to use Gas Chromatograph in Urbauer 210

1. Figure A4 shows SRI 8610C GC lay outs

Front view

166

Red protective
oven cover

Main power
switch

Thermostatically-
controlled chassis
cooling fan

Three conductor
grounded
AC power
cord

Computer
serial port
interface
(DB-9)

ECD
make-up gas

Carrier gas
#2 inlet

Carrier gas
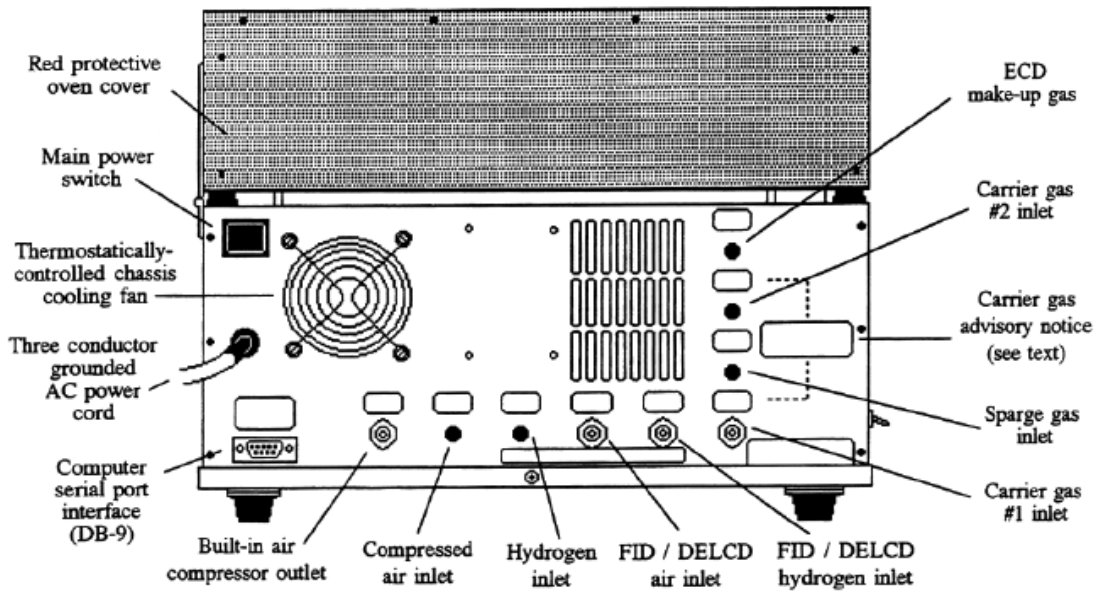advisory notice
(see text)

Sparge gas
inlet

Carrier gas
#1 inlet

Built-in air
compressor outlet

Compressed
air inlet

Hydrogen
inlet

FID / DELCD
air inlet

FID / DELCD
hydrogen inlet

Back View

Stainless steel grill separates heating element
and air circulation fan from analytical column
while permitting unrestricted circulation of
heated air in column oven

Grey column oven
cooling fan with
fast-cool booster fan

Forced cool air inlet into
column oven located at
right rear of oven

High-output
electrical
heating element

Analytical
column

Column oven
air circulation
fan

Ceramic
insulators
secure heating
element in
place

Thermostatically
controlled
detector heater
block ensures
stable detector
inlet / assembly
temperature

End of analytical
column visible
protruding from
detector inlet
(shown with
detector
assembly
removed)

Direct on-column injection port accepts both packed
columns and capillary columns (a wide-bore capillary
column adapter is provided)

Insulated oven wall seals with oven lid
and permits high-temperature operation
with minimal heat loss / radiation

Top view

167

Figure A4: SRI 8610C GC lay out

2. Connect outlet tubing for the reactor system at inlet of injector valve

3. Connect outlet tubing of injector valve to empty cylinder if you want to preserve the effluent for further analysis or send it to exhaust

4. Start PEAK SIMPLE software on the computer attached to GC

5. Click Edit on top of left hand side

6. Check all boxes on Channel 1 if you are using FID and check all boxes on Channel 2 if you are using TCD

7. Click on Temperature of Channel 1

8. Click Add this allows you to enter initial temperature at start of the run the time you need to hold, then the ramp speed and final temperature. This will be displayed in temperature window. **Note:** Time entered here will decided your overall time for each run

For example: Your starting temperature is 100 C for first 2 minutes then you want to reach 180 C at speed of 10 C/minute. So the total time of the run will be 10 minutes beginning at 100 C and ending at 180 C

9. Click ok

10. Click on Events of Channel 1

11. Click Add this allows you to enter new events for your GC application

12. Check Event type: **Zero** and click ok. This makes sure that there is no event taking place at beginning of each run

13. Click Add again

14. Check Event type: **G Valve #1 Load/in,** Check event type: **On** and set event time as per your requirement and click ok. This will make valve move in inject position so that sample is injected in the GC column

INJECT POSITION - TURN SHAFT CW
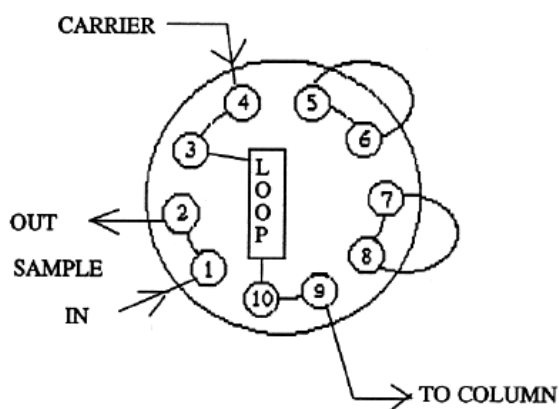
15. Check Event type: **G Valve #1 Load/in, Uncheck** event type: **On** and set event time as per your requirement (which should be latter then time set in step 9} and click ok. This will make valve move in load position so that sample is not injected in the GC column

**LOAD POSITION - TURN SHAFT CCW**
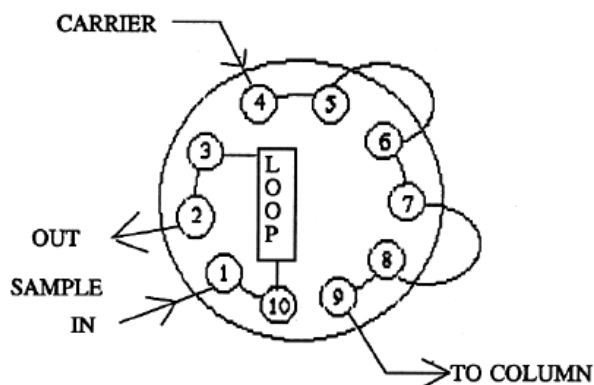
16. Now you will be able to see three events in window. For example you want to have no events at beginning of the run then 0:2 minutes in run you want the sample valve to be open so that the sample is feed in the GC column, then after 0:5 minutes you want the sample valve to close. The events in your window should then look like;

169

17. Click on postrun of Channel 1

18. Here you can enter time needed between each run. It's always good to have some time difference between two runs

Figure A5 a and b shows the step up and step down response at 323 K for isobutane and nitrogen in beta zeolite (2 gm of beta zeolite was packed in the packed bed reactor). It is observed that both breakthrough and elution curves for isobutane is longer than nitrogen indicating that the isobutane is adsorbed and transported in beta zeolite.
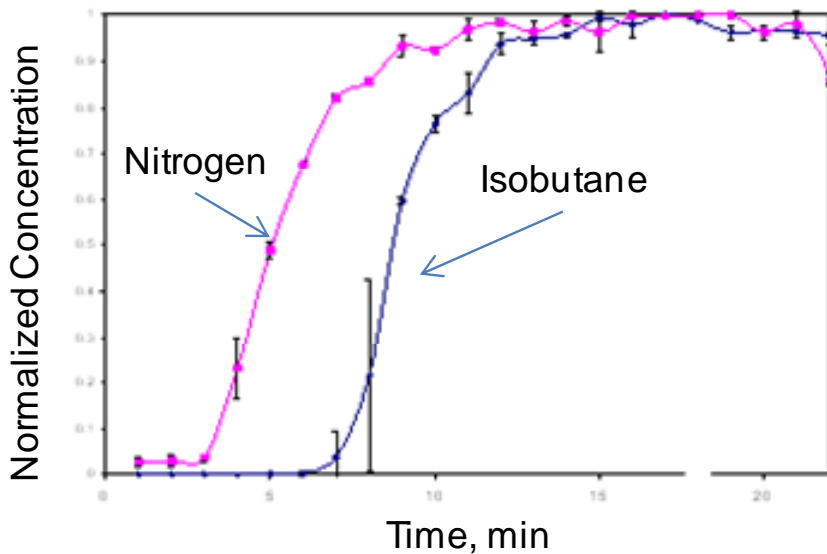
(a)
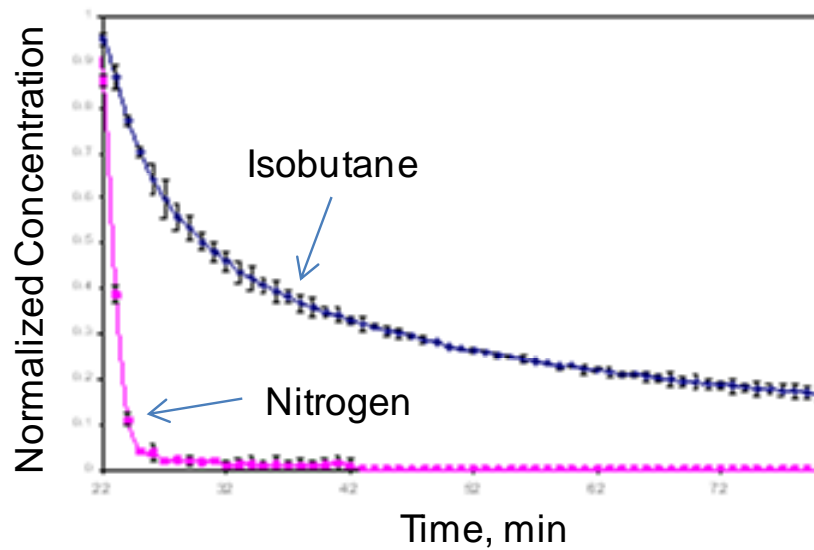
(b)

Figure A5: Adsorption-desorption study in beta zeolite at 323 K; (a) breakthrough curve for isobutane and nitrogen; (b) elution curve for isobutane and nitrogen.

B1. Reactor and feed optimization for solid acid alkylation

Introduction:

Ramaswamy et al., 2005 theoretically investigated different reactor flow configuration for solid acid alkylation. The major inferences of their study is that the packed bed reactor with multiple olefin injection in axial direction (Figure B1.1) will give better performance and will be economical for solid acid alkylation.

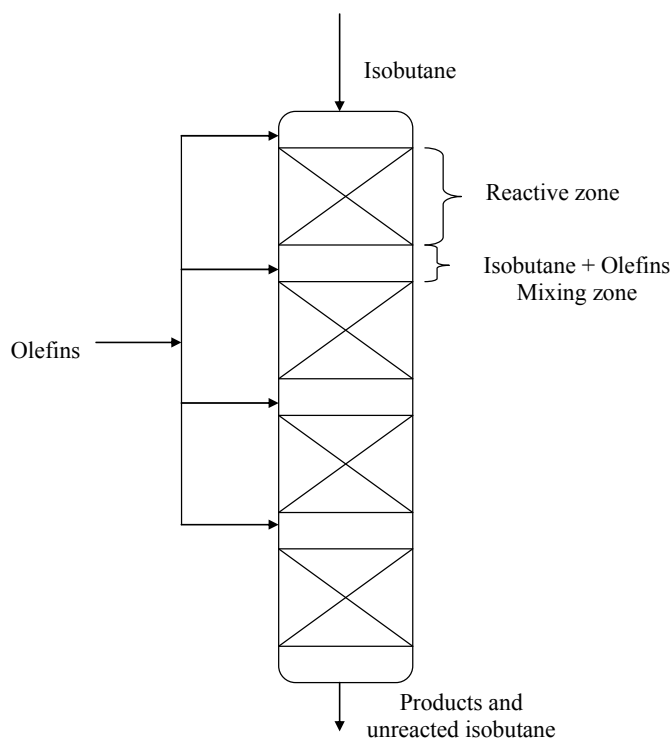Figure B1.1: Packed bed reactor with olefin injected in axial direction

Ramaswamy et al., 2005 used ideal N-CSTR model (to model the packed bed reactor) coupled with particle model in their theoretical investigation. Where complete mixing of the reactants and products were assumed in each CSTR. In reality though, one needs to consider the effect of non-ideal flow patterns, especially when olefins are distributed

along the axial direction. The important effects like axial and radial dispersions of the components should be incorporated in the model equations. These hydrodynamic effects will play an important role in performance of the reactor for solid acid alkylation, as they control the dynamics of paraffin to olefin ratio near the vicinity of catalyst.

Present Contribution:

In this study a three-dimensional adiabatic model for packed bed reactor used in solid acid alkylation processes was developed. The model takes in to account the hydrodynamics and heterogeneous kinetics of solid acid alkylation. The detailed particle model was not considered in current study but its effect on reaction rate was included using effectiveness factor (fudging parameter). Commercial CFD code FLUENT (of Fluent Inc., USA) was used and appropriate user defined subroutines were developed.

The volume averaged momentum, mass and energy balance equations for the continuous phase were:

$$\frac{\partial(\alpha_c \rho_c)}{\partial t} + \nabla \cdot (\alpha_c \rho_c U_c) = S_c \tag{B1.1}$$

$$\frac{\partial(\alpha_c \rho_c U_c)}{\partial t} + \nabla \cdot (\alpha_c \rho_c U_c U_c) = -\alpha_c \nabla p - \nabla \cdot (\alpha_c \tau_c) + \alpha_c \rho_c g + S_{Cm} \tag{B1.2}$$

$$\frac{\partial(\alpha_c \rho_c h_c)}{\partial t} + \nabla \cdot (\alpha_c \rho_c U_c h_c) = -\nabla \cdot (\alpha_c q_c) + S_{Ch} \tag{B1.3}$$

where, S_c, S_{Cm} and, S_{Ch} are the mass, momentum and enthalpy sources representing the exchange between the porous media, (solid acid catalyst) and continuous phase, (gas phase) as well as any sources due to volumetric reaction occurring in the porous phase.

It is instructive to point out that in current case continuous phase was considered to be gas rather than compressed liquid. Further, ideal gas law was assumed to calculate molar density of the system and molecular viscosity was assumed to same as that of air. User

defined subroutine were developed where one can change density and molecular viscosity, which can be implemented in future.

In addition to these, individual species conservation equation was written as:

$$\frac{\partial(\alpha_c \rho_c m_i)}{\partial t} + \nabla \cdot (\alpha_c \rho_c U_c m_i) = S_{Ci} \tag{B1.4}$$

where, S_{Ci} is the mass source for the species i and m_i is the mass fraction of species i in the continuous phase.

Porous media were modeled by the addition of a momentum source term to the standard fluid flow equations. The source term is composed of two parts: a viscous loss term (Darcy, the first term on the right-hand side of equation B1.5), and an inertial loss term (the second term on the right-hand side of equation B1.5).

$$S_i = -\left(\sum_{j=1}^{3} D_{ij} \mu u_j + \sum C_{ij} \frac{1}{2} \rho u_{mag} u_j\right) \tag{B1.5}$$

The constants D_{ij} and C_{ij} for the equation B1.5 were calculated using Ergun's equation for pressure drop.

To make model less intensive, here only two alkylation reactions were assumed as shown in reactions R1 and R2. In the reaction R1 isobutane reacts with n-butene to form isooctanes (TMP) (desired product) and in reaction R2 two n-butene molecules reacts to form octenes (undesired product). Further, it was assumed that the zeolite catalyst does not deactivate with TOS. In future more complicated heterogeneous reaction kinetics and deactivation steps can be included in the current model by implementing few changes in developed user defined subroutine (UDF).

$$C_4H_{10} + C_4H_8 + S \xrightarrow{k_1} C_8H_{18} + S \text{ , and} \tag{R1}$$

$$C_4H_8 + C_4H_8 + S \xrightarrow{k_2} C_8H_{16} + S \text{ .} \tag{R2}$$

Further, the rate of reaction is given as:

$$-r_1 = k_1 C_{isobu\tan e} C_{butene} \xi \varphi \in_S \tag{B1.6}$$

$$-r_2 = k_2 C_{butene}^2 \xi \varphi \in_S \tag{B1.7}$$

where, $C_{isobu\tan e}$, $\& C_{butene}$ were the concentrations of isobutane and n-butene in each cell respectively, ξ was the effectiveness factor, φ was the catalysts activity in current case it was assumed to be 1 with TOS, and $\in_S$ was the solid hold up.

Results and Discussion:

One dimension steady state packed bed reactor simulations were carried out. Figure B2 shows the geometry used in these simulations.
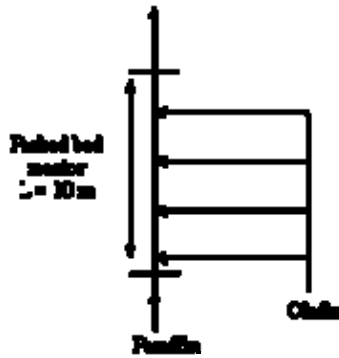

Figure B1.2: 1-d grid simulated for 10 m long packed bed reactor

The initial condition for one dimensional packed bed reactor simulation were

Parameters	Values
Isobutane mass flow rate	4.41 e-03 kg/sec
Butene mass flow rate	4.41 e-04 kg/sec
Residence time	1 hr
Reactor length	10 m
Temperature	353 K

k_1	1.3 m^6/kmole^2-sec
k_2	175 m^6/kmole^2-sec
ξ	0.012 (diffusion limitation)
φ	1
$\in_S$	0.53

Different cases were simulated to understand and implement the effect of different parameters, they were:

1. n-Butene injected at inlet with paraffin
2. n-Butene injected using 3 feed distribution along the length of the reactor
3. n-Butene injected using 5 feed distribution along the length of the reactor
4. n-Butene injected using 10 feed distribution along the length of the reactor

Note: In all the four cases total mass flow rate of olefin into the reactor was kept constant.

Figure B1.3 shows the n-butene mass fraction as the function of reactor length. It is observe that as the number of the n-butene feed distribution increases mass fraction of n-butene at the reactor outlet also increases. The increase in number of distribution for n-butene causes decrease in overall residence time of n-butene inside the reactor, hence decrease in butene conversion.

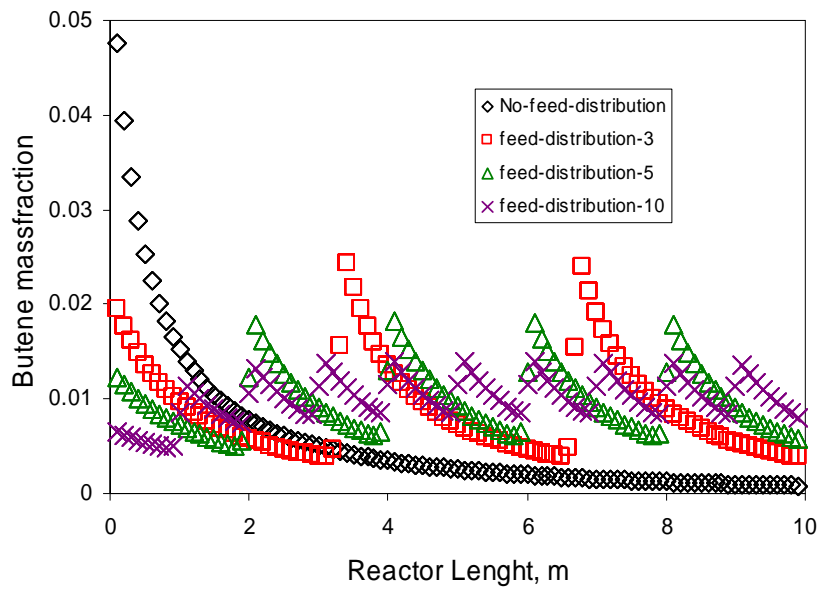Figure B1.3: Butene mass fraction vs. reactor length for different feed distribution

Figure B1.4 shows the isooctanes mass fraction as the function of reactor length. One can infer from Figure B1.4 that as number of n-butene feed injection increases the mass fraction of isooctanes increases, but the increase was incremental after n-butene was distributed 3 times along the length of the reactor.

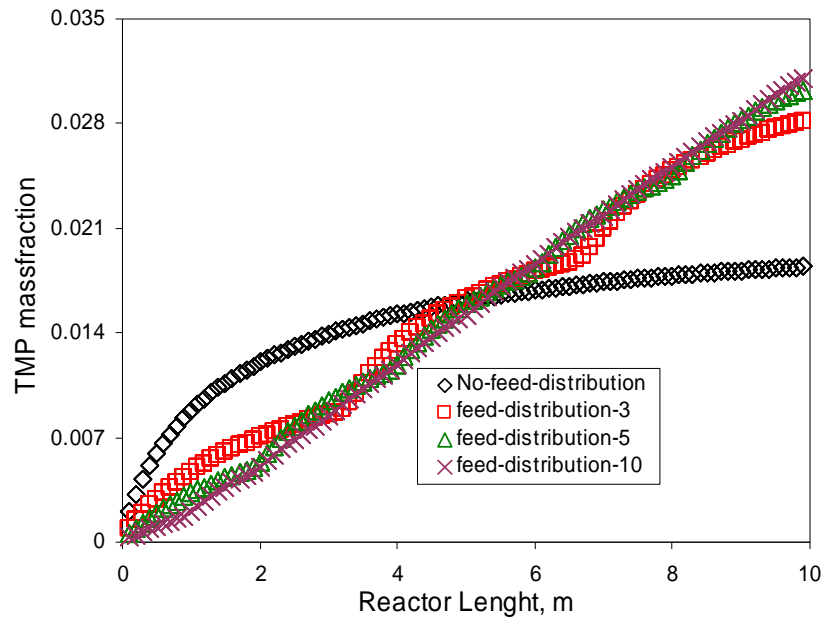Figure B1.4: Isooctanes mass fraction vs. reactor length for different feed distribution

Figure B1.5 shows the octenes mass fraction as the function of reactor length. Total mass fraction of the octenes at reactor outlet almost remains constant for all feed distribution, but it varies severely along the reactor length.
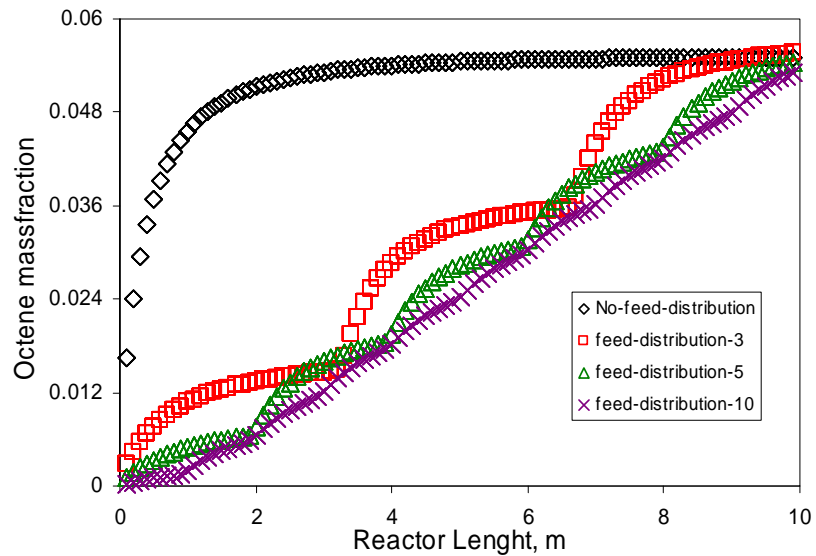

Figure B1.5: Isooctenes mass fraction vs. reactor length for different feed distribution
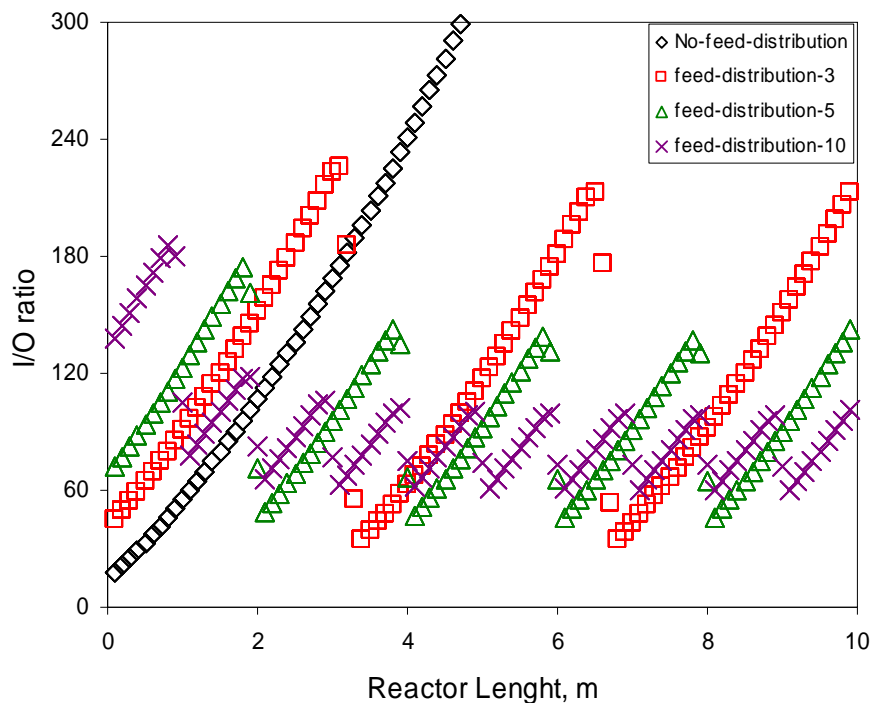
Figure B1.6: Isobutane/n-butene ratio vs. reactor length for different feed distribution

Figure B1.6 shows the isobutane to n-butene (P/O) ratio as the function of reactor length. The P/O ratio changes along the reactor length as the function of n-butene consumed and n-butene added to the reactor. It is interesting to note the range of change in P/O ratio becomes small as number of feed distribution increases.

Summary:

Frame work for 3-d adiabatic model for packed bed reactor for isobutane and n-butene alkylation is reported. The model is incorporated in commercially available solver FLUENT.

Following table summarizes the finding of one dimension steady state simulations with no zeolite catalyst deactivation. The definitions of conversion, yield and selectivity were:

$Conversion = M_{butene\ out} - M_{butene\ in} / M_{butene\ in}$

$Yield = M_{isooc\tan es\ out} - M_{isooc\tan es\ in} / M_{butene\ in}$

179

$$Selectivity = M_{isooc\tan es\,out} / M_{isooctenes\,out}$$

where M is the mass flow rate kg/sec.

Feed Distribution	Conversion %	Yield %	Selectivity %	Average P/O ratio
None	99	24	33	386
3	95	36	51	121
5	93	39	56	98
10	90	40	59	91

Nomenclature

C_j concentration of component j, kmole/m^3

k_i reaction kinetic constant for ith reaction, $m_r^6 / Kmole^6$ -s

U velocity, m/s

S source term

r reaction rate, kmole/ m^3-sec

M mass flow rate, kg/ sec

Greek letters

ρ density, Kg/m^3

μ viscosity, Kg/m-s

$\in_S$ solid holdup

φ activity factor

ξ effectiveness factor

α volume fraction

Reference:

Ramaswamy. R C, P.A. Ramachandran, M.P. Dudukovic (2005). "Modeling of Solid Acid Catalyzed Alkylation Reactors", International Journal of Chemical Reactor Engineering, Vol.3, Article A42

Introduction:

TEOM (tapered element oscillating microbalance) instrument preciously measures any mass change of the catalyst bed due to different mechanism occurring at the catalyst surface or in the catalysts pores. As a result, TEOM can be effectively used to study transport and sorption in nano-porous zeolites. Figure B2.1 shows the schematic of TEOM experimental set up (Gong, 2008). Step input of adsorbing tracer is given at t = 0 and mass change of catalyst bed due to adsorption as a function of time in noted. After saturation level of the catalyst is reached flow of adsorbing tracer is switched off and the catalyst bed is purged with inert gas. Figure B2.2 shows the adsorption and desorption profiles of isobutane on beta-zeolites for different partial pressures (Gong, 2008).
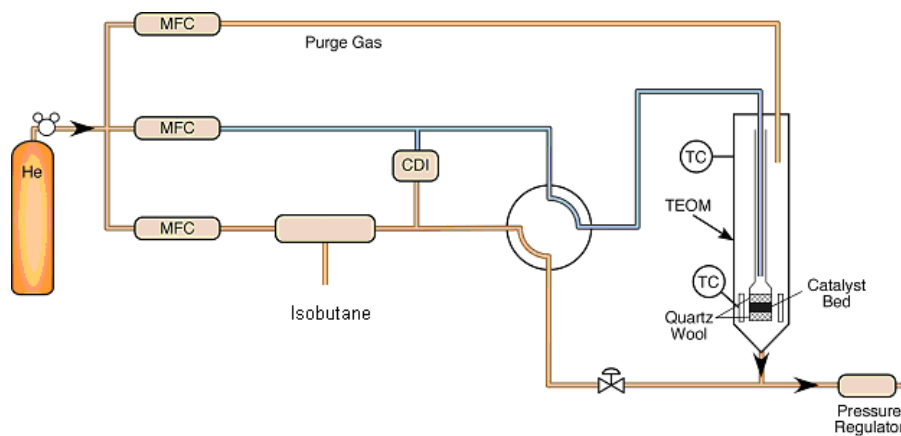

Figure B2.1: Schematic of TEOM experimental set up (Courtesy of Gong, 2008)
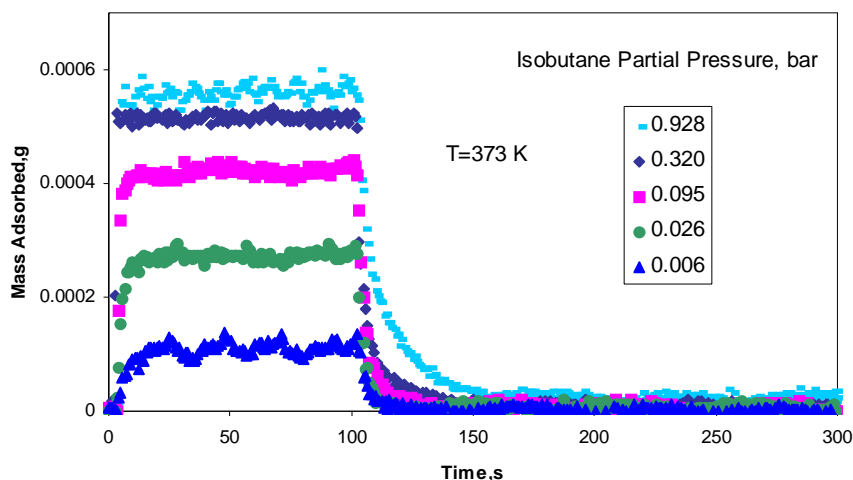
Figure B2.2: TEOM isobutane profiles for step input and
subsequent desorption by He purging (Courtesy of Gong, 2008)

Present Contribution:

This study was conducted with the collaborative efforts with Prof. B. Subramaniam group
at U. of Kansas. To quantify TEOM results appropriate theoretical models are required.
Consequently, a theoretical model was developed to represent the experimental response
and numerically solved. The assumptions used to develop these models were:

1) Spherical particle geometry was assumed

2) Concentration gradient across the very thin catalyst bed was neglected

3) External mass transfer limitation was neglected

4) Isothermal behavior was assumed

5) Non-linear Langmuir adsorption isotherm well explains the data provided

6) Instantaneous equilibrium between gas phase and adsorbed species was assumed
   in the nano-pores

7) Negligible accumulation in the gas phase inside the micro-pore was assumed

8) Adsorbate transport was described by Fick's diffusion equation

9) At the pore mouth conventional assumption of equilibrium between the vapor
   phase and adsorbed phase was not assumed; instead it is considered that at the

182

pore mouth elementary adsorption kinetics take place between the local adsorbate and the vapor phase

Component mass balance is given as:

$$\frac{\partial q}{\partial t} = \frac{1}{r^2}\frac{\partial}{\partial r}\left(D_e r^2 \frac{\partial q}{\partial r}\right)$$

(B2.1)

Boundary condition is given as:

$$-D_e \frac{\partial q}{\partial r}\bigg|_{r=R} = \frac{R k_{des}}{3}\left(q - K_{eq}C(q_{max} - q)\right)\bigg|_{r=R},$$

(B2.2)

$$\frac{\partial q}{\partial r}\bigg|_{r=0} = 0,$$

(B2.3)

The two limiting resistances in the current model are diffusion in nano-pores and desorption at particle surface. Further, two cases were considered for current model. Case # 1: diffusion is free of surface coverage and case # 2: diffusion is dependent on surface coverage. Darken's equation (Karger, and Ruthven, 1992) was used to establish the dependency between surface coverage and effective diffusivity.

So in case # 1:

$$D_e = D_0$$

and in case # 2:

$$D_e = \frac{D_0}{1-\theta}$$

where,

$$D_e = \text{effective diffusivity}, \frac{m^2}{sec}$$

$$D_0 = \text{corrected diffusivity}, \frac{m^2}{sec}$$

$$\theta = \text{surface coverage} = \frac{q(r)}{q_{max}}$$

Please note that the use of Darken's equation leads to increase in effective diffusivity with increase in surface coverage. The developed model is numerically solved using method of line approach.

Results and Discussion:

The simulation requires the knowledge of maximum saturation capacity and equilibrium constant. These data were determined by fitting the equilibrium isotherms obtained from TEOM and Langmuir isotherm.

Figure B2.3 shows the experimental isotherms and the fitted Langmuir isotherm.

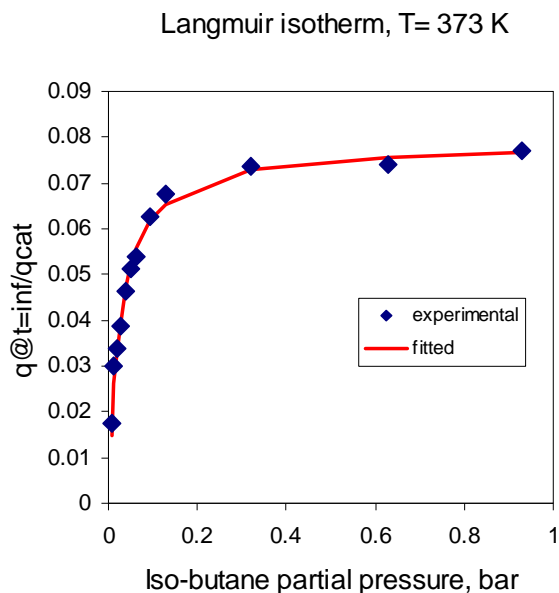$$q\big|_{t=\infty} = \frac{q_{\max} K_{eq} P}{1 + K_{eq} P}$$

Figure B2.3: Langmuir isotherm

Figure B2.4 shows the comparison between model predictions for case # 1 and TEOM experimental results for isobutane on beta-zeolite at low surface coverage ($\theta = 0.40$) at T = 373 K. Experimental results fit well with model predictions and diffusion values estimated compares well with ones reported in literature.

184
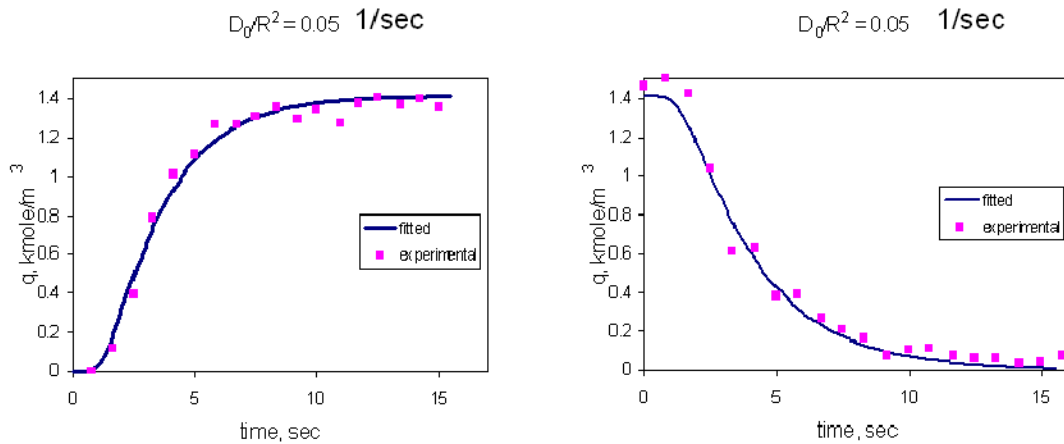
Figure B2.4: Comparison between model predictions for case # 1 and TEOM experimental results for isobutane on beta-zeolite ($\theta = 0.40$) at T = 373 K.

Summary:

TEOM approach can be used to obtain temporal adsorption/ desorption profiles in the zeolites. Depending on the experimental uptake profiles one needs to judiciously choose the presented models to quantify TEOM results. The understanding gained with TEOM results should help in quantifying the frequency for periodic regeneration and the key features needed for the optimal catalysts design and regeneration techniques for solid acid alkylation processes.

Nomenclature:

q	adsorbate concentration, mole/ m^3
q_{max}	adsorbate concentration, mole/ m^3
C	vapor phase concentration, mole/ m^3
r	radial position in the zeolite particle, m
t	time, sec
K_{eq}	equilibrium constant, m^3/ mole
k_{des}	desorption constant, sec^{-1}
P	pressure, bar

Reference:
Gong, K. (2008). Adsorption/desorption studies on solid acid alkylation catalysts using a tapered element oscillating microbalance (TEOM), University of Kansas. Ph.D

B.3 Method of Moments

Introduction:

There are several methods for analyzing the TAP response curve, and to quantify the pertinent parameters. They can broadly be classified as non-linear regression on the data to fit it with numerical solution of developed model in the time domain and method of moments. The previous one is explained in detail in main text, here method of moments approach is presented. In the method on moments, the experimental moments of the response curve are matched with the moments of the model and the pertinent parameters are estimated. It is instructive to point out that the in TAP response experiments the estimated parameters are model dependent.

Present Contribution:

We begin our discussion of the moment-based analysis of TAP data by considering only Knudsen diffusion in the inter-particle voids. Here the dimensionless continuity equation is given as:

$$\frac{\partial c_i}{\partial \tau} = \frac{\partial^2 c_i}{\partial \xi^2} \,. \tag{B3.1}$$

The dimensionless initial condition for equation (B3.1) is (Zou et al., 1993; Gleaves et al., 1997)

$$c_i(0, \xi) = 0 \,. \tag{B3.2a}$$

Further, the dimensionless inlet and outlet boundary conditions are (Zou et al., 1993; Gleaves et al., 1997)

$$\left. \frac{\partial c_i(\tau, \xi)}{\partial \xi} \right|_{\xi=0} = -\delta^*(\tau) \,, \text{ and} \tag{B3.2b}$$

$$c_i(\tau, 1) = 0 \,. \tag{B3.2c}$$

In the TAP experiments the measured variable is exit flux and the dimensionless exit flux is defined as:

$$F_i^* = \frac{\partial c_i(\tau, \xi)}{\partial \xi}\bigg|_{\xi=1}. \qquad (B3.3)$$

The jth moment of the dimensionless exit flux is defined as:

$$M_j = \int_0^\infty F_i^*(\tau) \times \tau^j \, d\tau. \qquad (B3.4)$$

The moment expressions for the developed model can be determined from the Laplace-domain solution for the exit flux using

$$M_j = (-1)^j \,\underset{s \longrightarrow 0}{\lim}\, \frac{\partial^j F_i^*(s)}{\partial s^j}. \qquad (B3.5)$$

Consequently, by solving the equations B3.1, and B3.2 a, b, c, and d in Laplace-domain the zeroth, and first moments obtained are 1 and 0.5, respectively.

For the TAP reactor packed with zeolite particles the dimensionless continuity equations is

$$\frac{\partial c_i}{\partial \tau} = \frac{\partial^2 c_i}{\partial \xi^2} - (1 - \varepsilon_b) k_{d_i}^* \left[K_{eq_i} c_i - \overline{\theta}_i \right]_{\eta=1}. \qquad (B3.6)$$

The initial and boundary conditions for equation B3.6 are same as one reported earlier (B3.2 a, b, and c.) The dimensionless mass balance for zeolite particle is

$$\frac{\partial \overline{\theta}_i}{\partial \tau} = \tau_{p_i} \left[\frac{\partial^2 \overline{\theta}_i}{\partial \eta^2} + \frac{2}{\eta} \frac{\partial \overline{\theta}_i}{\partial \eta} \right]. \qquad (B3.7)$$

The dimensionless boundary conditions for equation (B3.7) at the zeolite particle exterior surface and center are given as

$$\frac{\partial \overline{\theta}_i}{\partial \eta}\bigg|_{\eta=1} = \frac{k_{d_i}^*}{3\tau_{p_i}} \left[K_{eq_i} c_i - \overline{\theta}_i \right]\bigg|_{\eta=1} \qquad (B3.8\ a)$$

and

$$\lim(\eta \frac{\partial \overline{\theta}_i}{\partial \eta})\bigg|_{\eta=0} = 0. \qquad (B3.8\ b)$$

Solving this coupled PDEs (equations B3.6 and B3.7) in Laplace-domain and estimating moments from the dimensionless exit flux is a formidable task which can be avoided by using linear driving force (LDF) model formulated by Glueckauf (1957). This model is widely used to simulate and design fixed-bed adsorption. In this work LDF approach was used to model adsorption – desorption and intra-particle diffusion for zeolite packed in TAP micro-reactor. In following section the derivation of LDF model for TAP is presented.

Linear Driving Model for TAP

The volume average pulse-normalized coverage is given as:

$$\overline{\theta}_{iAverage} = 3\int_0^1 \eta^2 \overline{\theta}_i \, d\eta \tag{B3.9}$$

Assuming parabolic profile of $\overline{\theta}_i$ in the particle

$$\overline{\theta}_i = a + b\eta^2 . \tag{B3.10}$$

Where, a and b are constant depending on time and location in the micro-reactor, but are independent of η. As the indication of degree of approximation the residual R is defined as:

$$R = \frac{\partial \overline{\theta}_i}{\partial \tau} - \tau_p \left[\frac{\partial^2 \overline{\theta}_i}{\partial \eta^2} + \frac{2}{\eta}\frac{\partial \overline{\theta}_i}{\partial \eta} \right]$$

or

$$R = \frac{\partial(a + b\eta^2)}{\partial \tau} - \tau_p 6b . \tag{B3.11}$$

Combining eq. B3.8 a and B3.10 we get:

$$2b = \frac{k_{d_i}^*}{3\tau_{p_i}} \left[K_{eq}c_i - a - b \right] \tag{B3.12}$$

After some mathematical manipulation eq. B3.12 can be rewritten as:

$$a = K_{eq}c_i - \left[1 + \frac{6\tau_{p_i}}{k_{d_i}^*} \right] b . \tag{B3.13}$$

Combining eq. B3.9 and B3.10 we get:

$$\theta_{iAverage} = a + \frac{3}{5}b \qquad \text{(B3.14)}$$

Combining eq. B3.13 and B3.14

$$\theta_{iAverage} - \frac{3}{5}b = K_{eq}c_i - \left[1 + \frac{6\tau_{p_i}}{k_{d_i}^*}\right]b \qquad \text{(B3.15)}$$

After some mathematical manipulation eq. B3.15 can be rewritten as;

$$b = \frac{K_{eq}c_i - \theta_{iAverage}}{\left[\dfrac{2}{5} + \dfrac{6\tau_{p_i}}{k_{d_i}^*}\right]} \qquad \text{(B3.16)}$$

Solution by least square method

The overall fitness of the assumed parabolic profile quantity F can be defined as:

$$F = \int_0^1 R^2\eta^2\partial\eta = \int_0^1 \left[\frac{\partial(a+b\eta^2)}{\partial\tau} - \tau_p 6b\right]^2 \eta^2\partial\eta \,. \qquad \text{(B3.17)}$$

The condition for F to be minimum is:

$$\frac{\partial F}{\partial b} = 0 \,. \qquad \text{(B3.18)}$$

Yielding,

$$\int_0^1 \left[\frac{\partial(a+b\eta^2)}{\partial\tau} - \tau_p 6b\right]\eta^2\partial\eta = 0 \,,$$

or

$$\frac{\partial(a+\frac{3}{5}b)}{\partial\tau} - \tau_p 6b = 0 \,. \qquad \text{(B3.19)}$$

Therefore the average pulse normalized surface coverage in the intra-particle space is:

$$\frac{\partial\overline{\theta}_{iAverage}}{\partial\tau} = \tau_p 6b = \tau_p 6 \frac{(K_{eq}c_i - \overline{\theta}_{iAverage})}{\left[\dfrac{2}{5} + \dfrac{6\tau_{p_i}}{k_{d_i}^*}\right]} \,. \qquad \text{(B3.20)}$$

Solution by Orthogonal Collocation

189

The collocation solution of eq. B3.7 with the boundary condition B3.8 a and b using one collocation point $\eta = \eta_1$ requires that the:

$$R\big|_{\eta=\eta_1} = \frac{\partial(a+b\eta^2)}{\partial\tau}\bigg|_{\eta=\eta_1} - \tau_p 6b = 0 \qquad (B3.21)$$

Taking $\eta_1 = \left(\frac{3}{5}\right)^{0.5}$ we get:

$$\frac{\partial(a+\frac{3}{5}b)}{\partial\tau} - \tau_p 6b = 0 \qquad (B3.22)$$

This is identical to eq. B3.19 obtained earlier by applying least square method. The average surface coverage rate with $\overline{\theta_i}\big|_{\eta=1} - \overline{\theta}_{iAverage}$ as the driving force can be found by subtracting eq. B3.10 at $\eta = 1$ by eq. B3.14

$$\overline{\theta_i}\big|_{\eta=1} - \overline{\theta}_{iAverage} = \frac{2}{5}b \qquad (B3.23)$$

Combining eq. B3.16 and eq. B.23, we get:

$$\overline{\theta_i}\big|_{\eta=1} - \overline{\theta}_{iAverage} = \frac{2}{5}\frac{K_{eq}c_i - \theta_{iAverage}}{\left[\frac{2}{5} + \frac{6\tau_{p_i}}{k_{d_i}^*}\right]}. \qquad (B3.24)$$

Combining eq. B3.20 and B.3.24, we get:

$$\frac{\partial\theta_{iAverage}}{\partial\tau} = 15\tau_p\left(\overline{\theta_i}\big|_{\eta=1} - \overline{\theta}_{iAverage}\right). \qquad (B3.25)$$

This is the LDF expression in dimensionless form for TAP. The dimensionless mass balance for the TAP micro-reactor considering adsorption-desorption and intra-particle diffusion can be rewritten as:

$$\frac{\partial c_i}{\partial\tau} = \frac{\partial^2 c_i}{\partial\xi^2} - \frac{\partial\overline{\theta}_{iAverage}}{\partial\tau},$$

or

$$\frac{\partial c_i}{\partial \tau} = \frac{\partial^2 c_i}{\partial \xi^2} - \tau_p 6 \frac{(K_{eq}c_i - \overline{\theta}_{iAverage})}{\left[\dfrac{2}{5} + \dfrac{6\tau_{p_i}}{k_{d_i}^*} \right]} \tag{B3.26}$$

$$\frac{\partial \theta_{iAverage}}{\partial \tau} = \tau_p 6 \frac{(K_{eq}c_i - \overline{\theta}_{iAverage})}{\left[\dfrac{2}{5} + \dfrac{6\tau_{p_i}}{k_{d_i}^*} \right]} \tag{B3.27}$$

After some mathematical manipulation eq. B3.27 can be rewritten as:

$$\frac{\partial \theta_{iAverage}}{\partial \tau} = \frac{(K_{eq}c_i - \theta_{iAverage})}{\left[\dfrac{\varepsilon_p D_{K_i} R_p^2}{15\varepsilon_b D_e L^2} + \dfrac{\varepsilon_p D_{K_i}}{\varepsilon_b L^2 k_d} \right]} \tag{B3.28}$$

Let,

$$\frac{1}{k_{lump}} = \left[\frac{\varepsilon_p D_{K_i} R_p^2}{15\varepsilon_b D_e L^2} + \frac{\varepsilon_p D_{K_i}}{\varepsilon_b L^2 k_d} \right],$$

or

$$\frac{1}{k_{lump}} = \frac{D_{K_i}}{\varepsilon_b L^2} \left[\frac{\varepsilon_p R_p^2}{15 D_e} + \frac{\varepsilon_p}{k_d} \right]. \tag{B3.29}$$

The first term in RHS bracket represents the resistance due to intra-particle diffusion and second term in RHS bracket represents the resistance due to desorption.

If the intra-particle diffusion time is much smaller than desorption time then $\dfrac{1}{k_{lump}} \propto \dfrac{1}{k_d}$.

If the desorption time is much smaller than intra-particle diffusion time then $\dfrac{1}{k_{lump}} \propto \dfrac{R_p^2}{D_e}$.

If the experiments are repeated with two or more particles with different particle sizes the individual values of the intra-particle diffusion and adsorption-desorption constant may be found. It in this work experiments were conducted on zeolite with mean radius of 5 μm, as a result k_{lump} only was estimated.

Eq. B3.26 and B3.27 can be rewritten as:

$$\frac{\partial c_i}{\partial \tau} = \frac{\partial^2 c_i}{\partial \xi^2} - k_{lump}(K_{eq}c_i - \theta_{iAverage}), \text{ and} \tag{B3.30}$$

$$\frac{\partial \theta_{iAverage}}{\partial \tau} = k_{lump}(K_{eq}c_i - \theta_{iAverage}). \tag{B3.31}$$

The dimensionless initial and boundary conditions for eq. B3.30 and B3.31 are given as:

$$\tau = 0, \quad c_i = 0 \quad and \quad \theta_{iAverage} = 0 \tag{B3.32}$$

$$\xi = 0, \quad \frac{\partial c_i}{\partial \xi} = -\delta(t) \tag{B3.33}$$

$$\xi = 1, \quad c_i = 0 \tag{B3.34}$$

In the developed model the dimensionless parameters K_{eq}, and k_{lump} affects the shape of the TAP response curve. The equations B3.30, B3.31, B3.32, B3.33, and B3.34 were solved by taking the Laplace transfer to get the expression for zero[th], first and second moments. For the one zone TAP reactor configuration these moments are given as:

$$M_0 = 1 \tag{B3.35}$$

$$M_1 = \frac{1}{2}(1 + K_{eq}) \tag{B3.36}$$

$$M_2 = \frac{1}{12 k_{lump}}\left(5K_{eq}^2 k_{lump} + 12K_{eq} + 10K_{eq}k_{lump} + 5k_{lump}\right) \tag{B3.37}$$

For thin zone TAP reactor configuration the expression for zero[th], first and second moments are given as:

$$M_0 = 1 \tag{B3.38}$$

$$M_1 = \frac{1}{2}\left(2l_3 K_{eq} - l_3^3 K_{eq} - 2l_2 K_{eq} + l_2^2 K_{eq} + 1\right) \tag{B3.39}$$

$$M_2 = \frac{1}{12}\left(5l_2^2 + 10l_2 l_3 + 9l_3^2 - 20l_2 - 28l_3 + 24\right)\left(l_2 - l_3\right)^2 K_{eq}^2 +$$

$$\frac{1}{2}\left(\frac{2}{3}l_3^4 - \frac{4}{3}l_3^3 - l_3^2 - \frac{l_2}{3}\left(2l_2^3 - 4_2^2 - 3l_2 + 10\right) + \frac{10}{3}l_3\right)K_{eq} + \qquad \text{(B3.40)}$$

$$\frac{M_1 - 1}{k_{lump}} + \frac{5}{12}$$

Here, l_2 is dimensionless distance from the entrance of TAP micro-reactor to the start of the thin zone and l_3 is dimensionless distance from the entrance of TAP micro-reactor to the end of the thin zone.

Representing the TAP response Curves

An expression for dimensionless TAP response curve in time domain were obtained by using zero[th], first and second moments of the response curve in a leading term of Languerre polynomial series expression (Linek and Dudukovic, 1982) and quasi-lognormal (Q-LND) probability density function (Wang and Lin, 1986).

The approximation to the dimensionless TAP response curve for Languerre polynomial series expression (Linek and Dudukovic, 1982) can be written as:

$$F_i^*(\tau) = \left(\frac{b}{a}\right)^b \frac{\tau^{b-1}e^{-bt/a}}{\Gamma(b)}\left(1 + \sum_{n=3}^{\infty} k_n L_n^{\,b}\left(\frac{b}{a}\tau\right)\right) \qquad \text{(B3.41)}$$

Here a and b are defined as:

$$a = \frac{M_1}{M_0}, \text{ and} \qquad \text{(B3.42)}$$

$$b = \frac{(M_1/M_0)^2}{(M_2/M_0) - (M_1/M_0)^2}. \qquad \text{(B3.43)}$$

Further, the Languerre polynomial $L_n^{\,b}(\tau)$ is defined as:

$$L_n^{\,b}(\tau) = \sum_{i=0}^{n}(-1)^i \frac{n!\Gamma(n+b)\tau^{n-i}}{i!(n-i)!\Gamma(n+b-i)}, \text{ and} \qquad \text{(B3.44)}$$

The series coefficients k_n are evaluated in terms of the moments of TAP response curve and are given as:

$$k_n = \sum_{i=0}^{n} \frac{(-1)^i \Gamma(b)(b/a)^{n-i}}{i! \Gamma(n+b-i)(n-i)!} \qquad (B3.45)$$

Using the Q-LND the expression for dimensionless TAP response curve is:

$$F_i^*(\tau) = \frac{M_0}{\sqrt{2\pi b}\,\tau} \exp\left(-\frac{(\ln(\tau)-a)^2}{2b}\right) \qquad (B3.46)$$

Here a and b are defined as:

$$a = \ln(M_1) - \frac{1}{2}\ln\left(1 + \frac{M_2 - M_1^2}{M_1^2}\right) \qquad (B3.47)$$

$$b = \left[\ln\left(1 + \frac{M_2 - M_1^2}{M_1^2}\right)\right]^{0.5} \qquad (B3.48)$$

Result and Discussions:

The approximations presented in equation B3.41 and B3.46 were compared with standard diffusion curve (Gleaves et al., 1997). Figure B3.1 shows the comparison. It was observed that the Q-LND gives a good representation of standard diffusion curve than Languerre polynomial series expression.
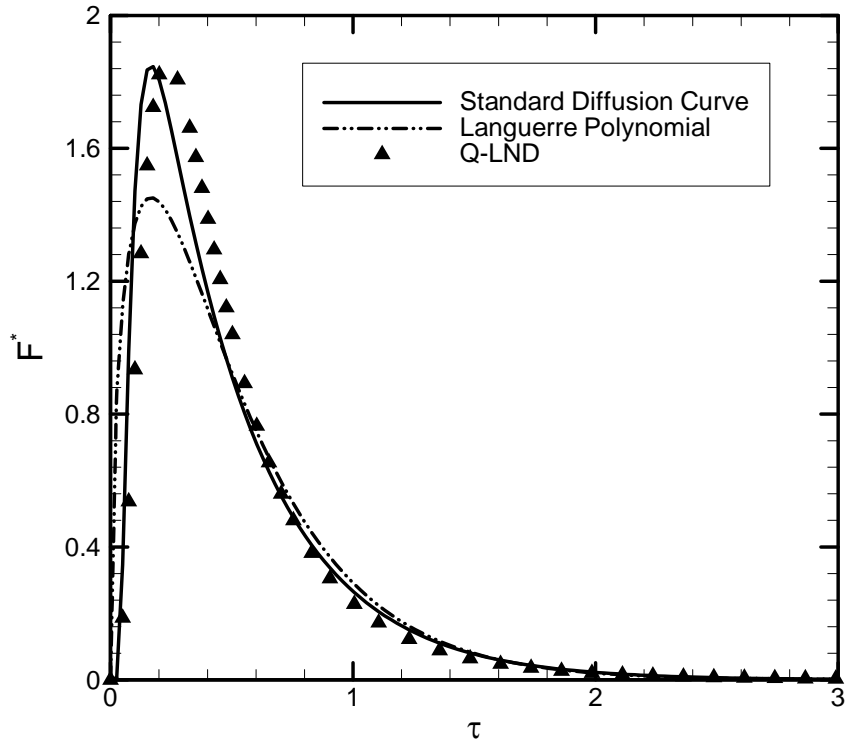
Figure B3.1: Comparison of standard diffusion curve with response curve represent by leading terms of Languerre polynomial series and Q-LND

To evaluate the predictive capability of LDF model for TAP, the response curve of the developed model was compared with the numerical response curve of the full model for one zone TAP reactor configuration (equations B3.6 and B3.7 with appropriate boundary and initial conditions). The time dependent response curve for LDF model was generated using Q-LND approximation. The moments expression represented in equations B3.38, B3.39 and B3.40 were used to calculate the constants a and b of Q-LND approximation. Figure B3.2 shows the comparison of the response curves, where the model parameters constants τ_{p_i}, $k_{d_i}^*$, and K_{eq_i} were kept constant for both the cases (for LDF k_{lump} was calculated from τ_{p_i}, and $k_{d_i}^*$). Not a good match was found. It is concluded that the parabolic profile of surface coverage is seldom achieved as the flux at the zeolite particle

195

boundary is constantly changing under TAP conditions. A better approximation of the surface coverage is needed for using LDF model.
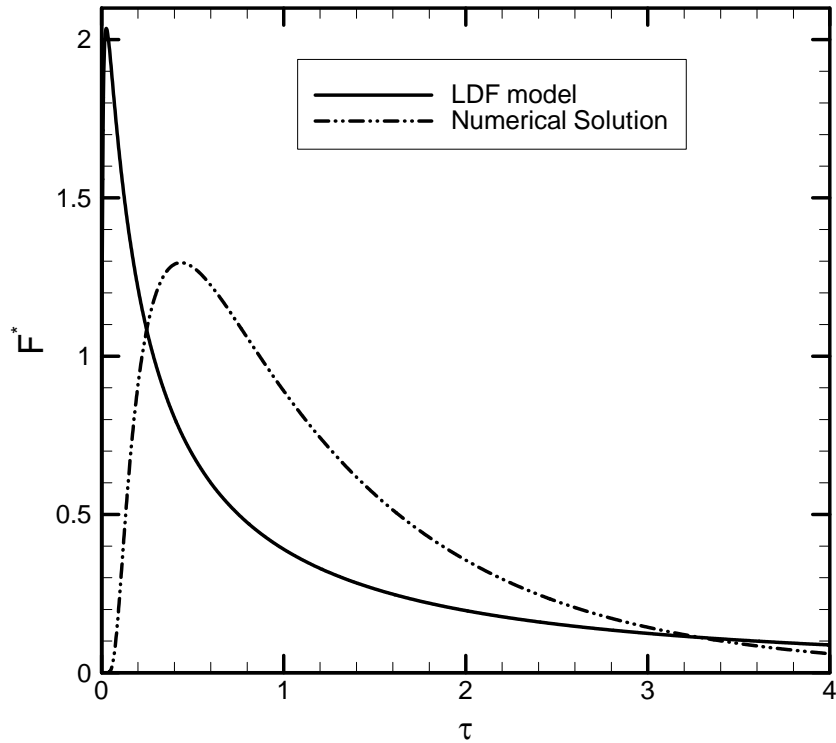
Figure B3.2: The response curves from LDF model and direct numerical simulation of full model (Here, τ_{p_i} is 1 x 10^{-4}, $k_{d_i}^*$ is 1, and K_{eq_i} is 10)

Summary:

Method of moments approach to estimate model parameters is presented. This approach can be effectively used to quickly estimate model parameter from TAP response curve. The TAP response curve can be represented by Q-LND approximation. To use LDF model a better approximation than parabolic profile is needed to represent the surface coverage under TAP experimental conditions.

196

Nomenclature

a constant of approximation

b constant of approximation

c_i pulse-normalized bulk concentration

D diffusivity, m²/ sec

D_{e_i} effective diffusivity in the intra-particle space defined as $D_{e_i} = \dfrac{\varepsilon_p}{\varsigma_p} D_{T_i}$ m²/ sec

D_{K_i} effective Knudsen diffusivity, m²/ sec

D_{T_i} Fickian diffusivity, m²/ sec

$E_i(t)$ time dependent intensity measured by the mass spectrometer, Mv/ sec

$F_i^*(\tau)$ dimensionless exit flow

k_{a_i} adsorption constant, m³/ moles-sec

k_{d_i} desorption constant, 1/ sec

$k_{d_i}^*$ dimensionless desorption constant

K_{eq_i} dimensionless equilibrium adsorption constant

k_{lump} dimensionless lumped parameter defined as $\dfrac{1}{k_{lump}} = \dfrac{D_{K_i}}{\varepsilon_b L^2}\left[\dfrac{\varepsilon_p R_p^2}{15 D_e} + \dfrac{\varepsilon_p}{k_d}\right]$

L micro-reactor length, m

Mw_i molecular weight of species i, kg/ moles

M_j j^{th} moment

q_{max} maximum concentration of adsorption sites, moles/ m³

R universal gas constant, kJ/ moles-K

R_p zeolite particle radius

t observation time, sec

$\bar{t}$ mean of the dimensionless response curve

Greek letters

θ_i dimensionless surface coverage or fraction surface coverage

$\overline{\theta_i}$ pulse-normalized surface coverage

$\overline{\theta}_{iAverage}$ average pulse-normalized surface coverage

$\delta^*(\tau)$ pulse-normalized delta function defined as $\delta^*(\tau) = \dfrac{\varepsilon_b L^2}{D_{K_i}} \delta(t)$

τ dimensionless time

$$\tau_{pi} \quad \frac{L^2 / D_{K_i}}{R_p^2 / D_{e_i}}$$

ξ dimensionless spatial distance within the micro-reactor

η dimensionless spatial distance within the zeolite particle

ε_b solid holdup

ε_p zeolite particle porosity

References:

Gleaves, J. T., G. S. Yablonskii, P. Phanawadee and Y. Schuurman (1997). "Tap-2: An interrogative kinetics approach." Applied Catalysis, A: General 160(1): 55-88.

Linek F. and M. P. Dudukovic (1982)."Representation of Breakthrough curves for fixed-bed adsorbers and reactors using moments of impulse response." Chem. Eng. J. 23: 31-36

Wang, C. T., and C. Lin, (1986). "Prediction of Breakthrough Curves for Fixed Beds," Hua Gong Xue Bao (China), 37, 183.

Zou, B., M. P. Dudukovic and P. L. Mills (1993). "Modeling of evacuated pulse micro-reactors." Chemical Engineering Science 48(13): 2345-2355.

<div align="center">**Subramanya Nayak**</div>

Address: Washington University, Cupples II, Campus Box 1180, St. Louis, MO 63130.

Email: svn1@cec.wustl.edu

Date of Birth: January 28, 1982   **Place of Birth:** Mumbai, India

Education:

Doctor of Philosophy in Energy, Environmental and Chemical Engineering

Washington University in St. Louis

School of Engineering and Applied Science   *GPA: 3.78*

Master of Science in Energy, Environmental and Chemical Engineering

Washington University in St. Louis

School of Engineering and Applied Science   *GPA: 3.78*

Bachelor of Engineering in Petrochemical Engineering

Pune University

Maharashtra Institute of Technology   *Percentage: 75.46 % (Top 5 %)*

Experience:

Washington University in St. Louis – Graduate Research Assistant

August 2004 – Present

Chemical Reaction Engineering Laboratory (CREL) – Assistant

PI: Professor Milorad. P. Dudukovic and Professor Palghat. A. Ramachandran

'Engineering Sustainable Chemicals and Fuels; Zeolite Catalyzed Alkylation Processes'

National Chemical Laboratory, Pune India – Research Assistant

October 2003 – July 2004

National Chemical Laboratory (IFMG) – Assistant

PI: Dr Vivek. V. Ranade

'Modeling and Simulation of Vaporization of Liquid Injected in Gas-Solid Flow'.

Publications:

- **Subramanya V. Nayak**, Saket L. Joshi and Vivek V. Ranade, 2005, "Modeling of vaporization and cracking of liquid oil injected in a gas–solid riser" *Chem. Engr. Sci., Vol – 60, 22, 6049*

- **Subramanya V. Nayak**, P. A. Ramachandran and M. P. Dudukovic, 2008 "Modeling of Reaction Mechanisms for Zeolite Catalyzed Alkylation Processes" *in press Chem. Engr. Sci.*

- **Subramanya V. Nayak**, P. A. Ramachandran and M. P. Dudukovic, 2009 "Transport and Sorption Studies in Beta and USY Zeolites via Temporal Analysis of Products (TAP)*" in press Journal of Catalysis*

- **Subramanya V. Nayak**, P. A. Ramachandran and M. P. Dudukovic, 2009 "Transport in nanoporous zeolites used in alkylation processes" *in preparation*

Honors and Activities:

- Elected **President** of Student Leadership Council (2005-2006), CEBC, USA
- Elected **President** of WASP, (2002-2003), India
- Won **Second prize** in Graduate Research Symposium Poster Competition-2008
- Awarded **Third rank** by Pune University in Final year Petrochemical Examination
- Won **First prize** in State Level Project Competition Prakalp-2003, India
- Won **First prize** in Poster Competition organized by Institute of Engineer's, India
- Won travel award for ISCRE-20, Japan and NASCRE-2, USA
- In charge of safety of the chemical laboratories under CREL research group from August 2005 to present

Alkylation of isobutane and n-butene.   Nayak Ph.D